國立交通大學

材料科學與工程學系

博士論文

設計與製備多功能孔洞二氧化矽基板奈米平台應用於提高療效與增強影像之研究

Design and Characterization of Multifunctional Mesoporous Silica Nanoplatform for Enhanced Therapy and Imaging Modality

研究生：陳柏溶

指導教授：陳三元/劉典謨 教授

中華民國一零二年七月

設計與製備多功能孔洞二氧化矽基板奈米平台應用於提高療效與增強影像之研究

Design and Characterization of Multifunctional Mesoporous Silica Nanoplatform for Enhanced Therapy and Imaging Modality

研究生：陳柏溶　　Student：Po-Jung Chen

指導教授：陳三元/劉典謨　　Advisor：San-Yuan Chen/Dean-Mo Liu

國立交通大學

材料科學與工程學系

博士論文

A Thesis
Submitted to Department of Materials Science and Engineering
College of Engineering
National Chiao Tung University
In partial Fulfillment of the Requirements
For the Degree of
Doctor of Philosophy
in
Materials Science and Engineering
July 2013

Hsinchu, Taiwan, Republic of China

中華民國一零二年七月

設計與製備多功能孔洞二氧化矽基板奈米平台
應用於提高療效與增強影像之研究

研究生：陳柏溶　　　　　　　　　　　　　　　　　　　指導教授：陳三元/劉典謨

國立交通大學材料科學與工程學系

摘要

奈米載體結合診斷與治療等多功能的系統，在全球已經引起各學界與業界人士的注意。在本論文中，利用材料、奈米粒子與藥物的結合，設計與製備具多功能的磁性奈米載體與具高強度光反應的顯影載體。除了具有利用外部磁場或雷射光控制釋放治療之功能外，並可以同步監測奈米載體的位置。然而，目前的多功能奈米載體仍然具有許多缺點需要改善，例如:無法長時間監控載體，容易受外界環境影響載體的穩定性。為了改善這些缺點，本論文發展出一個結合診斷與治療於一身的多功能二氧化矽載體。於本論文第一部分研究，首先，以孔洞二氧化矽當作基材，將抗癌藥物載入孔洞中，並利用單分散氧化鐵奈米粒子藉由化學鍵和孔洞二氧化矽奈米粒子鍵結。此化學鍵提供氧化鐵奈米粒子和孔洞性二氧化矽奈米粒子有緊密的鍵結，並且當作奈米蓋子完整覆蓋於二氧化矽的孔洞表面。在沒有外加磁場刺激之下，近乎沒有藥物從磁性奈米載體裡面外漏出來。然而，當我們施加可控制的外加磁場刺激之下，磁性奈米載體表面的氧化鐵粒子將會脫落，使得二氧化矽孔洞外漏出來，進而讓孔洞裡面的抗癌藥物釋放出來。此磁性奈米載體具有高強度的核磁共振顯影效果與螢光顯影的特性，比較於其他類似的結構更為出色。

另一方面，由於孔洞二氧化矽材料受限於孔洞的大小，孔洞太小無法攜帶大分子藥物與功能性奈米粒子，限制其應用性。因此，於論文第二部分，我們將功能性量子點載入於 10 奈米孔洞大小的二氧化矽球中，並且透過非共價鍵的生物分子架接標靶分子，此

載體具有良好的光對比特性與多重色碼標示的優點，更可以大幅降低量子點會受到外界環境影響的特性，保護量子點維持其量子效應，並且改善量子點的生物相容性差的缺點，最後在標靶分子方面，具有標靶分子的載體在腫瘤細胞的標靶具有很明顯的差異。透過此簡易的乘載方法，使量子點在生物醫學應用上有很大的突破。

同時，在第三部分，設計另一種新型多功能奈米複合結構的奈米載體，其結構是由奈米金棒填滿孔洞二氧化矽球，並且具有高度強度且穩定性的光聲顯影效果。可當作一種新型的光聲顯影之顯影劑，這種光聲顯影是一種結合超音波及雷射所發展出之一種具有低成本及良好顯影的技術，可以應用偵測腫瘤及一些的病態組織，而其中當然最重要的是顯影劑。而奈米金棒成長填滿於孔洞奈米結構，則可以應用在這方面來當顯影劑，此奈米金棒於高強度的奈米秒發間歇性雷射照射之下，仍然具有且保留良好的光學特性與光熱穩定度，而且無論於生物體外和生物體內都具備了穩定的光聲顯影和高效率的熱治療，由此可以得知奈米金棒成長填滿多孔性球具有強而有力的奈米診斷治療能力。此外，奈米金棒填滿多孔性球也具有良好的生物相容性與低毒性的特性。所以，奈米金棒填滿孔洞球，的確可以成為一個具有熱治療與光聲顯影的奈米診斷治療平台。最後，將此奈米金棒填滿孔洞球與磁性氧化鐵結合，形成同時具備有磁特性、光特性奈米載體與核磁共振顯影和光聲顯影雙重顯影的功能。利用磁導引的特性，在光聲顯影方面，提升了將近 7.2 倍的影像強度，另一方面，應用於幹細胞治療上，奈米載體經由幹細胞吞噬之後，透過磁導引的方式，將幹細胞引導至中風部位，大幅降低於人體中幹細胞 90%會被肝跟肺所代謝。未來期望能透過多功能的奈米載體達到新一代的治療與診斷效果。

關鍵字：控制釋放，孔洞二氧化矽，影像顯影，磁標靶

Design and Characterization of Multifunctional Mesoporous Silica Nanoplatform for Enhanced Therapy and Imaging Modality

Student: Po-Jung Chen Advisor: San-Yuan Chen/Dean-Mo Liu

Department of Materials Science and Engineering

National Chiao Tung University

Abstract

Multifunctional nanoprobes have been received greatest attention worldwide, especially combining diagnostic and therapeutic functions. In order to enhance imaging and therapy efficiency, the use of the mesoporous silica nanoparticles as a new type of actuator platforms to anchor guest molecules has been developed in this thesis. In first part, an anticancer drug, (S)-(+)-Camptothecin (CPT)) were encapsulated into the mesoporous silica nanoparticles which is chemically capping by Fe_3O_4 to prevent drug elapsing and remote-controllable. With an external high frequency magnetic field (HFMF) trigger, the Fe_3O_4 nanocaps can be removed from surfaces of mesoporous silica vehicles due to the breaking of chemical bonds and then subsequently lead a fast-responsive drug release and concentration gradient for second drug release. The nanosystems also show the potential of magnetic resonance imaging and fluorescence imaging for diagnostic. In second part, the meosporous silica matrix was enlarged the pore size to incorporate quantum dots for bioimaging. A highly hydrophobic mesoporous silica nanoparticle with pore size greater than 10 nm was incorporating quantum dots and bridging the targeting peptide cRGD by using noncovalent biotin-streptavidin link. Their outstanding optical contrasts render these highly fluorescent QDs ideal fluorophores for wavelength-and-intensity multiplex color coding. This nanoprobe is able to provide highly chemically stability for the quantum dots and maintain the high quantum yield even in the low

pH value environment. For the targeting effect, the cRGD-encoded lipid coated QDs tagged nanobeads exhibited significantly increased $\alpha_v\beta_3$-expressing cell targeting toward MCF-7 breast cancer cells over the $\alpha_v\beta_3$-low expressing in HeLa cervix cancer cells. Furthermore, in MCF-7 xenograft nude mice, the cRGD-encoded nanoprobes revealed prolonged accumulation time at tumor site.

In third part, we a new type of theranostic system based on gold nanorod-containing mesoporous silica nanobeads with exceptionally efficient and stable photoacoustic imaging modality was synthesized. The novel nano-seaurchin structure is characteristic of high-density and well-dispersive gold nanorods (AuRNBs) in one mesoporous silica nanobead. The optical properties and photothermal stability of porous silica nanobeads with pore-filled gold nanorods (AuRNBs) under intense irradiation with nanosecond laser pulses were investigated by UV-Vis spectroscopy and transmission electron microsocopy. The AuRNBs showed increased photothermal stability and retained their superior optical properties under much higher fluence laser pulses at 10 mJ/cm^2. The AuRNBs also provided a stable photoacoustic signal and highly efficient hyperthermia effect both *in vitro* and *in vivo*, indicating a powerful theranostic modality.

Finally, the mesoporous silica nanobeads tagged iron oxides nanoparticles, where the nanoporosity was further filled with gold nanorods. The magnetic nanoprobes could be controlled by external magnetic navigation, capable of performing MR and photoacoustic imaging modalities simultaneously. The magnetic nanoprobes showed that the r_1 value was 1.205 s^{-1}mM^{-1}Fe, and the r_2 value was 127.89 s^{-1}mM^{-1}Fe. The higher transverse (r_2) relaxivities could be attributed to the silica nanobeads tagged the Fe_3O_4 NPs in the pore forming a well-dispersive and chemical stable condition. On the other hand, the PA contrast could be further increased 7.2 times PA signals by an external magnet PA signals compare with without an external magnet applied, demonstrating their ability to perform active magnetic guide. The magnetic nanoprobes could be internalized efficiently toward the stem

cells and a prolonged retention for 48 hours. In addition, the magnetic nanoprobes were successfully achieved using an external magnet guiding the stem cells to the stroke areas and cell labeling by MR images for *in vivo* MCAO stroke mouse. Therefore, this multifunctional nanoprobe not only provides exceptionally highly photothermal stability but also remote-controlled property, which offers potential advantages for carrying/homing stem cell, therapy and dual imaging.

Keywords: remote-controlled, mesoporous silica nanoparticles, imaging modality, magnetic target

致謝

經過碩士班一年和博士班四年的時間努力之下，終於在 2013 年取得博士學位。想當初剛進來交通大學念研究所的時候，對於實驗的掌握度和技巧都是那麼的生澀懵懂，在學習的過程中也是遭遇了許多困境與瓶頸，可喜的是都能克服這些難題，順利取得口試資格與博士學位。

在碩博五年的時間裡，遇到了許多貴人的幫忙與協助。首先感謝我的指導教授陳三元老師和劉典謨老師的提拔與教導，還記得碩一的時候，陳三元老師問我要不要直接逕博，在老師的啟發之下，繼續攻取博士學位。陳三元老師不只在實驗研究方面教導我，更於生活和未來的規劃上關心與照顧著我，在老師身上也學到如何與人相處技巧和方法。劉典謨老師在學術實驗上總是有許多創新與與新穎的看法與見解，在老師的身上學習到世界觀，讓我知道世界是如此之大，並且在老師的教導之下，實驗想法和英文能力都有很大的提升。還有要感謝胡尚秀學長，在碩一的時候帶著懵懂的我進行實驗設計與實驗概念，讓我快速的成長，感謝蕭繼聖學長在電子顯微鏡上的幫助與討論。另外，也要感謝黃信揚、蕭孟軒、周昊勳、李偉銘、蘇嘉偉、王衍人、張博學、陳又維、江智聖、黃薇蓁、楊翊筠等實驗室學長與同學的照顧，帶給我歡樂的實驗室生活，也特別感謝康宜達學弟協助我完成許多實驗。

最後也要感謝我的家人長久以來的支持和鼓勵，讓我可以無後顧之憂專注於我的學業研究，感謝佩鈴的照顧與陪伴，感謝我的電腦陪我渡過漫長的博士生活，沒有耍脾氣的當機。未來將是另一段人生路程，期望自己可以貢獻一己之力，對整個社會有所幫助。

Content

Figure Captions

Chapter 1

Introduction

Nowhere in medicine are the goals of nanotechnology more hotly pursued than in the field of oncology. Researchers have created many examples of nanoparticles that can circulate through the bloodstream and stick to tumors. The optical or magnetic properties of some of these nanoparticles provide a means to image tumors at their earliest stages of development. Recently, nanometer-sized particulate systems are being developed as intravascular carriers to increase the levels of monitored agents delivered to targets, with the fewest side effects [1,2]. It is desirable that multiple nanocomponents with diagnostic and therapeutic functions can be integrated into a "single" nanosystem. These systems follow on the concept of a "theranostic" device, in which both diagnostic and therapeutic functions can be administered in a single dose. For example, anti-cancer medicine inhibit/kill cancer cells, superparamagnetic iron oxide nanoparticles improve the contrast of magnetic resnonance images (MRI) and magnetic remote-controlled, the quantum dots show fluorescence intensity signal can be seen by unaided eyes, and gold nanostructures improve the contrast of photoacoustic imaging (PA) and near-infrared light therapy. Recently, many studies have been reported in multifunctional nanostructures, such as self-assemble nanoparticles(drugs)/polymer [3-5], material surface-coating metal particles [6-8], and chemical covalent bridge drugs[9,10]. However, such a manner of the nanocomponents may change or decrease the property of the functionalized nanoparticles. For example, optical probes such as quantum dots coated by silica, copolymer or lipids demonstrated a great damage of quantum yield approximately 30-50% lower than their original brightness, limiting their applications. Furthermore, most chemical modifications are complex, time-consuming and even in a risk of losing original function of the starting nanomatrix. Therefore, a practical development of desired nanocomponents with coupled functionalities will enable new imaging modes available from each individual component for diagnostic and therapeutic specificity.

More recently, many studies have highlighted an important class of nanocarriers made of a mesoporous silica matrix, such as MCM-41, where therapeutic or biologically active molecules can be filled and anchored into the nanopores of the silica nanoparticles, followed by a subsequent free-diffusion release from the nanopores after administration to the site of disease [11-16]. On the other hand, the MCM-41 type mesoporous silica has several attractive features, such as a stable mesoporous structure, large surface area, tunable pore size and volume, and well-defined surface properties. Therefore, combining different nanostructured materials will enable the development of multifunctional nanomedical platforms for diagnostic and therapeutic. However, using MCM-41 type mesoporous silica matrix with pore size about 2~3 nm to load guest molecules by chemical bridge, it will limit tagged large molecule weight molecules or particles and damage the property through chemical bridge [17, 18]. Thus, the development of multifunctional large pore size nanoprobes, meaning more capacity for guest molecules, enabling new imaging modalities beyond the intrinsic limitations of individual components is essential. Several important issues on mesoporous-based multifunctional carriers for diagnostic and therapeutic still need to be further addressed.

First, in order to combine functionality with magnetic resonance (MR) imaging capability and drug-carrying functions, we synthesized a new drug-release nanosystem in Chapter 4, which is constructed by chemically capping Fe_3O_4 nanoparticles onto the surface of a MCM-41 type mesoporous silica, while drug molecules (here we used a dye molecule (FITC) and an anticancer drug, (S)-(+)-Camptothecin (CPT)) were encapsulated into the pores. An external high frequency magnetic field (HFMF) trigger can be used to remove the Fe_3O_4 nanocaps from surfaces of mesoporous silica vehicles due to the breaking of chemical bonds and then subsequently lead a fast-responsive drug release for cancer therapy.

Next, in Chapter 5, we shifted our focus on large pore size (about 10~15nm) mesoporous nanocarriers which were designed and prepared by a highly hydrophobic octadecyltrimethoxysilane-modified mesoporous silica nanoparticle (hydrophobic porous nanobeads) with pore size greater than 10 nm. Furthermore, with hydrophobic QDs encapsulated into hydrophobic porous nanobeads and the peptide cRGD bridged on the surface of QD-tagged nanobeads by using noncovalent biotin-streptavidin link, a potential cellular-based targeting is achievable and exhibits significantly increased $\alpha_v\beta_3$-expressing cell targeting toward MCF-7 breast cancer cells over the $\alpha_v\beta_3$-low expressing in HeLa cervix cancer cells, indicating a successful design of highly-cytocompatible nanoparticulate platform capable of providing cell-specific targeting and nano-imaging modalities for biomedical applications.

To combine the diagnostic and therapeutic functions, we employed the gold nanorods to form a novel nano-seaurchin structure which is characteristic of high-density and well-dispersive gold nanorods in one mesoporous silica nanobead (AuRNBs) (Chapter 6). The AuRNBs showed increased photothermal stability and retained their superior optical properties under much higher fluence laser pulses at 10 mJ/cm^2. The AuRNBs also provided a stable photoacoustic signal and highly efficient hyperthermia effect both *in vitro* and *in vivo*, indicating a powerful theranostic modality.

To be continued, in Chapter 7, base on the nano-seaurchin structure nanoprobes, the multifunctional nanodevice were fabricated by intergrating homing stem cells, photoacoustic imaging, MRI imaging and magnetic remote-controlled. The nanoprobes (GRMNBs) is composed of mesoporous silica nanobeads tagged iron oxides nanoparticles, where the nanoporosity was further filled with gold nanorods, giving a multifunctional nanoprobe that can be controlled by external magnetic navigation, capable of performing MR and photoacoustic imaging modalities simultaneously. The GRMNBs showed the significant contrast enhancement for PA signal with the presence of external magnet as compared with pure gold nanorods. This multifunctional nanoprobes with magnetically controllable nature and dual contrast modality offer great advantages for carrying/homing stem cell, therapeutic delivery and real-time detection/diagnosis.

We make a conclusion in Chapter 8 for each part of our nanoprobes with diagnostic and therapeutic functions. These nanoprobes are simultaneously being multifunctional, compact in size, and sensitive to environmental. Future development of this new class of multifunctional nanoprobes includes diagnostic and therapeutic in biological and medical fields, and will lead to a new biomedical nanotechnology. Numerous cancer or other disease-related deaths could be averted in the near future, and our lives will be finally shaped by the advances and developments in the field.

Chapter 2

Literature Review and Theory

2.1 Introduction of nanosystems for detection and treatment of diseases

Development of multifunctional nanosystems is one of the most rapidly advancing areas of science in which material and chemical researchers are contributing to human health care. The nanosystems have typically focused on imaging enhancement, compounds delivery and site-specific targeting, which separate the function for each independent part. Currently, the new multifunctional nanosystems have considerable effort to incorporate both diagnostic and therapeutic functions into a “single” nanoscale device. The technique can achieve such dual functions, particularly combining the imaging detection and disease treatment. The key concept of the new nanosystems is “theranostic” device, in which both diagnostic and therapeutic integrated into a single nanosystem. For designing functional nanoparticles, one advantage of combining imaging with therapeutic functions is that can be monitored the biodistribution of nanosystems *in vivo*, reducing the unintended side effect and physical or chemical damage in health tissues [19,20]. By these wide advantages of theranostic system, a number of researches have been successfully proposed to integrate active drug molecules, optical or magnetic nanoparticles and host materials, where to manipulate theranostic desirably. For example, different structural nanocomponents as host materials have been used to introduce the guest materials such as drugs, protein and funcational nanoparticles [21-26]. As shown in **Figure 2.1**, the nanosystems contain both structural (therapeutic) and functional (diagnostic) nanocomponents. For the therapeutic nanocomponents, the structural nanocomponents such as liposome [27, 28], micelle [29, 30], porous silica [31-33], and polymer [34, 35] can be host materials for carrying drugs cargo, while gold and carbon nanostructure enable photothermal therapy. For the diagnostic nanocomponents, the functional nanocomponents such as gold nanostructures (for optical imaging), quantum dots (for fluorescence imaging) and magnetic nanocrystal (for MRI imaging and magnetic guiding) can be guest materials for incorporating into the inner space or equipping on the surface of host materials. This literature reviews exhibit the theranostic nanosystems including mesoporous silica nanoparticles in which the functional materials such as quantum dots, iron oxides, or gold nanostructures incorporating/equipping for imaging, diagnosis, photo-absorbing or triggering drug release. In the later sections of this review, we focus on the current applications of nanotechnology for silica nanoparticles, especially for the tumor treatment and stem cell therapy.

Component	**Nanoparticle type**	**Function**
Structural (therapeutic) nanocomponent	**Liposome, micelle, porous silica, and virus**	**Drug delivery**
	Gold and carbon nanostructure	**Photothermal therapy**
Functional (diagnostic) nanocomponent	**Gold nanostructure and quantum dots**	**Optical imaging**
	Magnetic nanocrystal	**Magnetic guiding**

Figure 2.1 The nanosystems design strategies for containing both therapeutic and diagnostic nanocomponents.

2.2 Remote-controlled mesoporous silica nanoparticles for drug delivery

The unique properties of mesoporous silica materials, such as stable mesoporous structures, high surface areas (>800m^{2}g^{-1}), uniform tunable pore sizes (2-10 nm in diameter) and volumes, easy surface modification and good biocompatibility have made them ideal for hosting molecules of various sizes, shapes, and functionalities. Due to high surface areas property, the mesoporous silica materials have been developed for controlled-release delivery of drug, biocides, genes, or even proteins *in vitro* or *in vivo* [36-38]. A major key point for mesoporous silica materials as drug delivery is most hydrophobic therapeutic anticancer drugs as low solubility in aqueous media hampers the ability of drugs to be administered through the intravenous route. The mesoporous silica materials have large surface areas and porous interiors that can be used as reservoirs for storing hydrophobic drugs. Unlike polymer-based nanoparticles, these robust inorganic materials can tolerate many organic solvents. In addition, remote-controlled drug delivery can improve the efficiency of chemotherapy by allowing the maximum fraction of the delivered drug molecule to react with the disease sites without adverse effects on the normal cells. Therefore, the development of a desired drug carrier for medical applications should possess remote-controlled properties as well as real-time responsiveness to the stimuli, for example, when urgent disease control measures and/or a slow, sustained release to meet different clinical applications are required.

2.2.1 Synthesis of mesoporous silica nanoparticles

The development of porous materials with large specific surface areas is currently an area of extensive research, particularly with regard to potential applications in areas such as adsorption, chromatography, catalysis, sensor technology, and gas storage. An upsurge began in 1992 with the development by the Mobil Oil Company of the class of periodic mesoporous silicas known as the M41S phase. These materials superseded zeolite molecular sieves, which were restricted to a pore size of around 1.5 nm. Like the microporous crystalline zeolites, this class of materials is characterized by very large specific surface areas, ordered pore systems, and well-defined pore radius distributions. Unlike the zeolites, however, the M41S materials have pore diameters from approximately 2 to 10 nm and exhibit amorphous pore walls. The most well-known representatives of this class include the silica solids MCM-41 (with a hexagonal arrangement of the mesopores, space group *p6mm*), MCM-48 (with a cubic arrangement of the mesopores, space group *Ia3d*), and MCM-50 (with a laminar structure, space group *p2*) (**Figure 2.2**). The use of supramolecular aggregates of ionic surfactants (long-chain alkyltrimethylammonium halides) as structure-directing agents (SDAs) was groundbreaking in the synthesis of these materials. These SDAs, in the form of a lyotropic liquid-crystalline phase, lead to the assembly of an ordered mesostructured composite during the condensation of the silica precursors under basic conditions. The mesoporous materials are obtained by subsequent removal of the surfactant by extraction or calcination.

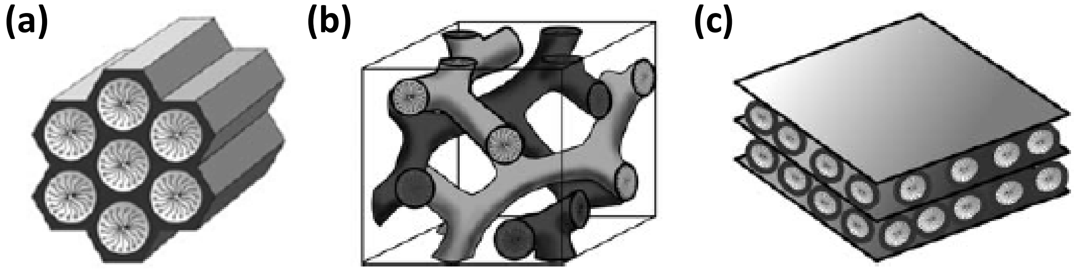

Figure 2.2 Structures of mesoporous M41S materials: (a) MCM-41, (b) MCM-48 and (c) MCM-50 type. [39] Copyright 2006, Wiley-Vch.

In-depth investigations into the formation process of these composite materials have found that two different mechanisms are involved: On the one hand, in true liquid-crystal templating (TLCT), the concentration of the surfactant is so high that under the prevailing conditions (temperature, pH) a lyotropic liquid-crystalline phase is formed without requiring the presence of the precursor inorganic framework materials (normally tetraethyl- (TEOS) or tetramethylorthosilica (TMOS)).[40] On the other hand, it is also possible that this phase forms even at lower concentrations of surfactant molecules, for example, when there is cooperative selfassembly of the SDA and the already added inorganic species, in which case a liquid-crystal phase with hexagonal, cubic, or laminar arrangement can develop (**Figure 2.3**)

One of the major applications of mesoporous silica materials is in biomedicine. Appling the porous materials to drug delivery system, it may be possible to achieve improving delivery of poorly water-soluble drugs and delivery of large macromolecule drugs. However, for general MCM type mesoporous silica materials, the pore size are about 2~4 nm in diameter, which is too small to load large molecules/drugs and amount of molecules/drugs, limiting biomedicine applications. Therefore, many methods have been reported for controlling the periodic unit size and pore size of mesoporous materials. The most commonly used technique is the introduction of a “swelling agent” into the structure directing template.

Commonly used swelling agents include the large organic hydrocarbons such as dodecane, 1,3,5-trimethylbenzene, triisopropylbenzene,and tertiary amines. The introduction of these agents has been shown to lead to pore expansion by up to 30%, but loss of long-range order of the mesoporous structure is commonly observed.

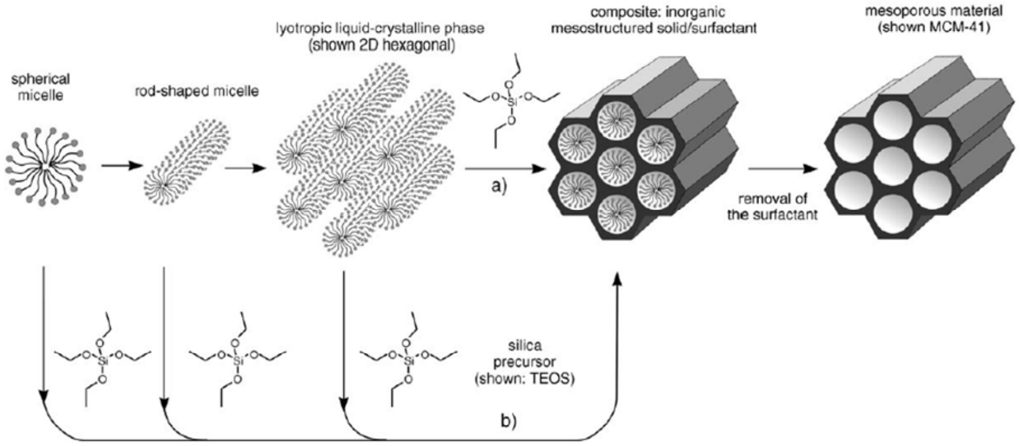

Figure 2.3 Formation of mesoporous materials by structure-directing agents: a) true liquid-crystal template mechanism, b) cooperative liquidcrystal template mechanism. Copyright 2006, Wiley-Vch.

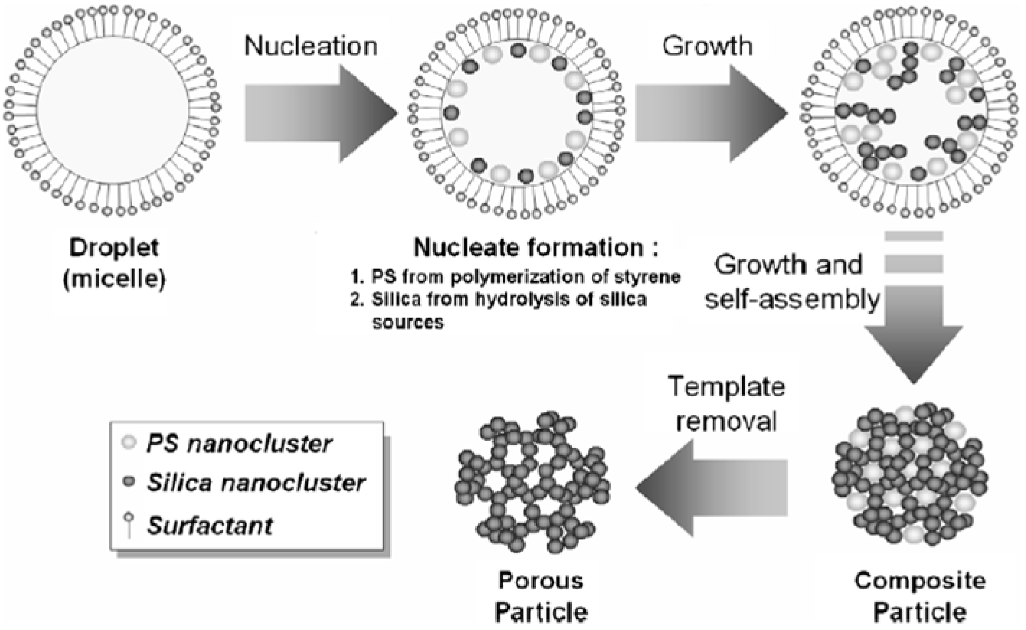

Figure 2.4 Formation of mesoporous materials by using hydrolytic condensation of tetraorthosilicate (TEOS) and polymerization of styrene into polystyrene (PS). Copyright 2008, Elsevier Inc.

Smarsly et al. [41] and Ryan et al. [42] recently reported a method of mixing surfactant blends to tailor the pore size of mesoporous silicas, showing Angstrom-level control over the pore size. However, the longest block copolymer surfactant chain used governs the largest pore size obtainable with this method. In order to solve these problem, Nandiyanto et al. [43] develop a method for the preparation of spherical nano-sized silica particles with a tunable pore size ranging from 4 to 15 nm and a tunable particle size in nanometer range (20–80 nm) using an organic template method in a water/oil phase. (**Figure 2.4**) In briefly, using hydrolytic condensation of tetraorthosilicate (TEOS) and polymerization of styrene into polystyrene (PS) grows silica nanoparticles. The process uses an amino acid as the catalyst, octane as the hydrophobic supporting reaction component, and cetyltrimethylammonium bromide (CTAB) as the surfactant. The reactions took place simultaneously in the micelle, resulting in a composite silica/PS particle with CTAB as the as-prepared product. In the final step, the organic components (CTAB and PS) were removed by calcination to yield the mesoporous silica particles. Thus, the mesoporous silica materials can be potential of biomedicine applications by using this synthesized method.

2.2.2 Nanoparticles cap porous silica nanoparticles for drug delivery

Recent reports [44, 45] on the design of capped and gated mesoporous silica derivatives have shown promise in the generation of controlled-release nanodevices. Mesoporous silica nanoparticles that are capable of stimuli-responsive release of cargo molecules are presently under active investigation. A key challenge for these integrated systems is whether they can be designed for biological use through autonomously controlled nanovalve opening inside cells of interest. Many important site-selective deliveries, e.g., deliveries of highly toxic antitumor drugs, such as Taxol, require “zero release” before reaching the targeted cells or tissues. However, the release of encapsulated compounds of many current drug delivery systems typically takes place immediately upon dispersion of the drug/carrier composites in water. Also, the release mechanism of many biodegradable polymer-based drug delivery systems relies on the hydrolysis-induced erosion of the carrier structure. Such systems typically require the use of organic solvents for drug loading, which could sometimes trigger undesirable modifications of the structure or function or both of the encapsulated molecules, such as protein denaturation and aggregation. Therefore, designing a stimuli-responsive and capable of “zero premature release” for controlled release systems is required.

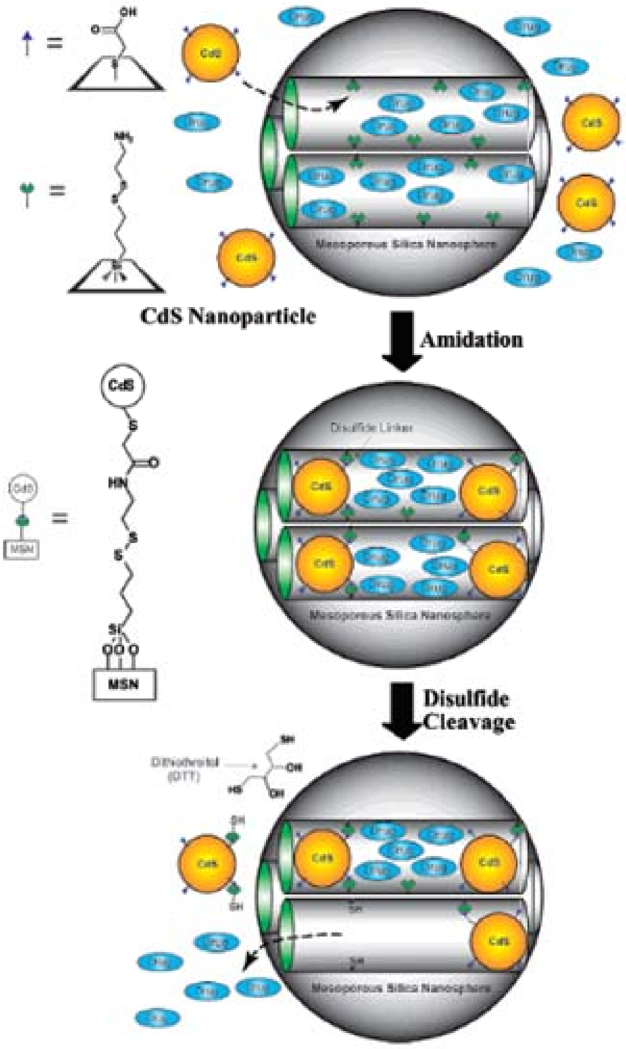

Figure 2.5 Schematic representation of the CdS nanoparticle-capped MSN based drug/neurotransmitter delivery system. The controlled-release mechanism of the system is based on chemical reduction of the disulfide linkage between the CdS caps and the MSN hosts. Copyright 2003, American Chemical Society.

Lai et al. [46] report the synthesis of a novel MCM-41 type mesoporous silica-based controlled-release delivery system that is stimuli-responsive and chemically inert to the matrixentrapped compounds. The major concept of this designed is using CdS nanoparticles to cap on the surface of mesoporous silica nanoparticles for preventing the drug in the pore releasing in nature. Furthermore, the controlled-release mechanism of the system is based on isulfide linkages between the MSNs and the CdS nanoparticles are chemically labile in nature and can be cleaved with various disulfide-reducing agents, such as dithiothreitol (DTT) and mercaptoethanol (ME). As shown in **Figure 2.5**, the release of the CdS nanoparticle caps from the drug/neurotransmitter-loaded MSNs can be regulated by introducing various amounts of release triggers. The functionalized MCM-41 type of mesoporous silica nanosphere material can be used as novel controlled-release delivery carriers that are stimuli responsive.

2.2.3 Responsive molecules with mesoporous silica nanoparticles for drug delivery

The goal of drug delivery is to administer medicinally active molecules with high specificity to diseased cells in a targeted and controlled manner. Recently, mesoporous silica nanoparticles have emerged as an appealing class of drug delivery vehicles for the treatment of diseases on account of their sophisticated design and mode of action. The size and shape of the mesoporous silica nanoparticles can be tuned to maximize cellular uptake, while the dimensions and physical environment of the nanopores inside the nanoparticles can be tailored to store a range of small molecules of different sizes. In particular, the silica nanoparticles can be covered and mechanized with a monolayer of nanovalves3k and other artificial molecular and supramolecular machines in order to convert them into smart drug delivery vehicles, that is, mesoporous silica nanoparticles capable of storing and releasing drug molecules on command in response to external stimuli such as pH and/or redox changes, irradiation with light, or the action of enzymes. As shown in **Figure 2.6**, Park et al. [47] employed the functional mesoporous silica nanoparticles that are composed of the surface cyclodextrin (CD) gatekeepers, functional stalks, and fluorescence probes within porous channels as an enzyme-responsive nanocontainer. The torus shaped CD was initially chosen to block the porous channel of mesoporous silica nanoparticles. The CD moiety of the gatekeeper can be hydrolyzed by α-amylase, and the stalk part was designed to be degraded by lipase to exhibit enzyme-responsive characteristics in the release of guests. This system would provide diverse applications in controlled drugs delivery.

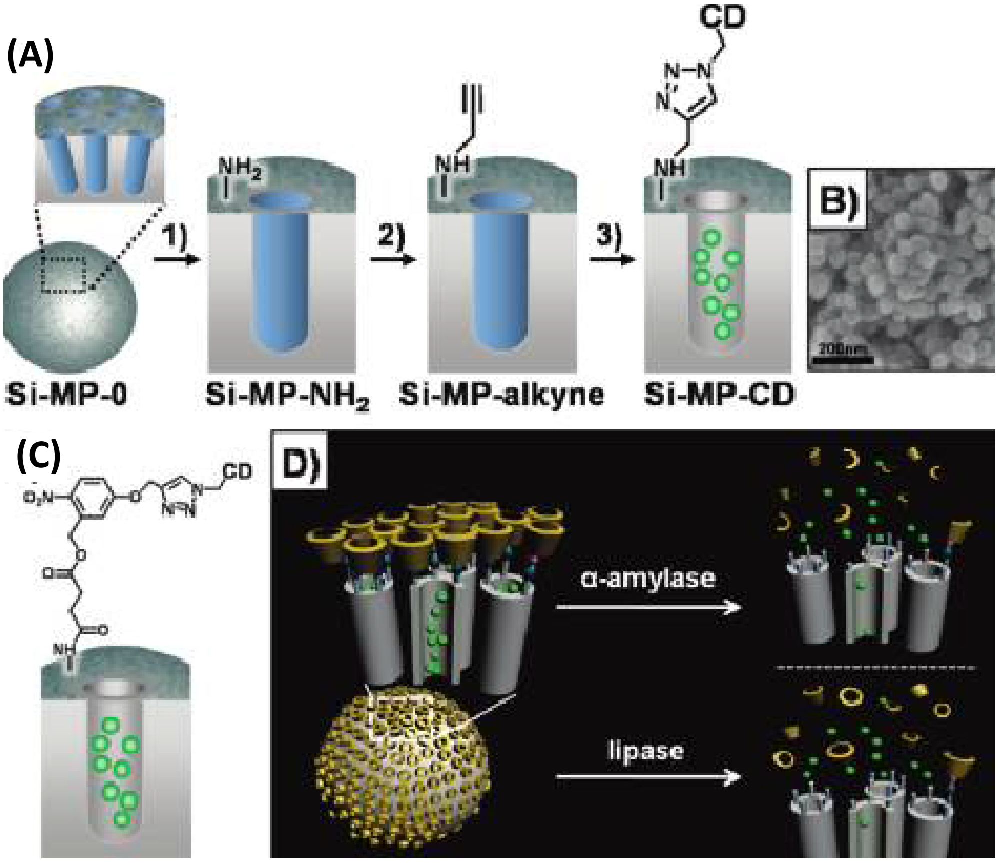

Figure 2.6 (A) Synthetic route to Si-MP-CD: (1) 3-aminopropyltriethoxysilane; (2) succinic anhydride and triethylamine; (3) removal of CTAB, calcein, CuSO4, sodium ascorbate, and mono-6-azido-_-CD. (B) FE-SEM image of Si-MP-CD. (C) The structure of surface functional motifs on Si- MP-NBE-CD. (D) Schematic illustration for enzyme-triggered release of guest molecules from the pore of CD-covered nanocontainers. Copyright 2009, American Chemical Society.

2.3 Gold nanostructure for biomedical applications

The gold nanostructures have been a subject of intensive research for their fascinating surface plasmon resonance (SPR) property which is an optical phenomenon arising from the interaction between an electromagnetic wave and the conduction electrons in a metal. Under the irradiation of light, the conduction electrons in a gold nanostructure are driven by the electric field to collectively oscillate at a resonant frequency relative to the lattice of positive ions. At this resonant frequency, the incident light is absorbed by the nanostructure. Due to this SPR property, gold nanostructures have found use in a rich variety of applications such as (1) Surface-enhanced Raman scattering (SERS). (2) Photoacoustic imaging. (3) Photothermal treatment. The remarkable SPR properties and biocompatibility of gold nanostructures make them promising both as a contrast agent for *in vivo* optical imaging, and as a therapeutic agent for photothermal treatment of cancer for biomedical applications.

2.3.1 Synthesis of gold nanostructure

Gold nanostructures have proven to be a versatile platform for a broad range of biomedical applications, with potential use in numerous areas including: diagnostics and sensing, *in vitro* and *in vivo* imaging, and therapeutic techniques [48-50]. These applications are possible because of the highly favorable properties of gold nanostructures, many of which can be tailored for specific applications. In 1857, Michael Faraday demonstrated the synthesis of gold colloids in an aqueous medium and Gustav Mie solved Maxwell’s equations for spherical particles, making it possible to predict and explain the optical properties of gold nanospheres. Furthermore, in 1951, John Turkevich provided a robust and simple synthesis method [51]. In 1973, Frens systematically developed methods for synthesizing gold nanospheres of varying diameter by citrate-mediated reduction [52]. The resulting nanoparticle sizes are largely governed by the stoichiometric ratio of gold to the reducing agent with larger ratios leading to larger diameters. One of the most interesting and powerful properties of gold nanostructures is localized surface plasmon resonance (LSPR) which is the origin of many of the new applications of nanoscale gold nanostructures. When a gold nanostructure encounters electromagnetic radiation of an appropriate wavelength, the delocalized conduction electrons of the metal will begin to oscillate collectively relative to the lattice of positive nuclei with the frequency of the incoming light (**Figure 2.7a**). This process can be divided into two types of interactions: scattering, in which the incoming light is re-radiated at the same wavelength in all directions, and absorption, in which the energy is transferred into vibrations of the lattice (i.e., phonons), typically observed as heat. Together, these processes are referred to as extinction (extinction = absorption + scattering).

Gold nanospheres (**Figure 2.7b**) are the simplest structure to synthesize, and there are now well-developed techniques to produce particles of high uniformity with a variety of sizes. In a typical reaction, a dissolved gold salt (such as $HAuCl_4$) is reduced to gold atoms in the presence of a capping agent or surfactant to prevent aggregation. In the most commonly used method, the reducing agent and capping agent are the same: citrate ions. Depending on the size of the nanosphere, strong LSPR extinction will occur between 500–600 nm. Nanoshells (**Figure 2.7c**) are created by depositing small gold nanoparticles onto the surface of a silica sphere, followed by deposition of more gold through chemical reduction. The LSPR of gold nanoshells and gold nanocages can also be tuned into the NIR by adjusting the thickness of gold walls surrounding a dielectric or hollow core which depends on the ratio between the diameter of the particle (typically ~120 nm), and the thickness (~10 nm) of the deposited gold layer. For gold nanorods (**Figure 2.7d**), these structures are typically synthesized by a seed-mediated, solution-phase method, where small gold seeds are added to a series of growth solutions. Typically, gold nanorods have two LSPR peaks, one for the transverse mode around 515 nm and the other for the longitudinal mode whose position depends strongly on the aspect ratio of the rod. By adjusting the synthesis parameters (e.g., the concentrations of key reagents and the size of the initial gold seeds), it is possible to synthesize nanorods with strong LSPR-based absorption across the visible spectrum and into the NIR. For the gold nanocage (**Figure 2.7e**), the gold nanocages are created by hollowing out the interior of a

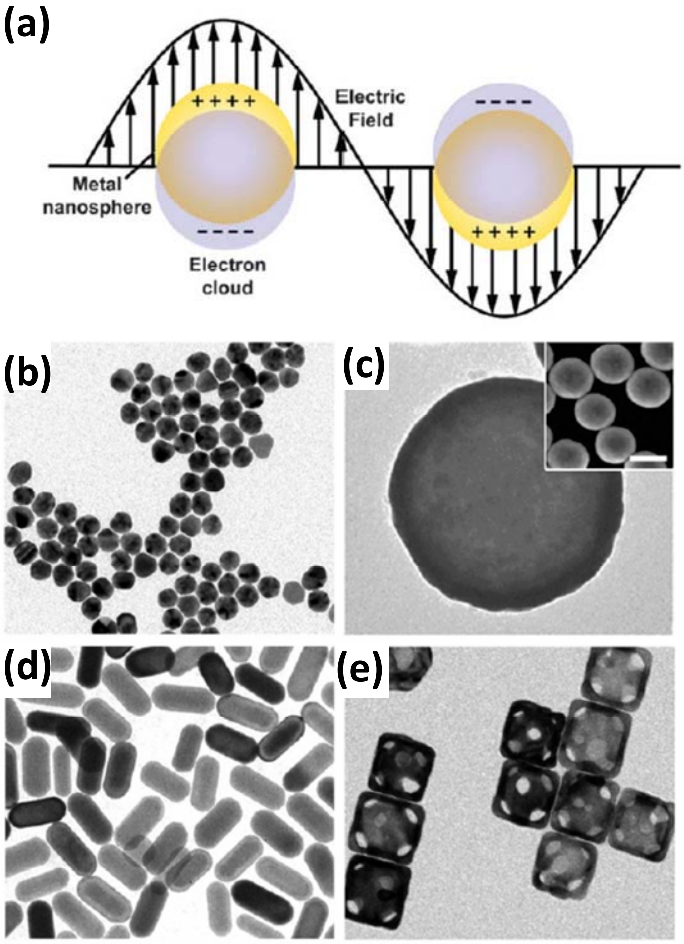

Figure 2.7 (a) Localized surface plasmon resonance (LSPR) is another critical property of gold nanostructures that results from the collective oscillation of delocalized electrons in response to an external electric field. (b) multiply twinned gold nanoparticles. (c) gold nanoshells (silica beads coated with a polycrystalline gold layer). (d) gold nanorods, and (e) gold nanocages. [53] Copyright 2011, Royal Society of Chemistry.

sacrificial template of silver nanocubes (as well as silver nanocrystals with other shapes). When silver nanocubes are titrated with a gold salt (typically $HAuCl_4$), a galvanic replacement reaction occurs, causing gold atoms to be deposited on the surface of the nanocube and silver atoms to be dissolved from a small pit in the surface.

2.3.2 Photoacoustic imaging for gold nanostructure

Recently, several commercially available optical imaging, such as confocal microscopy, two-photon microscopy and optical coherence tomography, have been successful, but none of these technologies can provide penetration beyond ~1mm into scattering biological tissues due to relying on ballistic and qusi-ballistic photons. Photoacoustic imaging, which combines high ultrasonic resolution and strong optical contrast in single modality, has broken through this limitation. Thus, many researchers have interesting in the field of photoacoustic imaging in the past few years. In 1880, Alexander Graham Bell was first reported the photoacoustic effect as a physical phenomenon. However, the photoacoustic imaging technology was developed only after the advent of ultrasonic transducers, computers and lasers [54]. In 2000s, Wang. et al. [55, 56] introduced the fundamentals of photoacoustic imaging technology to lead the generation of this technology development. In photoacoustic imaging, the intensity modulated electromagnetic radiation, e.g., a beam of pulsed laser light, is directed at the imaging target. The light absorbed and converted to an outgoing thermoacoustic wave can be detected by an ultrasound transducer and used to reconstruct images (**Figure 2.8**). Key factors for photoacoustic imaging efficiency are how many incident photons can be absorbed and converted to heat, and how fast generated heat can diffuse out from the target during thermoelastic expansion and wave generation. In order to enhance the photoacoustic imaging signal, the probes used for photoacoustic imaging should be minimally emissive, enhancing conversion of absorbed light energy to heat and subsequently to an acoustic signal. In recent studies, the photoacoustic imaging has been demonstrated successfully using gold nanorods, nanocages, and nanoshells with high and tunable optical absorption cross section. Lihong V. Wang and Younan Xia were reported a new theranostic system with the contrast of photoacoustic imaging and control the release of a chemical or biological effector by high-intensity focused ultrasound (HIFU) [57]. They facile and versatile strategy for loading hydrophobic or hydrophilic drugs into the hollow gold nanocages and use a phase-change material to control the release of drug in response to temperature increase.

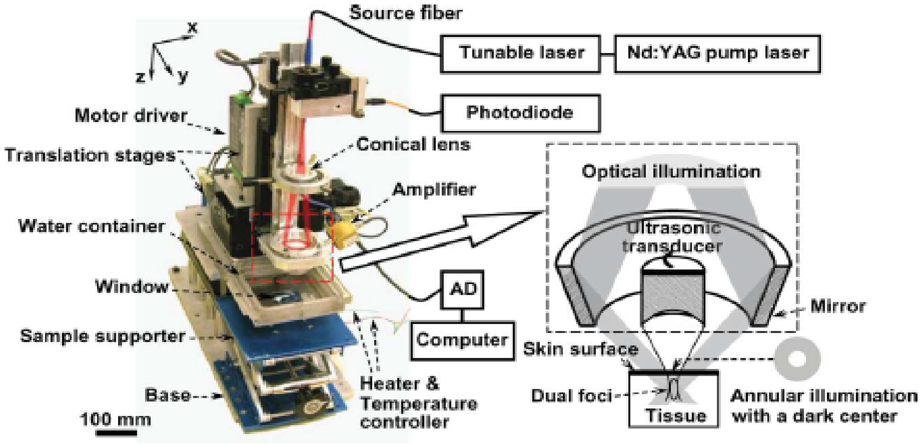

Figure 2.8 Photoacoustic microscopy (PAM) system. Copyright 2008, IEEE.

Recently, Chen et al. introduced a new approach to significantly increase the contrast-to-noise ratio (CNR) of contrast-enhanced nanoparticle augmented photoacoustic imaging by encapsulating gold nanorods within an optically nonabsorbing shell silica material. The role of the silica shell in amplifying the photoacoustic signal highlights the importance of the heat transfer mechanism from the gold nanoparticle to the ambient signal-generating medium. They used the cetyltrimethylammonium bromide (CTAB) stabilized gold nanorods, furthermore, CTAB was replaced by mPEG-thiol through ligand exchange, and then silica was grown onto the PEGylated gold nanorods via the modified Stober method using tetraethyl orthosilicate (TEOS). In addition, it can control the silica thickness with conformal and isotropic silica coating of the gold nanorods (**Figure 2.9**). To discuss the photoacoustic imaging enhancement, the author showed a comparison of ultrasound, photoacoustic, and the spatially coregistered combined ultrasonic and photoacoustic images of phantoms with inclusions containing PEGylated gold nanorods, and gold-silica core shell nanorods with silica shells of 6, 20, and 75 nm thickness, respectively. The PEGylated gold nanorods produced a much weaker photoacoustic signal than that with silica-coated nanorods. As the thickness of the silica shell increases from 6 to 20 nm, the photoacoustic signal increases and, consequently, the photoacoustic image showed brighter. The signal enhancement is slightly reduced for the nanorods with a 75 nm silica shell (**Figure 2.9e**). As a result, silica coating of gold nanoparticles appears to be a simple way to increase their usefulness as contrast agents for photoacoustic imaging.

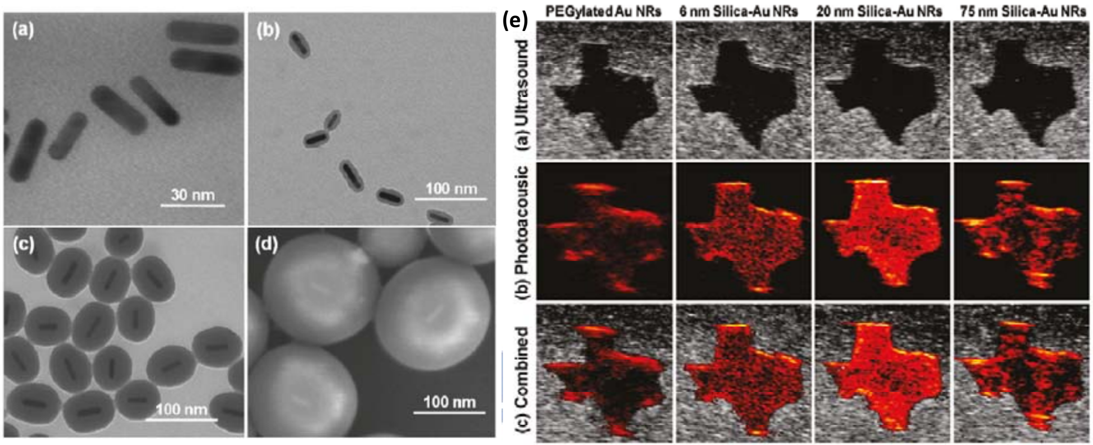

Figure 2.9 (a) TEM image of PEGylated gold nanorods. TEM images of gold-silica core-shell nanorods with (b) 6 nm, (c) 20 nm. (d) 75nm thichness of silica coating.(e) ultrasound, photoacoustic and combined ultrasound and photoacoustic images of PEGylated gold nanorods and gold-silica core-shell nanorods with 6 nm, 20 nm and 75 nm silica coating. [58] Copyright 2011, American Chemical Society.

2.3.3 Gold nanostructures integrate with silica for phtothermal therapy

Recently, near-infrared (NIR) light absorbing plasmonic nanomaterials have attracted intensive attention for their hyperthermia therapy to kill tumorigenic cells without damaging normal cellsm such as gold nanorods, gold nanocages, gold nanoshells and many gold nanocomposites. Here, Liu et al. presented a kind of PEG functionalized gold nanoshells on silica nanorattles for ablation of breast tumor (**Figure 2.10**). They emphasized that the gold nanoshells on silica nanorattles demonstrate positively result for *in vivo* breast tumors in mice show complete regression by the combination of selectively targeting, photothermal therapy and chemotherapy *via* a single irradiation with NIR laser light. In briefly, the gold nanoshell was consists of a thin gold nanoshell and a mondispersed mesoporous silica nanoparticle core. After that procedure, the Methoxy-poly(ethylene glycol)-thiol (mPEG-SH) was attached to the gold via the thiol end groups. Furthermore, the Transferrin (Tf) was also linked to gold silica nanorattles (GSNs) because the carboxylic end of gold silica nanorattles reacted with amine groups on the transferrin via carbodiimide chemistry to form an amide bond. For the photothermal therapy test, an infrared thermal mapping apparatus was used to monitor the temperature increasing when an 808 nm NIR laser light irradiated a MCF-7 tumor-bearing BALB/c nude mouse (< 5 mm × 5 mm). The mouse was intravenously injected with pGSNs-Tf saline solution (200μL, 1 mg mL^{-1}). Then it was anesthetized with sodium pentobarbital and irradiated the tumor region with NIR light (2 W cm^{-2}) at 6 h post-injection. As a result, during this irradiation, the temperature of the tumor bviously increased from 30.5 ° C to 45.7 ° C in the focal region to kill the cancer cells. This proves that pGSNs-Tf is promising as an ideal photothermal converter in cancer therapy.

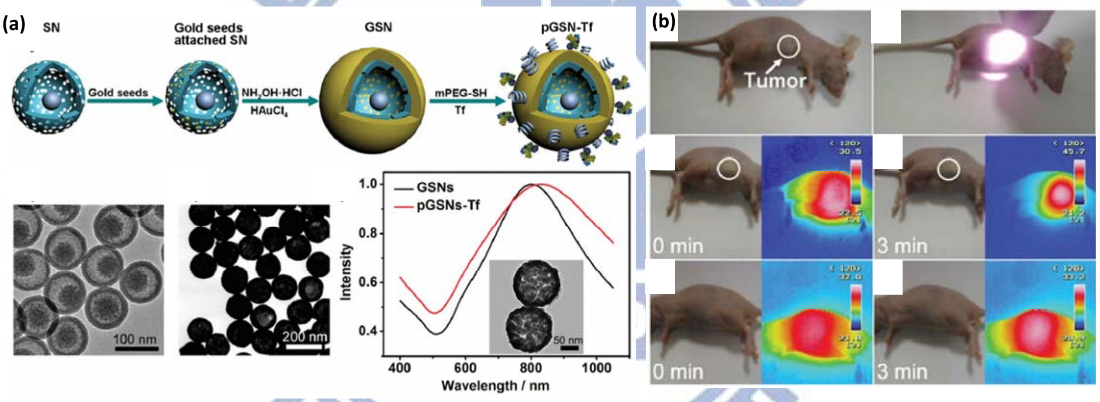

Figure 2.10 (a) Schematic diagram and TEM image of GSNs synthesis and bioconjugation. (b) The photo image of a MCF-7 tumor-bearing BALB/c nude mouse under an 808 nm NIR laser light irradiation. [59] Copyright 2012, Wiley-Vch.

2.4 Magnetic nanoparticles for biomedical applications

Controlled drug release from nanofunctional materials, especially magnetic nanoparticles, is attracting increasing attention due to their potentials in cancer therapy and treatment of other ailments. The magnetic nanoparticles stems from intrinsic properties of their magnetic properties combined with their drug loading capability and the biochemical properties that can be bestowed on them by mean of a suitable coating [60]. Preparation methods of NPs generally fall into the category of so-called “bottom up” method, where nanomaterials are prepared from atoms or molecules in a controlled manner that is thermodynamically regulated by means such as self-assembly. Some biomedical applications require core-shell magnetic nanoparticles. They have a metal or metallic oxide core, which is encapsulated in an inorganic or a polymeric coating that renders the particles biocompatible, stable and may serve as a support for drug or biomolecules. Their magnetic properties make these particles to be used in numerous applications, belongingto one or more than the following groups: (i) magnetic contrast agents in magnetic resonance imaging (MRI) (ii) Hyperthermia agents, where the magnetic particles are heats selectively by applications of a high frequency field. (iii) Magnetic targeting can be directly by means of a magnetic field gradient towards a certain location.

Freeman et al. reported in 1960 that the magnetic nanoparticles could be transported through the vascular system and concentrated in a specific part of the body with the aid of a magnetic field. Since in 1970, the magnetic particles were used to the delivery of chemotherapeutics. In 1976, Zimmermann and Pilwat applied magnetic erythrocytes for the delivery of cytotoxic drugs and Widder et al. proposed the targeting of magnetic albumin microspheres encapsulating an anticancer drug (doxorubicin) in animal models. In 1980, many studies reported the strategy to delivery different drugs using magnetic microcapsules and microspheres. However, before the 1980s, all researches were focus on microsized. In 1996, the first Phase I clinical trial was carried out by the same group in patients with advanced and unsuccessfully pretreated cancers using magnetic nanoparticles loaded with eqirubicin. However, in that first trial, more than 50% of magnetic nanoparticles were accumulated in the liver. Since that, a number of groups have designed and fabricated magnetic micro- or nano- particles, which used in MRI, hyperthermia, cell sorting, magnetic targeting, enzyme immobilization, and gene transfection detection systems.

2.4.1 Synthesis of magnetic nanoparticles

The synthesis of iron oxide nanoparticles has been received a great attention by chemists and material scientists for nearly the last half a century. Early studies have developed a number of methods, such as physical mechanogrinding, gas phase vapor deposition, sol-gel process, and coprecipiation of ferrous and ferric salts. Recently, in the synthesis of highly in the middle of 1990s opened up new efficient synthetic routes to produce monodispersed nanoparticles. For biomedical applications, the two most common aqueous syntheses of iron oxide nanoparticles are alkaline coprecipitation and microemulsion based precipitation/oxidation of ferrous and ferric salts (Fe^{3+} and Fe^{2+}). Iron oxide NPs can be obtained on a large scale by aging a stoichiometric mixture of inorganic salts in aqueous media. A series of experimental parameters, such as pH, reaction temperature, and precursor, have been studied to control NP morphology, size, and quantity. The solvothermal process uses a high pressure reaction to obtain well-crystallized MNPs. However, using these two methods it is difficult to produce magnetic nanoparticles with a narrow size distribution. This is further compounded by the use of surface coatings which introduce large hydrodynamic size variability. Briefly, iron oxide are coprecipitated under aqueous conditions with a strong base to yield the magnetic nanoparticles which can be either complexed with surface coating in a one-pot fashion or after purification and dispersion in a multistep procedure. Although it is difficult to achieve control of the nanoparticle size with nanometer precision and crystallinity with high fidelity via the aqueous based synthesis, magnetic nanoparticles have been widely used as MRI contrast agents, bioseparation agents and drug delivery vectors [61].

A significant evolutionary in the control over size and properties of magnetic nanoparticles occurred with movement away from low-temperature hydrolytic synthesis techniques toward organometallic procedures carried out at higher temperatures. In 1979, Griffiths et al. developed the thermal decomposition of iron pentacarbonyl in a dilute solution of functional polymers in organic solvent at relatively elevated temperatures (~150^{o}C) to obtain single domain (10-20 nm) and single domain superparamagnetic (< 10 nm) colloidal Fe and Fe oxide [62]. Bawendi et al. proposed metal-alkyl precursors, surface coordinating ligands, and high boiling point solvents for the high quality and efficient elevated-temperature organic-phase synthesis of semiconductor nanocrystals [63, 64]. These techniques have demonstrated well-controlled size, high monodispersity, and enhanced magnetic properties. Major improvements of this approach by Hyeon et al. utilized iron pentacarbonyl precursors and oleic acid as the surfactant for the synthesis of maghemite nanoparticle [65], followed by additional optimization wherein the large-scale magnetic nanoparticle synthesis with size control was demonstrated [66]. (**Figure 2.11**) A systematic study of the reaction kinetics of magnetic nanoparticles by Hyeon et al. has shown that the "heating up" method follows a similar size distribution control mechanism as the "hot injection" synthesis technique, wherein a sudden burst in nucleation is succeeded by rapid size distribution narrowing and a high growth rate. [67]

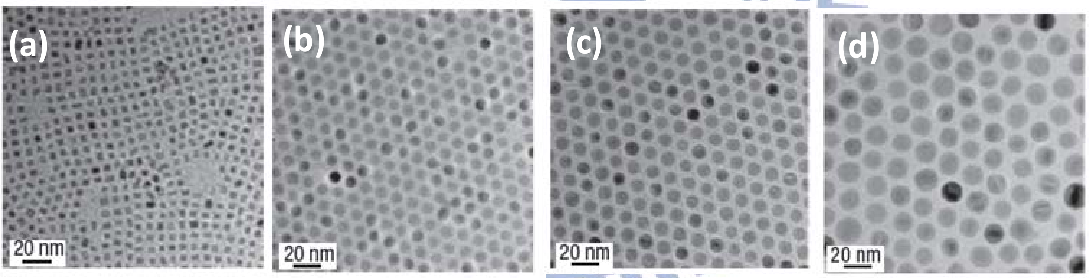

Figure 2.11 TEM micrographs of iron oxide nanoparticles with diameter of (a) 6 nm, (b) 9nm, (c) 12 nm and (d) 16 nm. Copyright 2004, Nature Publishing Group.

2.4.2 Magnetic nanoparticles for high performance magnetic resonance imaging and guiding effect

Magnetic resonance imaging (MRI) has been regarded as a powerful imaging tool as a result of its noninvasive nature, high spatial resolution and tomographic capabilities, but its low signal sensitivity has been a major limitation. For the past two decades, synthetic iron oxide nanoparticles such as dextran-coating superpara -magnetic iron oxide (SPIO) have served as contrast-enhancing probe for MRI. [68, 69] These magnetic nanoparticles are now clinically used for improving anatomical magnetic resonance contrast and have also been used in molecular imaging, gene expression, cancer, angiogenesis imaging, and cellular trafficking [70-73]. However, since most of such iron oxides are prepared through conventional water-phase synthetic protocols, there tends to be difficult to achieve highly well-defined nanocrystalline size, stoichiometry, and magnetism, which in turn results in rather poor MR signal-enhancing effect. To enhance MR contrast effects and to functionalize versatile surface groups for advanced molecular imaging, researchers have been developeing next generation magnetic nanoparticle probes. For example, rapid advances in non-hydrolytic thermal-decomposition synthetic methods for preparing monodispersed magnetic nanoparticles have offer to synthetically control the important features of these probes, such as size, magnetic dopants, magneto-crystalline phase, and surface states,[74-76] resulting in the discovery of designed functional magnetic nanoparticles. These innovative nanoparticle probes exhibit superior magnetism and MR contrast effects which have been shown to be better than that of conventional MR contrast agents [77-80].

The size of magnetic nanoparticles is one important parameter for MR contrast enhancement effect. For the bulk materials, the magnetic spins are aligned parallel to the external magnetic field. However, in the nanoscale size, surface spins tend to be slightly tilted to cause a magnetically disordered spin-glass-like surface layer effects of magnetic nanoparticle influence their magnetic moments and MR contrast enhancement effects. This effect is size dependent and is well demonstrated in the case of magnetism engineered iron oxide nanoparticles, where the variation of their size from 4 nm to 6nm, 9 nm and 12 nm result in magnetization values of 25, 43, 80 and 102 emu per gram Fe, respectively (**Figure 2.12**) and such a trend is clearly observed from MR signals.

On the other hand, for magnetic property, molecular targeting relying on the binding between a targeting ligand and a cancer-specific receptor has been widely applied to enhance the tumor homing of nanomaterials. However, the patient-to-patient variation in receptor

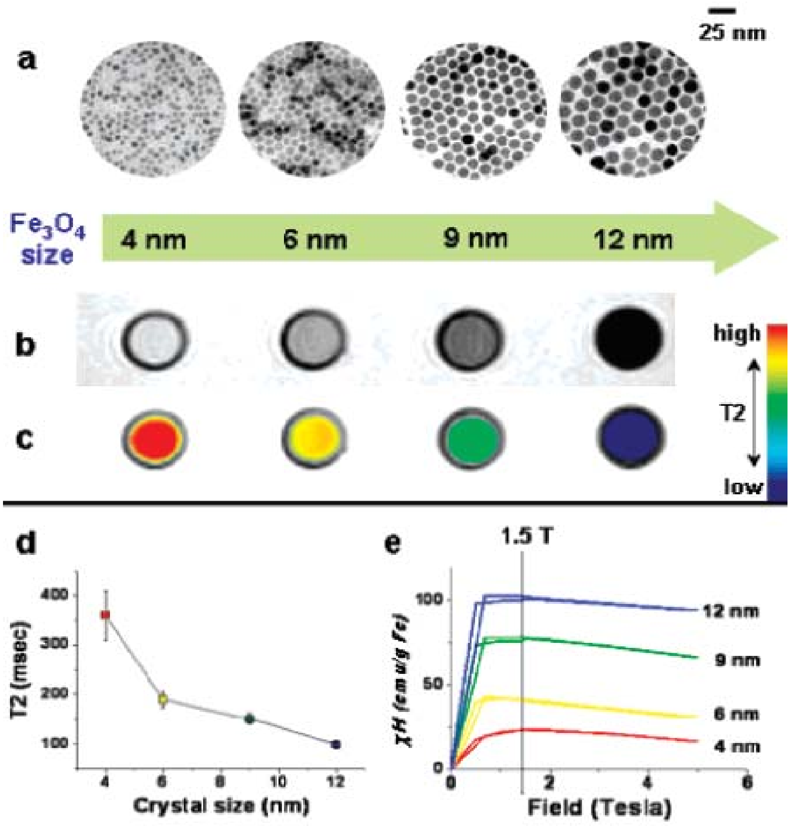

Figure 2.12 Nanoscale size effect of magnetic nanoparticles on magnetism and induced MR signals. (a) TEM images of Fe3O4 nanoparticles of 4 to 6, 9, and 12 nm. (b) Size-dependent *T*2-weighted MR images of magnetic nanoparticles in aqueous solution at 1.5 T. (c) Size-dependent changes from red to blue in color-coded MR images based on *T*2 values. (d) Graph of *T*2 value versus magnetic nanoparticles size. (e) Magnetization of magnetic nanoparticles measured by a SQUID magnetometer. [81] Copyright 2005, American Chemical Society.

expression levels and the non-specific expression of receptors in normal tissues, due to these factors largely limit the clinic applications of this strategy in cancer therapies. Recently, magnetic targeting employs a magnetic field to attract magnetic nanoparticles circulating in the blood to the tumor site where the magnet is placed. Different from molecular targeting, magnetic targeting based on physical interactions is not limited by the specific receptor expression, and may be a more general tumor-targeting approach. In the past years, the magnetically targeted delivery has been demonstrated by a number of different reports, including *in vivo* drug delivery system and gene delivery system, which could be a useful anti-tumor strategy and delivery stem cells or gene in injury site.

2.4.3 Magnetic nanoparticles/silica core-satellite structure for dual-mode imaging

The multifunctional nanoparticle was investigated by using magnetic nanoparticles and mesoporous silica forming core-satellite structure [82]. In **Figure 2.13a**, this work presented the multiple fluorescent dyes and mutilple magnetic nanoparticles into a single nanoprobe that provides superior fluorescence and MR imaging capabilities through the synergistic enhancement of its respective components. This design was fabricated new "core-satellite" structured dual functional nanoparticles comprised of a dye-doped silica "core" and multiple "satellites" of magnetic nanoparticles.

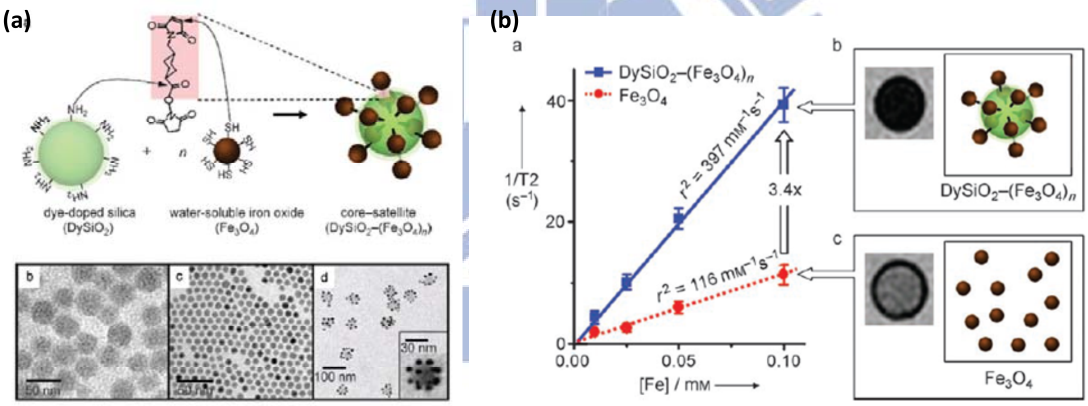

Figure 2.13 (a) Schematic diagram for the synthesis of core–satellite DySiO$_2$–(Fe$_3$O$_4$)$_n$ nanoparticles. (b) Synergistic MR enhancement effect of DySiO$_2$–(Fe$_3$O$_4$)$_n$. T$_2$ relaxivity coefficients (r$_2$ and T$_2$-weighted) MR images of DySiO$_2$–(Fe$_3$O$_4$)$_n$ nanoparticles and free Fe$_3$O$_4$ nanoparticles. Copyright 2006, Wiley-Vch.

Rhodamin-dye-doped silica (DySiO$_2$) nanoparticles with surface amine groups were conjugated with 9 nm magnetic iron oxide nanoparticles by using sulfosuccinimidyl-(4-N-maleimidomethyl) cyclohexane-1-carboxylate (sulfo-SMCC, Pierce) cross-linkers. Using a clinical MRI instrument, the MR contrast effect of DySiO2–(Fe3O4)$_n$ nanoparticles in comparison with that of free magnetic iron oxide nanoparticles with the same iron concentration was examined. In the spin–spin relaxation time (T$_2$) weighted spin echo

MRI at 9.4 T, the free magnetic iron oxide nanoparticles show weak MR contrast with a T_2 relaxivity coefficient (r_2) of 116 mm^{-1} s^{-1} (**Figure 2.13b**). In contrast, the DySiO2–$(Fe3O4)_n$ nanoparticles provide a remarkably dark MR contrast of an approximate 3.4-fold increased T_2 relaxivity coefficient of 397 mm^{-1} s^{-1}. Such a significant improvement in the MR signal arises from the synergistic magnetism of multiple Fe_3O_4 satellites surrounding a core silica nanoparticle. Furthermore, the DySiO2–(Fe3O4)n nanoparticles exhibit enhanced fluorescence behavior at 580 nm of rhodamine dye molecules with approximately 1.7-times more intense emission, compared with that of directly conjugated rhodamine- Fe_3O_4 nanoparticles.

2.4.4 Magnetic nanoparticles for stem cell therapy

Tissue autotransplantation has been developed a well-established tool for the treatment of tissue damage or loss resulting from traumatic insult, oncological resection, congenital deformities, or progressive degenerative diseases. However, it is hampered by complicated surgical procedure and severe tissue donor shortages in clinical practices. Although the tissue allotransplantation has great potential for reconstructive surgery, the low number of human leukocyte antigen (HLA) compatible donors and the disproportionately high demand for suitable graft tissue, result in this procedure difficulty to widespread implementation. Therefore, the new generation of curing human diseases was opened. The “stem cells” can yield almost any cell in the human body and are capable of developing into almost any tissue, including bone, muscle, nerve, and blood. Thus, they represent an important building for regenerative medicine and tissue engineering due to their powerful reparative potential. The stem cells also represent a unique opportunity to cure a broad range of significant human diseases, such as stroke, Parkinson’s disease, myocardial infarction, and muscular dystrophy, for which existing therapies only alleviate symptoms or retard further disease progression. Of note, stem cell-based therapy is being clinically explored and will likely become more clinically relevant in the future

In 1960s, Joseph Altman and Gopal Das presented scientific evidence of adult neurogenesis, ongoing stem cell activity in the brain; their reports contradict Cajal's "no new neurons" dogma and are largely ignored. In 1963, McCulloch and Till illustrated the prescence of self-renewing cells in mouse bone marrow. To the 1998, Thomson et al. derive the first human embryonic stem cell line, resulting in beginning the generation of stem cells therapy technology. Recently, many researchers have been developed the stem cell-based therapy technology [83-85]. However, there are still exist some problems for stem cell-based therapy, such as (1) from intravenous injection, almost 90% stem cells were metabolized to the liver and lung, less than 10% moving to the target site. (2) stem cell-based therapy requires monitoring the fate and distribution of transplanted cells to maximize the therapeutic benefit. Thus, two key points for stem cells therapy are how to determine and track the quantity of stem cells in the location and how to home the stem cells to the target site.

In **Figure 2.14**, the authors use a unique class of nanoparticles with both upconversion luminescence (UCL) and superparamagnetic properties for stem cell research. Those MFNPs after functionalized with polyethylene glycol were used for upconversion luminescence (UCL)/magnetic resonance multimodal imaging as well as magnetically targeted photothermal ablation of cancer in vitro and in vivo. For the stem cell tracking, they use the UCL optical and MR imaging techniques to investigate the location of stem cell and determine the quality of stem cells. In addition, MFNP-labeled stem cells are tracked after being intraperitoneally injected into wound-bearing mice under a magnetic field. The translocation of stem cells from the injection site to the wound nearby the magnet is observed and, intriguingly, a remarkably improved tissue repair effect is observed as the result of magnetically induced accumulation of stem cells in the wound site.

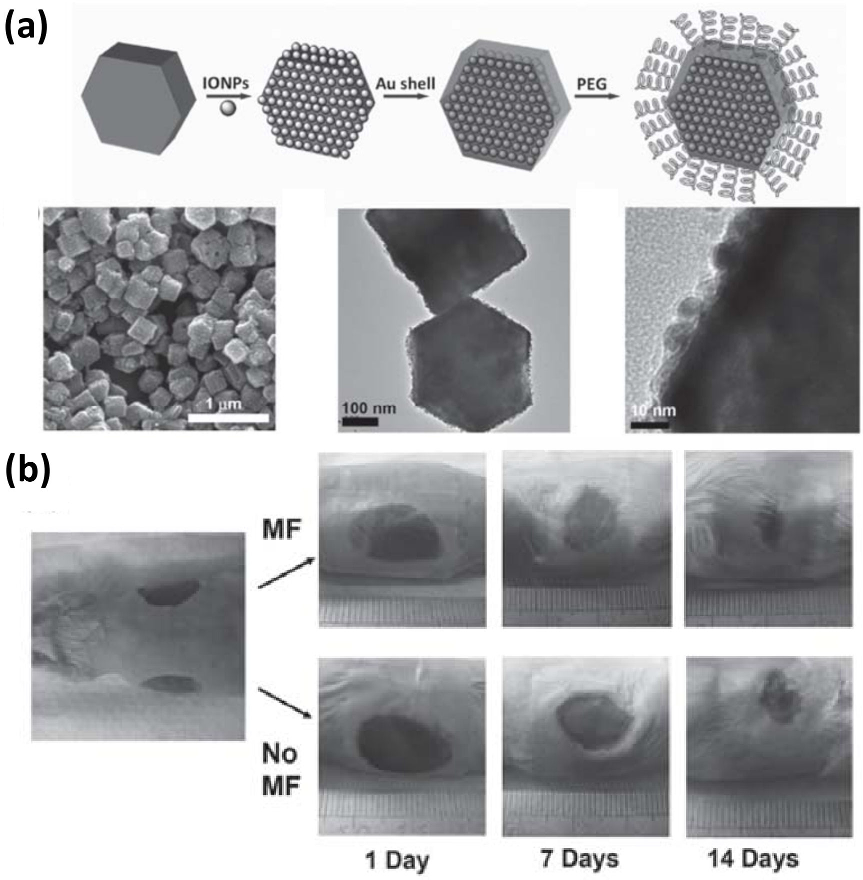

Figure 2.14 (a) A schematic illustration showing the composition of MFNP-PEG and SEM, TEM image of MFNPs. (b) Magnetic field induced tissue repairing of gradual closure of the wounds over time after mice were treated with MFNP-labeled mMSCs. Upper and lower rows of photos showed the left side (with magnet) and right side (without magnet) wounds, respectively, of a representative mouse. [86] Copyright 2012, Wiley-Vch.

Jokerst et al. use silica-coated gold nanorods as a photoacoustic contrast agent to label stem cells and quantitation of mesenchymal stem cells in rodent muscle tissue. Due to silica-coated gold nanorods, it enhanced the photoacoustic signal of gold nanorods and increased uptake of the gold nanorods into the cell. This approach has significant advantages over traditional cell imaging techniques like positron emission tomography and magnetic resonance imaging including real time monitoring of stem cell therapy. On the other hand, Li et al. use a doxorubicin-silica nanorattle drug delivery system to stem cells as a “time bomb” for tumor-tropic therapy (**Figure 2.15**) [87]. They upload the drug-loaded nanorattle to the stem cell by bioconjugated with a monoclonal antibody for specifically binding with the stem cell’s membrance proteins. The obtained time bomb of DOX-nanorattle labeled stem cells was able to migrate toward the giloma xenograft showing more extensive and prolonged drug accumulation in tumor tissues.This strategy prospectively provides an attractive foreground for using MSC-anchored nanoparticulate drug delivery systems for targeted tumor therapy with high efficiency.

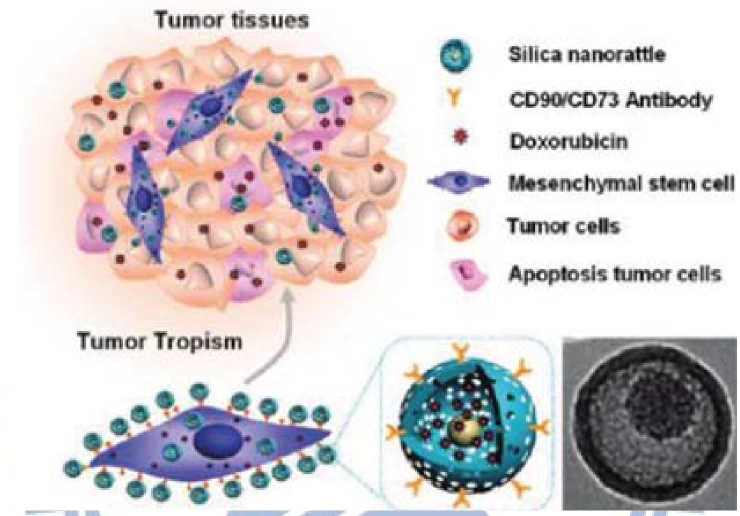

Figure 2.15 Scheme of silica nanorattle_doxorubicin-anchored mesenchymal stem cells for tumor-tropic therapy. Copyright 2011, American Chemical Society.

Chapter 3

Experimental Procedures

3.1 Experimental overviews

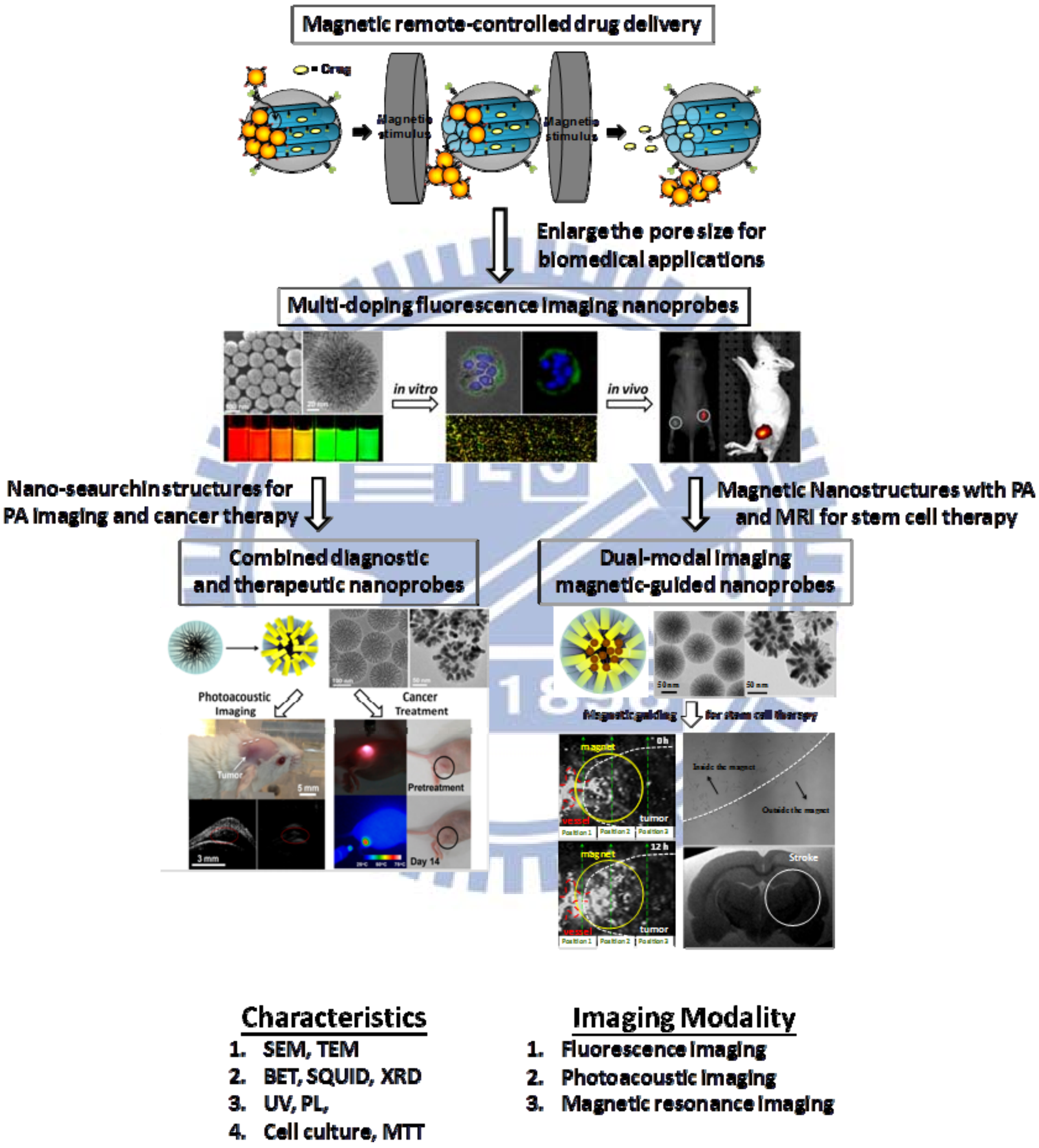

3.2 Characterization

The morphologies of the nanoparticles were investigated using scanning electron microscopy (SEM, JSM-6700F, Japan), transmission electron microscopy (TEM, JEM-2010, Japan). For SEM analysis, the nanoparticles were dried on 0.5 × 0.5 cm silicon. After drying, the nanoparticles were coated with an ultrathin layer using platinum sputtering to enhance the image quality. The magnetic property of iron magnetic nanoparticles was estimated by superconducting quantum interference device (SQUID, MPMS-XL7) at 298K with the magnetic field sweeping from -10000 to +10000 G. The BET analysis (Quantachrome, NOVA 2000, USA) was conducted using N_2 gas absorption isotherms at 77K, and the pore size were calculated following the approach by Barrett, Joyner and Halenda (BJH). The nanoparticles were degassed for 250^{o}C, 2hours before BET analysis. The fluorescent images were recorded by IVIS Spectrum (IVIS Imaging System 200 Series, Caliper Life Sciences, USA). Living Image software Version 3.0 (Xenogen) was used to acquire and quantitate the fluorescence. The images showing fluorescence of nanoparticles was captured using excitation (Ex), 500 nm and emission (Em), 540 nm/600nm. Spectrally unmixed images were captured using a sequence of Ex, 500 nm and Em, 540 nm/560 nm/580 nm/600 nm. For advanced fluorescence imaging, the IVIS Spectrum used epi-illumination (from the top) to illuminate in vivo fluorescent sources. After whole-body imaging, the mice were euthenized by overdosed CO_2.

3.3High frequency magnetic field (HFMF)

The strength of the magnetic field in these systems depends on the cooper coil which had eight loops with frequency of 50 kHz and magnetic field strength (H) of 2.5 kA/m. The temperature of HFMF generator was controlled by cycling cooling water at 25 ^{o}C. The heating effects of magnetic nanoparticles submitted to high frequency magnetic fields (HFMF) are due to several types of loss processes (hysteresis losses, Neel and Brown relaxation), the relative contributions of which depend strongly on particle size. The magnetization relaxation is governed by the combined effects of the rotational external (Brown) and internal (Neel) diffusion of the particle magnetic moment. The Brown relaxation is due to thermal orientational fluctuations of the grain itself in the carrier fluid, the magnetic moment being locked onto the crystal anisotropy axis. The equation is given by: $\tau_B = 3\eta V_H/kT$, where η is the viscosity of the carrier fluid, k is the Boltzmann constant, T is the temperature and V_H is the hydrodynamic volume of the particle. The Neel relaxation is the internal thermal rotation of the particle's magnetic moment within the crystal, which occurs when the anisotropy energy barrier Ea = KV, where K is the anisotropy constant of the magnetic material, and V is the magnetic particle volume. The equation of Neel relaxation is given by $\tau_N = \tau_0 \exp(Ea/kT)$, where τ_0 is the order of 10^{-9} s. As the two relaxation mechanisms take place in parallel, the effective relation time τ is given by the relationship: $1/\tau = 1/\tau_N + 1/\tau_B$.

3.4 Ultrasound and photoacouistic imaging system (PA)

The schematic of photoacoustic imaging system is shown in **Figure 3.1**. The high-frequency (>20 MHz) dark-field confocal photoacoustic microscopy (PAM) is demonstrate the characteristics of nanoaprticles as photoacoustic imaging (PAI) contrast agents. Laser pulses were provided at different wavelengths using an optical parametric oscillator (Surlite OPO Plus, Continuum) pumped by a frequency-doubled Nd:YAG Q-switched laser (Surlite II-10, Continuum) with pulse width of 6.5 ns and pulse repetition frequency (PRF) of 10 Hz. The 50- MHz ultrasonic transducer of the PAM system was custom-made by the Resource Center for Medical Ultrasonic Transducer Technology at the University of Southern California. It had a 6-dB fractional bandwidth of 57.5%, a focal length of 9 mm, and a 6-mm active element, offering axial resolution of 36 mm and lateral resolution of 65 mm. During the imaging process, the transducer was immersed in a water tank with a hole in the bottom that was sealed with a piece of 15-mm-thick polyethylene film. The wavelength of the OPO laser was tuned starting at 808 nm to expose different samples at the particular peak value of their optical absorption. Laser exposure was adapted to 4~20 mJ/cm^2 for all the experiments.

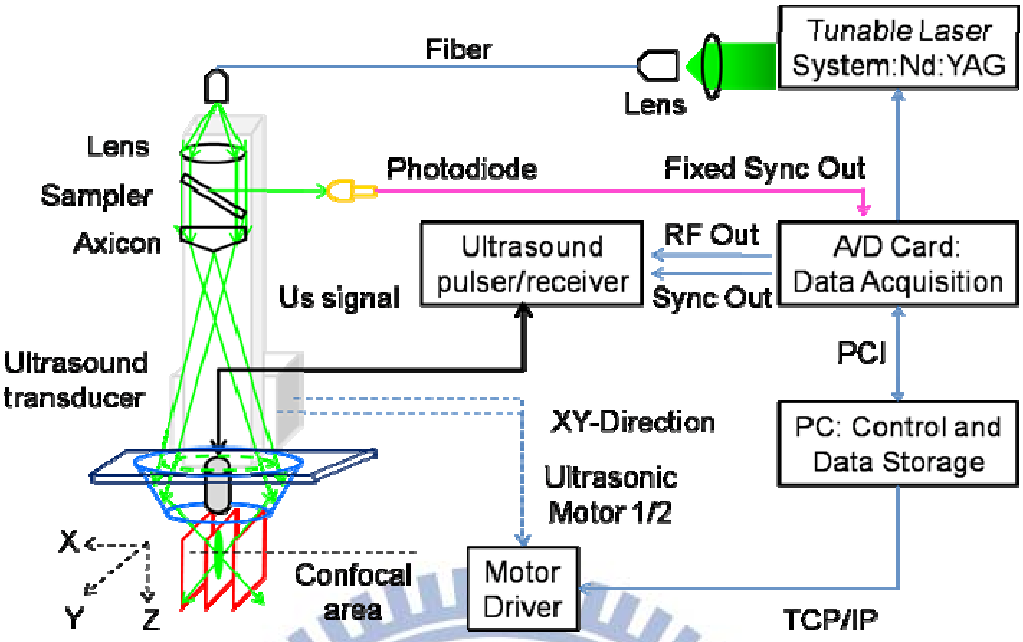

Figure 3.1 The photograph of the ultrasound and photoacoustic imaging system.

3.5 Cell culture

Four cell lines were used as cancer cell models: A549 (human lung cancer), MCF-7, MDA-MB-231 (human breast cancer), and HeLa (human cervix cancer) cells were maintained in DMEM (Dulbecco's modified Eagle's medium) containing 10% fetal bovine serum, 100 units/ml penicillin, and 100μg ml^{-1} streptomycin. Cells were cultured with complete medium at 37^{o}C in a humidified atmosphere of 5% CO$_2$ in air. For all experiments, cells were harvested from sub-confluent cultures by use of trypsin and were resuspended in fresh complete medium before plating. A comparison of in vitro cytotoxicity of nanoparticles with different concentrations was performed on cells with an in vitro proliferation method using MTT. Briefly, 10^4 cells were plated in 96-well plates to allow the cells to attach and then exposed to the serial concentrations of nanoparticles at 37^{o}C. After the nanoparticles incubated with cells for 24 h, 20 μL of MTT solution was added and incubated for another 2 h. Then, the medium was replaced with 200 μL of DMSO, and the absorbance was monitored using a Sunrise absorbance microplate reader at dual wavelengths of 570 and 650 nm. To estimate the cellular uptake of the nanocarriers, the green emitting FITC attached to the nanoparticles for the study. The FITC-labled nanoparticles were incubated with the cells for 2 hours and then studied by confocal microscopy (CLSM, Nikon, C1) and flow cytometry.

3.6 *In vivo* experiment

Subcutaneous tumors were induced in either the left hind flank of nude mice after injection of about ten million cells in 0.1 mL media. Tumors were allowed to grow to ~100 mm^3 before experimentation. The cancer cells xenograft nude mice were given single injection of the nanoparticles *via* intracortical injection. The concentration of particles administered were 0.5 μM given in 50 μL injection. Then it was anesthetized with isoflurane and irradiated the tumor region with NIR light (4 W cm^{-2} for 2 min) at 12 h post-injection and use infrared thermal mapping apparatus to monitor the temperature raise. For in vivo photoacoustic imaging experiment, the mouse (Balb/c) were induced tumors subcutaneously in the head after injection of about million cells (CT26, mouse colon cancer) in 0.1 mL media. The mouse was given single injection of nanoparticles (0.5 μM, 50 μL) via intracortical injection. Then the mouse was restriction of movement in the fixer. A frequency-doubled pulsed laser with 10-ns pulse width pumped an optical parametric oscillator to illuminate the tumor site at 808 nm wavelength and 10 mJ/cm^2 fluence.

Chapter 4

Multifunctional Magnetically Removable Nanogated Lids of Fe_3O_4–Capped Mesoporous Silica Nanoparticles for Intracellular Controlled Release and MR Imaging

4.1 Introduction

Controlled release of therapeutic agents from nanometric carriers has received increasing attention in recent years. The nanocarriers can be made of various biocompatible nanomaterials with a specifically designed structure, facilitating drug release from inside via specific stimuli, such as temperature,[88,89] pH,[90,91] electric field,[92] ultrasound,[93,94] chemicals,[95-97] and magnetic field,[98-100] in a therapeutically desirable manner. In particular, functional nanoparticles have been extensively investigated as probes in biomedical imaging due to their unique size-dependent electronic, optical, and magnetic properties. Many traditional stimuli, such as electric signals, mechanical forces, and pH, usually need a physical contact or chemical reaction with the drug carriers to trigger drug release. However, triggering a drug release in such a manner may not be practicable in the human body. Furthermore, real-time release with a short-time stimulus is difficult to achieve with traditional stimuli-responsive polymeric materials, which is especially critical for certain clinical applications. Therefore, the development of a desired drug carrier for medical applications should possess remote-controlled properties as well as real-time responsiveness to the stimuli, for example, when urgent disease control measures and/or a slow, sustained release to meet different clinical applications are required.

Recent reports on surface-functionalized iron oxide nanoparticles have demonstrated their feasibility for use in a variety of biological applications such as drug/gene delivery,[101-105] magnetic resonance imaging,[106,107] bioseparation,[108,109] tissue repairing,[110] and hyperthermia therapy.[111,112] In contrast, there are a limited number of reports addressing the use of magnetic nanoparticles for controlled drug delivery. However, a combined functionality with magnetic resonance (MR) imaging capability and drug-carrying functions employing the superparamagnetic iron oxide nanoparticle as a multifunctional nanosystem for biomedical applications has become an interesting and important research objective very recently.[113] More recently, a number of investigations has highlighted an important class of nanocarriers made of a nanoporous silica matrix, known as MCM-41, for instance, where therapeutic or biologically active molecules can be filled and anchored into the nanopores of the silica nanoparticles, followed by a subsequent free-diffusion release from the nanopores after administration to the site of disease. On the other hand, the MCM-41 type mesoporous silica has several attractive features, such as a stable mesoporous structure, large surface area, tunable pore size and volume, and well-defined surface properties. Combining different nanostructured materials will enable the development of multifunctional nanomedical platforms for imaging, diagnosis, and therapy.[114-116] Recently, Prasad et al. reported the fabrication of multifunctional nanoprobes for imaging live cancer cells by co-encapsulation of quantum dots and magnetite nanoparticles within organically modified silica. They also fabricated a biocompatible ferrofluid containing dye functionalized magnetite nanoparticles and demonstrated optical tracking of basic processes at the cellular level combined with magnetophoretic manipulation.[117] However, undesirable leakage of the drug from the nanopores during the course of delivery is problematic. A recent report by Meng's group,[118] who used organic capping molecules to block the pores from undesirable drug leakage after reaching the diseased sites, showed that the drug was released by chemical removal of the capping molecules. However, a chemical contact triggering reaction for drug release in the human body may cause complications.

Here, we report a new drug-release nanosystem, which is expected to overcome the undesirable complications mentioned above and provide multiple advantages including leakage free, site-specific delivery, sustained release, and imaging capability. The new drug delivery nanosystem is constructed by chemically capping Fe_3O_4 nanoparticles onto the surface of a MCM-41 type mesoporous silica, while drug molecules (here we used a dye molecule (FITC) and an anticancer drug, (S)-(+)-Camptothecin (CPT)) were encapsulated into the pores. With a magnetic trigger, the Fe_3O_4 nanocaps can be removed from surfaces of mesoporous silica vehicles due to the breaking of chemical bonds and then subsequently lead a fast-responsive drug release. The intracellular magnetically trigger anticancerous drug release is also carried out for cancer therapy. The integration of magnetite nanoparticles on the silica surface synergizes the potential of the nanosystem capable of MR imaging, fluorescence imaging, preventing drug leakage, and manipulating drug release under exposure of an external magnetic field. This new drug delivery nanosystem, to the best of our knowledge, is the first report in the field where a magnetically controlled sustain release for intracellular nanotherapeutics can be easily manipulated for practical demands.

4.2 Experimental section

Synthesis of 3-aminopropyltrimethoxy silane-functionalized mesoporous silica nanoparticles (amine-MSN): Cetyltrimethylammonium bromide (CTAB, 1 g) was dissolved in a mixture of distilled water (480 ml) and 2.0 M sodium hydroxide (3.5 ml). The solution was heated to 80^{o}C. Once the temperature of the CTAB solution stabilized, tetraethylorthosilicate (TEOS, 5 ml) and 3-aminopropyltrimethoxy silane (APTMS, 0.97 ml) were added and stirred magnetically for 2 hours. After 2 hours, the solution cooled to room temperature. The products were collected by centrifugation at 6000 rpm for 10 min and then washed with an excess of pure methanol 3 times. To remove the surfactants (CTAB) from the pores of the particles, the particles were dissolved in a mixture of hydrochloric acid (37.5%, 9 ml) and methanol (180 ml). Subsequently, the solution was refluxed for 24 hours. The particles were collected by centrifugation at 6000 rpm for 10 min and then washed with an excess of pure methanol 3 times. The product, mesoporous silica nanoparticles, was centrifuged to remove solvent and redispersed into distilled water.

Synthesis of Fe_3O_4 nanoparticles modified by meso-2,3-dimercaptosuccinic acid (DMSA): Monodisperse iron oxide nanoparticles were synthesized using a method developed by Sun et al.. Briefly, 5 nm of iron oxide nanoparticles were synthesized by mixing 2 mmol $Fe(acac)_3$ (iron III acetylacetonate), 10 mmol 1,2-hexadecanediol, 6 mmol oleic acid, 6 mmol oleylamine, and 20 mL benzyl ether under a flow of nitrogen. The mixture was stirred magnetically and preheated to reflux (200 ^{o}C) for 30 min, and then, heated to 300 ^{o}C for another 1 h under nitrogen atmosphere. The black-brown mixture was allowed to cool to room temperature and added 50 mL ethanol to participate. The products were collected by centrifugation at 6000 rpm for 10 min and then 4 times washed with an excess of pure ethanol. The product, iron oxide nanoparticles, was centrifuged to remove solvent, and redispersed into 30ml chloroform. The *meso*-2,3-dimercaptosuccinic acid (DMSA, 0.1g) was added into 10ml chloroform which contained iron oxide nanoparticles and stirred magnetically for 24 hours. The products were collected by centrifugation at 6000 rpm for 10 min and then washed with tetrahydrofuran (THF) 3 times. Finally, the particles were redispersed into distilled water.

Loading (S)-(+)-camptothecin(CPT) into MSN: To load the drug (S)-(+)-camptothecin(CPT) into the pores of the MSN particles, we followed the method by Lu et al.. The MSNs were soaked in the solution containing (S)-(+)-camptothecin (CPT, 5 mg) and DMSO (3 ml) and then stirred magnetically. After 24 hours, the products, drug-loaded MSNs were dried under vacuum to remove DMSO and then washed 3 times with PBS (PH 7.4) solution to remove CPT, which was on the surface and not inside the pores.

Synthesis of Fe_3O_4 NP-capped MSNs: The MSNs (1 ml) and DMSA-Fe_3O_4 NPs (2 ml) were first mixed together, and then distilled water was added up to 5 ml. Subsequently, the solution was added with 1% 1-ethyl-3-(3-dimethylaminopropyl) carbodiimide (EDC, 300 μl) and stirred magnetically for 24 hours. After 24 hours, the products were centrifuged at 6000 rpm for 10 min and then washed 3 times with distilled water. The MSN@Fe_3O_4 was redispersed into distilled water.

Drug, (S)-(+)-camptothecin(CPT), releasing: The clear solution without the nanospheres was used to estimate the concentration of drug release UV–vis spectroscopy (Agilent, 8453 1UV-Visible spectrophotometer) was used for characterization of absorption peak at 366nm (I_{max} of free CPT). The nanocarriers were absent and did not affect the measurements.

4.3 Preparation of MSN@Fe_3O_4 nanocarriers

The synthesis of MSN@Fe_3O_4 nanoparticles is schematically illustrated in **Figure 4.1**. The first step is to synthesize the MCM-type silica matrix with functionalized 3-aminopropyltrimethoxy silane to give amine groups along the silica surface (**Figure 4.2a**). The drug molecule ((S)-(+)-Camptothecin) (CPT) was filled into the pores of the amine-functionalized MSN by soaking in the DMSO for 48 hours and dried under vacuum for 24 hours. The opening of mesopores along with the CPT-loaded amine-MSN was covalently capped through amidation of the 3-aminopropyltrimethoxy silane at the pore surface with *meso*-2,3-dimercaptosuccinic acid functionalized superparamagnetic iron oxide nanoparticles (DMSA-Fe_3O_4 NPs) (**Figure 4.2b**), an average diameter of 5.6 nm. The characteristic of the functionalized superparamagnetic iron oxide nanoparticles showed in **Figure 4.3**. The CPT-loaded MSN@Fe_3O_4 nanocarriers showed an average diameter of 100 nm **Figure 4.2c**) and were well-suspended in distilled water for more than 24 h without using any surfactants. The capped Fe_3O_4 nanoparticles formed a dense and uniform layer tightly bound to the MSN surface without any signs of falling from the surface upon vigorously stirring in distilled water via spectroscopic detection, indicating the successful immobilization of the functionalized DMSA-Fe_3O_4 nanoparticles on the MSN surface.

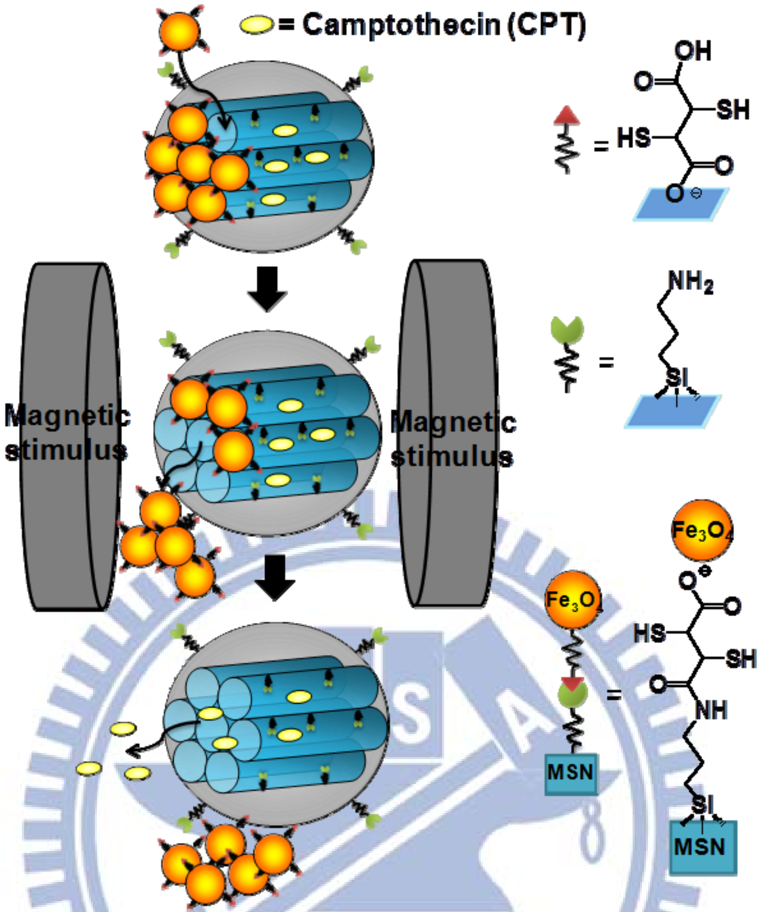

Figure 4.1 Schematic illustration of the synthesis and structure of the Fe_3O_4 NPs-capped mesoporous silica drug nanocarriers. The drug release from MSN@Fe_3O_4 nanocarriers can be remotely controlled under magnetic stimulus.

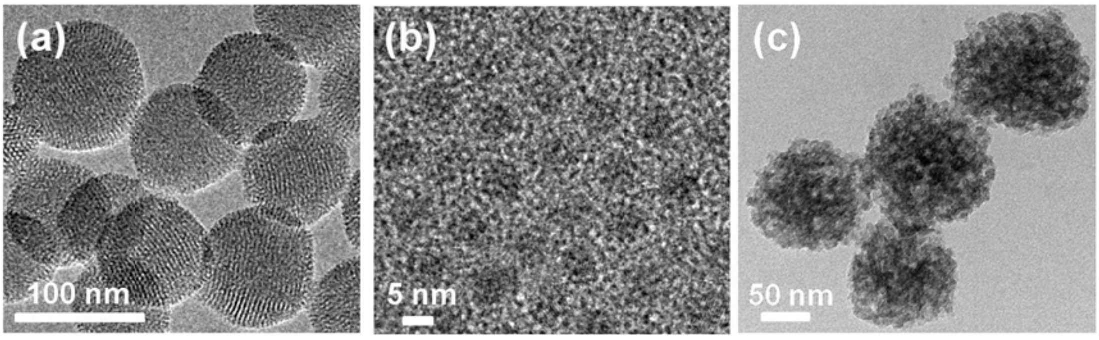

Figure 4.2 TEM images of (a) mesoporous silica nanoparticles, (b) Fe_3O_4 NPs, and (c) Fe_3O_4 NPs -capped mesoporous silica nanocarriers (MSN@Fe_3O_4).

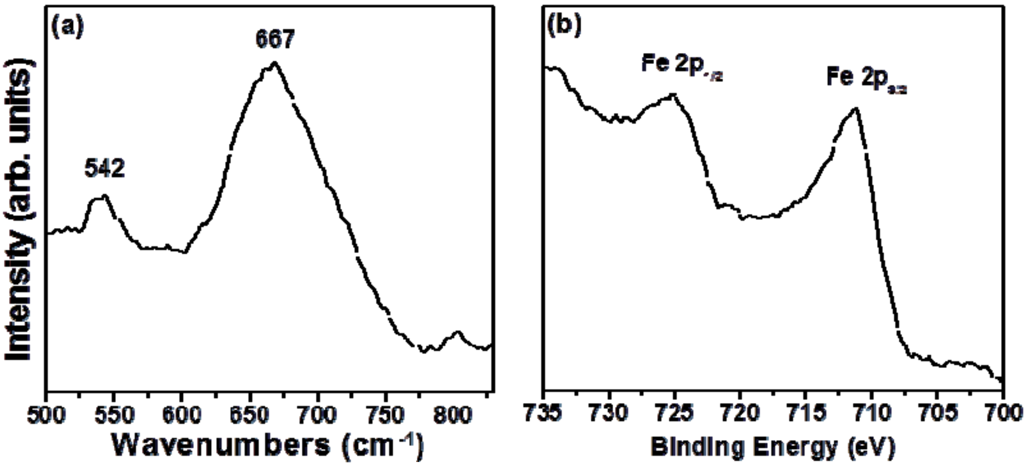

Figure 4.3 (a) The Raman spectroscopy analysis and (b) X-ray Photoelectron Spectrometer of the iron oxide nanoparticles.

4.4 Characterization of MSN@Fe_3O_4 nanocarriers

The covalent immobilization of the Fe_3O_4-capped MSN led to a decrease in X-ray diffraction intensity (**Figure 4.4a**). The low angle X-ray diffraction analysis shows three diffraction peaks at $2\theta = 2.3^o$, 3.9^o, 4.3^o assigned to the characteristic mesoporous structure of standard MCM-41 and indicating an MSN architecture. However, high angle x-ray diffraction patterns of the MSN@Fe_3O_4 matched exactly that of the DMSA-Fe_3O_4 NPs (**Figure 4.4b**), which confirmed the presence of DMSA-Fe_3O_4 NPs on the surface of the MSN matrix. The magnetic property of Fe_3O_4 NPs and MSN@Fe_3O_4 nanocarriers was estimated by SQUID at 298K with the magnetic field sweeping from -10000 to +10000 G. **Figure 4.4c** shows the correlation of the magnetization with the magnetic field for the Fe_3O_4 NPs and MSN@Fe_3O_4 nanocarriers where the curves showed similar shape with negligible hysteresis. The presence of mesoporous silica nanoparticles dilutes the concentration of Fe_3O_4 nanoparticles, resulting in a lower saturation magnetization (*Ms*) of the MSN@Fe_3O_4 nanocarriers than that of the pure Fe_3O_4 NPs. The magnetic properties of MSN@Fe_3O_4 nanocarriers were also tested by applying a magnet near the cuvette, where the MSN@Fe_3O_4 nanocarriers were completely moved to the side of the cuvette nearest to the magnet, as illustrated in **Figure 4.4c**.

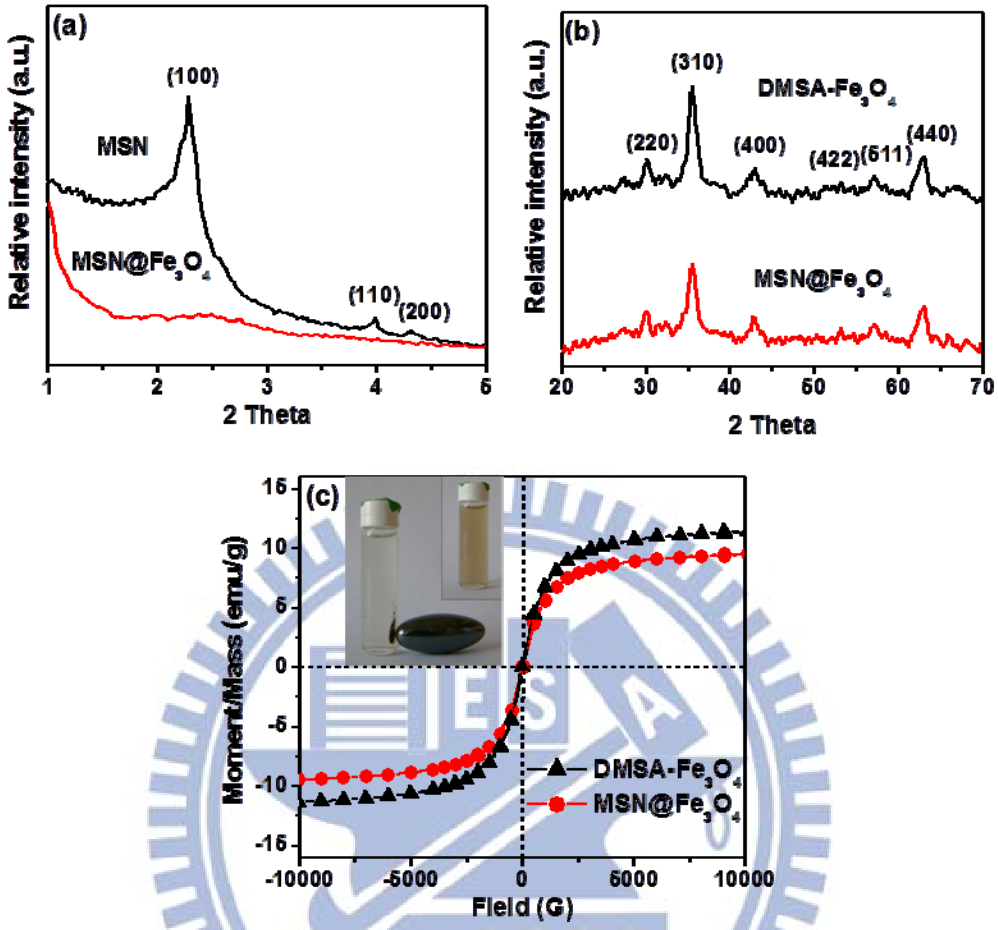

Figure 4.4 (a) Low angle powder x-ray diffraction patterns (XRD) of the MSN material and Fe_3O_4 NPs capped on MSN (b) High angle powder x-ray diffraction patterns of DMSA-Fe_3O_4 NPs and MSN@Fe_3O_4 nanocarriers. (c) Field-dependent magnetization curve of Fe_3O_4 NPs, DMSA-Fe_3O_4 and MSN@Fe_3O_4 nanocarriers. The inset shows that the MSN@Fe_3O_4 nanocarriers are attracted by an external magnet.

The N_2 adsorption/desorption isotherms of MSN and CPT-loaded MSN showed a typical MCM-41 structure (type IV) with Brunauer-Emmett-Teller (BET) analysis as shown in **Figure 4.5** and **Figure 4.6**. The surface area of the MSN is 1150.97 m^2/g, and the pore volume is 0.84 cc/g. A narrow pore size distribution of 2.17 nm (radius) was obtained using the Barrett-Joiner-Halenda (BJH) method. After CPT encapsulation, the surface area, pore volume and pore size of the CPT-loaded MSN were all reduced to a considerable extent compared with the MSN, indicating that the CPT molecules were filled into the pore space of the MSN. In contrast, the as-prepared MSN showed a high surface area 1150.97 m^2/g, and the MSN@Fe_3O_4 demonstrated a type II BET isotherm typical of nonporous materials, with a surface area 128.96 m^2/g. The DMSA-Fe_3O_4 NPs provided nearly full coverage of the MSN surface as confirmed by the N_2 adsorption/desorption isotherms.

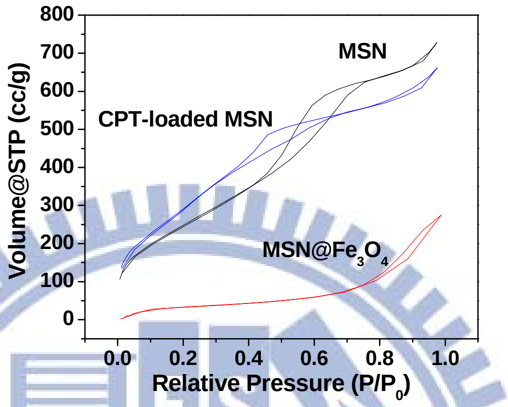

Figure 4.5 N_2 adsorption/desorption isotherms of MSN, CPT-loaded MSN and MSN@Fe_3O_4 nanocarriers.

Sample	Surface area (m^2/g)	Pore volume (cc/g)	Pore radius (nm)
MSN	1150.97	0.84	2.17
CPT-loaded MSN	885.86	0.64	1.57
MSN@Fe_3O_4	128.96	0.37	x

Figure 4.6 The Brunauer-Emmett-Teller (BET) analysis of MSN, CPT-loaded MSN and MSN@Fe_3O_4 nanocarriers.

4.5 Drug release of CPT-loaded MSN@Fe_3O_4 and under magnetic stimulus

Figure 4.7a shows the cumulative drug release of the MSN and MSN@Fe_3O_4 nanocarriers in a PBS buffered at pH 7.4. The release profiles clearly prove that both systems exhibit sustained-release behavior, but the release rates were apparently different. The amount of (S)-(+)-camptothecin (CPT) reached, from the MSN, 95% in 48 hours, and it only took 2.6% from the MSN@Fe_3O_4 nanocarriers. Such a small amount may be attributed as the result of surface residue upon the drug impregnation procedure. This finding demonstrated that most of the drug molecules were well-anchored within the nanoporous network of the MSN without leakage. The difference in release rate is solely attributed to the capped Fe_3O_4 NPs covering the surface of MSN that effectively prevented the CPT from free elution. In contrast, the concentration gradient led to outward diffusion of the CPT from the MSN without Fe_3O_4 capping.

Under magnetic stimulus, the release profile of CPT for the MSN@Fe_3O_4 nanocarriers is shown in **Figure 4.7b**. The cumulative drug release from the MSN@Fe_3O_4 nanocarriers is increased from 0.2% to about 21.9% over a 5-min stimulus. When the stimulus was removed, some of the Fe_3O_4 NPs fell apart from the surface of the MSN, as observed in the TEM image, increasing the surface area exposure, which results in an increased CPT elution. After 24 hours, the cumulative release increased from 21.9% to 45.9%. When a consecutive magnetic stimulus at 1-min and 3-min durations was applied, the release profiles were also observed. Interestingly, the rates of release of CPT showed different profiles before and after the magnetic stimulus. Under the magnetic stimulus, some of the Fe_3O_4 NPs were removed from the surface of the MSN, and the CPT burst from the MSN matrix in ten minutes. However, a slow diffusion-like profile over a timespan of 24 h was detected right after the stimulus was shut down. As expected, increasing stimulus durations caused an increment of CPT elution and a linear profile against the stimulus duration was obtained.

4.6 Operation mechanism of the nanocarriers under magnetic stimulus

Because this magnetic-induced release profile is believed to be a result of the removal of the Fe_3O_4 NPs from the MSN surface, and from **Figure 4.7b**, a time-dependent (magnetic-induced) drug-release profile is suggestive of a time-dependent removal of the Fe_3O_4 NPs. Thus, it is interesting to explore the correlation between the release profile and the amount of Fe_3O_4 NPs magnetically removed. Upon magnetic stimulus, the amount and distribution of Fe_3O_4 NPs on the surface of MSN was carefully monitored, as shown in **Figure 4.8**. As the time of stimulus increased, the quantity of the capped Fe_3O_4 NPs decreased, and, accordingly, more pores of MSN were exposed to the diluting medium, resulting in a greater amount of drug dissolved and diffused outward.

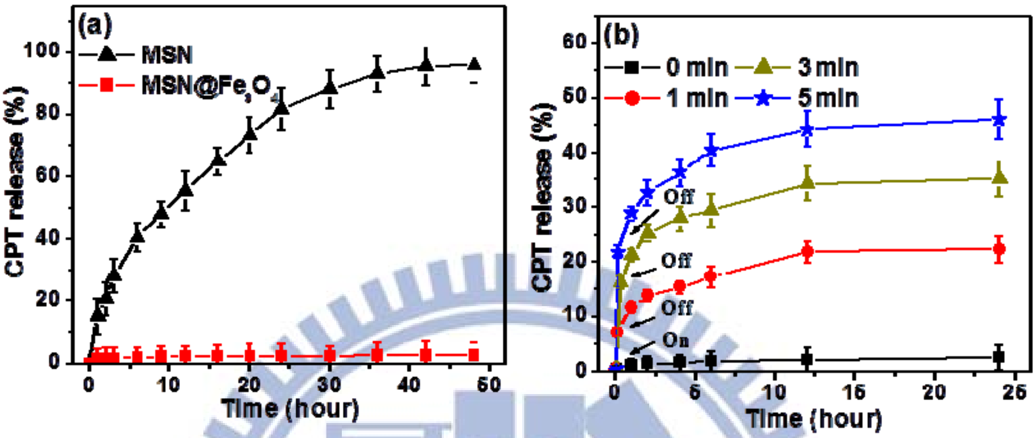

Figure 4.7 (a) Cumulative drug-release of MSN and $MSN@Fe_3O_4$ nanocarriers. The $MSN@Fe_3O_4$ nanocarriers showed no drug leakage compared to MSN nanoparticles. (b) Cumulative drug release profiles of CPT from $MSN@Fe_3O_4$ nanocarriers triggered by magnetic stimulus for 1-5 min.

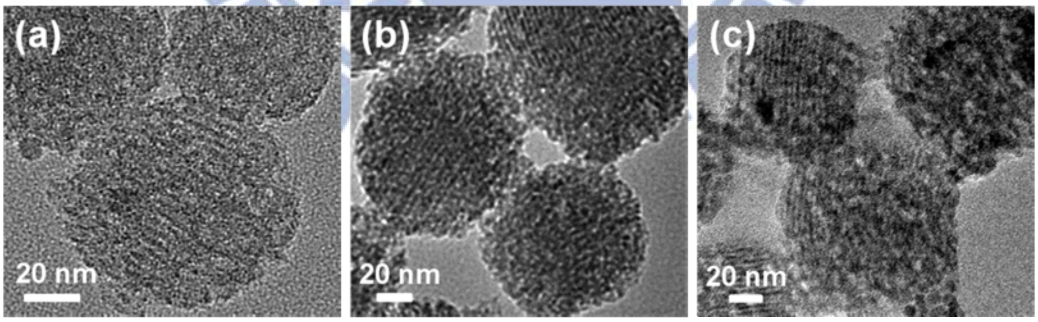

Figure 4.8 TEM images of nanostructures of $MSN@Fe_3O_4$ after magnetic stimulus for (a) 1-min (b) 3-min and (c) 5-min duration.

Because it is hard to obtain an accurate estimate of the exposed surface area of the $MSN@Fe_3O_4$ nanocarriers upon magnetic stimulus, from, for instance, microscopy examination, we employed the weight loss of the $MSN@Fe_3O_4$ as a parameter for the estimation by assuming an average of monolayer coverage of Fe_3O_4 was measured upon a magnetic stimulus indicating that the magnetic nanoparticles were separated apart from the MSN surface. The weight loss (%) of the MSN@Fe_3O_4 nanocarriers is given in **Figure 4.9** using the Eq. (1) below.

$$\textit{Weight loss } \% = \frac{\textit{the weight of } Fe_3O_4 \textit{ NPs on the MSN surface decrease after magnetic stimulus}}{\textit{the weight of } Fe_3O_4 \textit{ NPs on the MSN surface}} \tag{1}$$

After a 1-min exposure under the field, the Fe_3O_4 NPs on the surface of MSN lost 10.86% in weight and became more pronounced as the time of stimulus elapsed. To investigate the relationship between the weight loss of nano-Fe_3O_4 caps and amount of CPT released, two timespans were chosen, i.e., 10 min and 12 hours of CPT release, as shown in **Figure 4.10a**. The former timespan assumes that the releasing profile is approaching steady-state kinetics after a short time period when the nano-caps were removed, while the 12-h timespan suggests a steady-state profile reached after the nano-caps were magnetically lifted off. A linear correlation between the amount of drug released and the weight change of the MSN@Fe_3O_4 nanocarriers was measured for the two timespans. The slope of the straight lines is nearly the same, which suggests (1) the mechanism for the drug

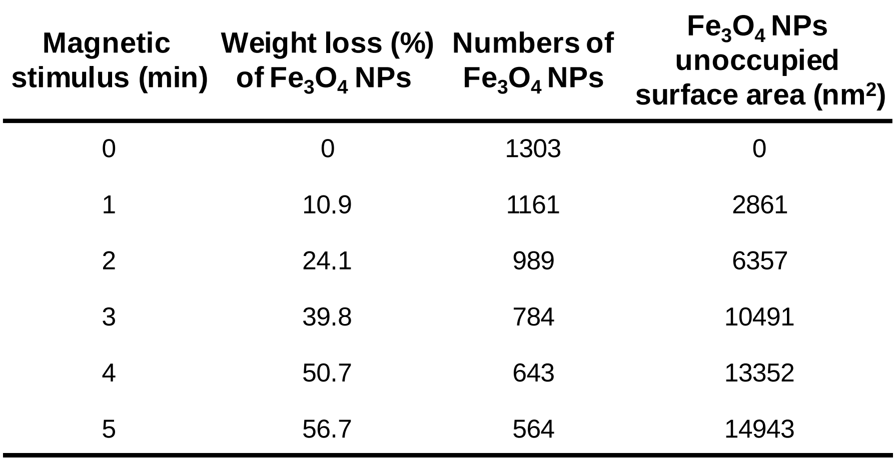

Magnetic stimulus (min)	Weight loss (%) of Fe_3O_4 NPs	Numbers of Fe_3O_4 NPs	Fe_3O_4 NPs unoccupied surface area (nm^2)
0	0	1303	0
1	10.9	1161	2861
2	24.1	989	6357
3	39.8	784	10491
4	50.7	643	13352
5	56.7	564	14943

Figure 4.9 The weight loss (%), numbers and unoccupied surface area of Fe_3O_4 NPs on one MSN@Fe_3O_4 nanocarriers surface under exposure to a magnetic stimulus for 0 to 5 min.

release remained the same across these two timespans, which is considered diffusion kinetics, and (2) the release amount of the drug can be linearly correlated with the weight loss of the MSN@Fe_3O_4 nanocarriers.

Such a magnetic-induced removal of the nano-caps implies a cleavage of the chemical bond between the DMSA-Fe_3O_4 nano-caps and silanized MSN, forming a chemical link as schematically drawn in **Figure 4.10b**. The bond energy of such a chemical link can be a sum or a portion of individual bonds including C – C (83 kcal/mole), C – N (74 kcal/mole), C – Si (83 kcal/mole), O – CO (110 kcal/mole), and C = O (179 kcal/mole). To effectively break the bond, a higher magnetic-induced power is indispensible, and the magnetic power employed is 2.0 kW (=0.48 kcal/sec) in this study. For a period of stimulus from 1, 2, 3, 4 to 5 minutes, an energy of 28.8, 57.6, 86.4, 115.2 and 144 kcal, was produced, respectively. The molar ratio of MSN: Fe_3O_4 NPs = 1 : 2.07, which corresponds to a total of 3.45×10^{-4} mole of Fe_3O_4 nano-caps. The surface area of one Fe_3O_4 NP projected onto the MSN is 49.24 nm^2, and the average radius of one DMSA molecule is 0.36 nm, corresponding to a surface area of 0.41nm^2 covering the Fe_3O_4 NP. Therefore, there are 121 molecules of DMSA on one side of the Fe_3O_4 NP attached to the MSN surface, and it is also suggestive of 121 units of chemical bonds linked between one Fe_3O_4 NP and MSN. As such, a total of 4.17×10^{-2} mole chemical bonds can be estimated between MSN and Fe_3O_4 NPs. The bonding energy of these chemical bonds is multiplied by 4.17×10^{-2}, which gives the total bond energy anchored between the DMSA-Fe_3O_4 nano-caps and functionalized MSN nanoparticles: C – C: $83 \times 4.17 \times 10^{-2} = 3.46$ kcal, C – N: 3.09 kcal, C – Si: 3.46 kcal, O – CO: 4.59 kcal and C = O: 7.46 kcal. Accordingly, the energy induced from the magnetic stimulus over various timespans is sufficiently large to cleave the chemical bond, resulting in an effective removal of the nano-caps (**Figure 4.8**). The rate of nano-cap removal can then be a function of the magnetic energy.

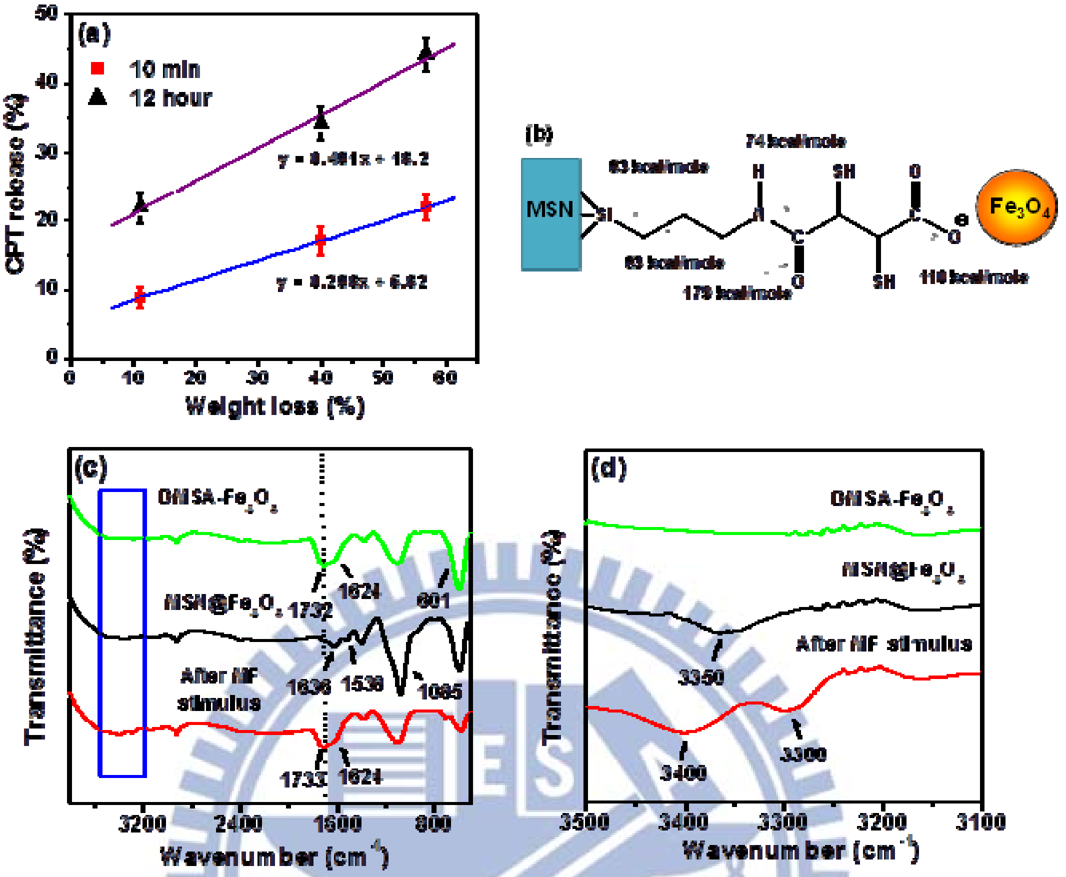

Figure 4.10 (a) The relationship between the weight loss of Fe_3O_4 NPs and the released amount of CPT for 10-min and 12-hours releasing duration. (b) Schematic illustration of the chemical bonding between Fe_3O_4 NPs and MSN. (c) and (d) The FT-IR spectrum of DMSA-Fe_3O_4 NPs,MSN@Fe_3O_4 and MSN@Fe_3O_4 after 3min of magnetic stimulus.

The DMSA-Fe_3O_4 NPs, MSN@Fe_3O_4 and MSN@Fe_3O_4 with 3-min magnetic stimulus were verified using infrared spectroscopic analysis, as shown in **Figure 4.10c**. For the DMSA-Fe_3O_4 NPs, the typical Fe-O stretch is at 601 cm^{-1}, and the peak at 2374 cm^{-1} is assigned to S-H stretching. In addition, there are two C = O stretches; the one at 1624 cm^{-1} is referred to the stretching mode of carboxylate due to the interaction for the carboxylate anion with the Fe_3O_4 surface. The other, the C = O stretching of carboxylic acid, appears at 1732 cm^{-1}. For the MSN@Fe_3O_4, Si-OH (1085 cm^{-1}) in the IR spectrum was identified due to MSN. The C = O stretching mode from carboxylic acid was also detected, but its intensity was reduced because of amide bond formation. The finding indicates that both the N - H (1538 cm^{-1}) and C = O (1636 cm^{-1}) bonds were present because of the chemical reaction between the carboxylic acid group of DMSA-Fe_3O_4 and the amino group of MSN to form the amide linkage. After the 3-min magnetic stimulus, the N-H stretch mode was reduced in intensity, and the C = O stretch band shifted from 1636 to 1733 cm^{-1}, indicating that the amide bond was cleaved to form carboxylic acid. An enlarged version in the IR spectra between 3100 cm^{-1} and 3500 cm^{-1}, shown below (**Figure 4.10d**), clearly indicates that N - H (3350 cm^{-1}) bond was present because the secondary amines of amide bond were formed. However, after the 3-min magnetic stimulus, the N-H stretch mode changed from singlet peak to doublet peak (3300 cm^{-1} and 3400 cm^{-1}), indicating that the secondary amines of amide bond were cleaved to form the primary amine. This observation does provide evidence for bond cleavage of the amide linkage. From the bond strength information, the amide bond is the weakest among others. Combining the bond strength and IR analysis, it is reasonable to believe that the amide bond was broken under magnetic stimulus and takes major responsibility for the removal of the Fe_3O_4 NPs from the MSN surface.

Further estimation on the exposed surface area of the MSN upon magnetic stimulus was approached using the Eq. (2) described below.

$$w = P \cdot 4\pi R^2 \cdot \rho \cdot h = \frac{4}{3}\pi r^3 \cdot \rho \cdot N \qquad (2)$$

where w is the total weight of Fe_3O_4 NPs for an MSN@Fe_3O_4 nanocarrier, P is a random probability of 64% (for a randomly packing configuration of the nano-caps on a given MSN surface area), R is the radius of MSN, ρ is the density of Fe_3O_4 NPs 5.17g/cm^3, h is the thickness of Fe_3O_4, r is the radius of Fe_3O_4 NPs, and N is the numbers of Fe_3O_4 NPs on the surface of a MSN nanoparticles. From TEM analysis it was clear that R is 45.8 nm, h is 7.1 nm, and r is 2.8 nm, which suggests an average of 1.2 nano-caps deposited on the surface, which is reasonably close to an earlier assumption of monolayer coverage. On this basis, the exposed surface area should be correlated in a quantitative manner with the weight change of the nanocarriers after being subjected to the magnetic stimulus of various timespans. **Figure 4.10** gives resulting calculations and, as expected, a linear relationship; **Figure 4.11** can be well-estimated between the weight change (and drug release) of the MSN@Fe_3O_4 nanocarriers and corresponding surface area being exposed as a result of nano-cap removal. This finding strongly implies the technical potential for advanced use of such capped functionalized nanocarriers for various industrial sectors where a programmable chemical or biochemical reaction, patient-specific therapy, or controlled catalysis can be magnetically tunable. However, as the main research theme of this work, a drug delivery nanosystem is tested, and the cellular uptake and cytocompatibility are prime concerns to be clarified.

4.7 Cell uptake and cell viability under magnetic stimulus

Cellular uptake of the FITC-loaded MSN@Fe_3O_4 nanocarriers was monitored by confocal laser scanning microscopy. **Figure 4.12a, 4.12b, 4.12c** shows that the nanocarriers (as arrows labeled) were gradually taken after incubating with the A549 cell for 1-h and 4-h durations. The green fluorescent dye can be clearly observed to be randomly distributed in the region of cytoplasm over the short time periods of incubation. For 1-h incubation, some of the nanocarriers appeared to attach rapidly to the surface of the cell membranes. However, numerous regions of the cytoplasm displayed strong green fluorescent illumination at 4 hours. This observation implies that the nanocarriers can be internalized rapidly upon cellular uptake.

The result of the MTT (3-(4,5-dimethyldiazol-2-yl)-2,5 diphenyl tetrazolium bromide) assay as a measure of metabolic competence of the cell with the MSN@Fe_3O_4 nanocarriers is shown in **Fig. 4.12d**. The nanocarriers were incubated with A549 cancer cells for 24 hours, and part of them were subjected to the magnetic stimulus for 3 minutes. The result showed that a higher cytotoxicity of about 26.5% was obtained from the CPT-loaded MSN compared to CPT-loaded MSN@Fe_3O_4. The result indicated that nano-Fe_3O_4-capped MSN effectively constraint the CPT from free elution, resulting in a well-tolerated cell viability more than 80% and a free diffusion of the CPT from the CPT-loaded MSN effectively killing the cells. Upon magnetic stimulus, about 42% of cells were killed, and the CPT released from the MSN@Fe_3O_4 is the major cause of cell death. In a control group, the drug-free MSN@Fe_3O_4 nanocarriers demonstrated excellent cell viability under the same magnetic treatment, which further substantiates the effectiveness of the CPT-loaded MSN@Fe_3O_4 nanocarriers as a versatile magnetically controlled drug delivery nanosystem.

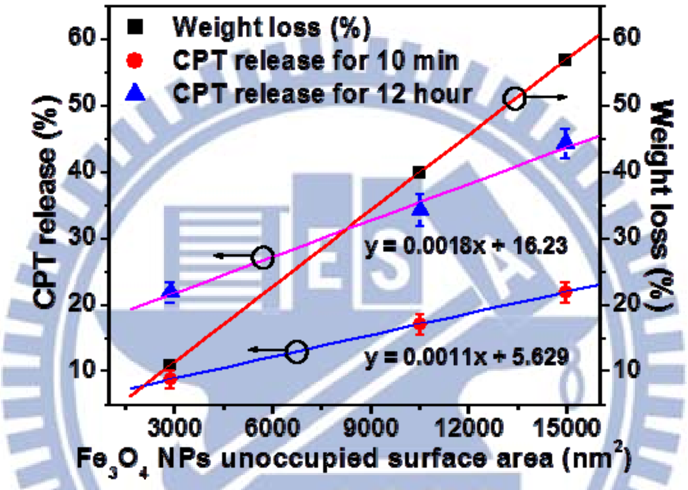

Figure 4.11 Showing a linear relationship between the weight loss of Fe_3O_4 NPs and the Fe_3O_4 NP unoccupied surface area of MSN. A similar relationship exists in between the released amount of CPT and the Fe_3O_4 NPs unoccupied surface area of MSN for 10 min and 12 hours of release duration.

4.8 Magnetic resonance behavior of MSN@Fe_3O_4 nanocarriers

The superparamagnetic characteristics of the Fe_3O_4 nanoparticles accelerate the transverse relation of water protons, and the Fe_3O_4-capped MSN could be used as a T_2 contrast agent in MR images. The longitudinal (T_1) and transverse (T_2) relaxation times of protons from the dispersion containing MSN@Fe_3O_4 are shown in **Figure 4.13a**. As shown, the MR signal decreased with the increasing content of MSN@Fe_3O_4, demonstrating the efficiency of the

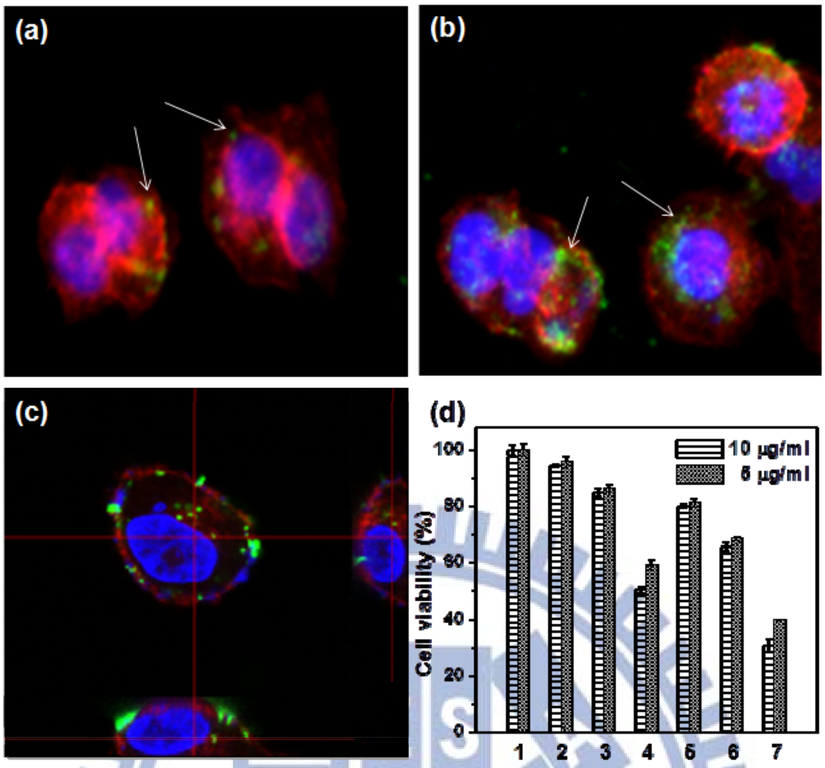

Figure 4.12 Time-course PL microscopy images of A549 cells labeled with FITC-MSN@Fe_3O_4 nanocarriers and incubated for (a) 1 hour and (b) 4 hours. (c) Illustration of the cell section after incubating for 4 hours. The cell skeleton was stained with rodamin phalloidin (red), and the cell nucleus with DAPI (blue). (d) Cell viability of A549 cells after 24 h of incubation with (1) control group, (2) MSN, (3) MSN@Fe_3O_4, (4) CPT-loaded MSN, (5) CPT-loaded MSN@Fe_3O_4, (6) MSN@Fe_3O_4 for 3 min of magnetic stimulus, and (7) CPT-loaded MSN@Fe_3O_4 for 3 min of magnetic stimulus. Cell viability was measured using an MTT assay.

MSN@Fe_3O_4 in enhancing the transverse (T_2) proton relaxation process. The efficacy and stability of the MSN@Fe_3O_4 as an MR contrast agent was further evaluated by measuring the longitudinal (r_1) and transverse (r_2) relaxivities using an MR scanner. **Figure 4.13b** shows that the r_1 of the MSN@Fe_3O_4 was 1.45 $s^{-1}mM^{-1}Fe$, and the r_2 value was 121.57 $s^{-1}mM^{-1}Fe$, which is larger than that reported for mesoporous silica nanoparticles decorated with magnetite nanocrystals (76.2 $s^{-1}mM^{-1}Fe$) .[119] The higher transverse (r_2) relaxivities could be attributed to the MSN@Fe_3O_4 nanocarriers with the capped Fe_3O_4 nanoparticles forming a dense and uniform layer tightly bounded to the MSN surface. Therefore, MSN@Fe_3O_4

nanocarriers could perform well as a T_2- type MR contrast enhancement agent for cell or molecular imaging and diagnostic applications.

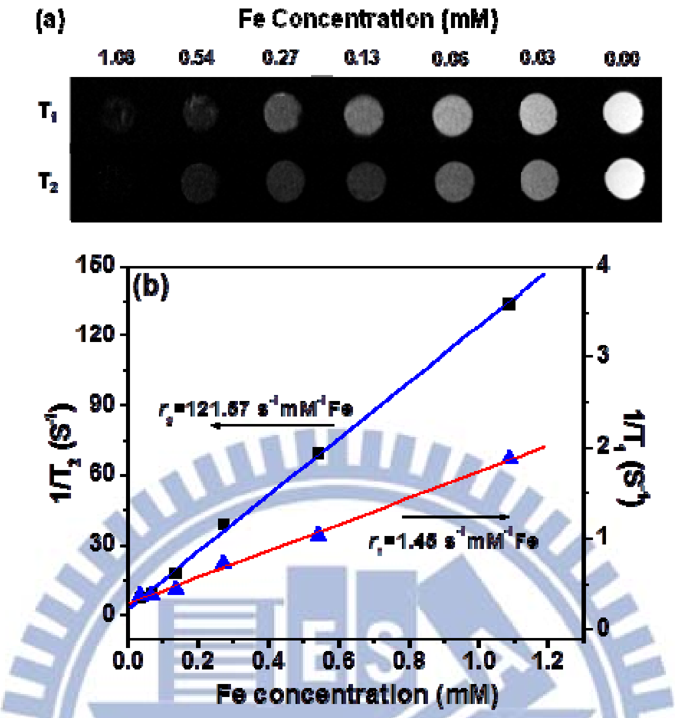

Figure 4.13 (a) T_1-weighted and T_2-weighted MR images (fast spin-echo sequence: repetition time (TR) = 2500 ms, echo time (TE) = 33 ms) of the aqueous dispersion of MSN@Fe_3O_4 at different Fe concentrations. (b) T_1 and T_2 relaxation rates ($1/T_1$, $1/T_2$) as a function of iron molar concentration obtained using a 7.0 T MR scanner.

4.9 Summary

Fe_3O_4-capped mesoporous silica nanoparticles (MSN@Fe_3O_4) were successfully developed in this work and displayed a well-dispersed character in an aqueous solution. The enormous nanoporous network of the MSN permitted a sufficient amount of drug to be carried for a subsequent delivery purpose. As expected, once a model drug, CPT, was enclosed, following the deposition of nano-Fe_3O_4 particles to reach a full coverage on the MSN surface, no leakage of the drug from the MSN@Fe_3O_4 was observed. Under a magnetic stimulus, the drug eluted in a fast-acting, burst-like profile depending on the time duration of the stimulus. The release profile underlying the stimulus was confirmed to be a result of the removal of the capped Fe_3O_4 nanoparticles from the MSN surface due to the cleavage of the chemical bonds bridging both Fe_3O_4 and MSN. The longer the stimulus duration, the larger the amount of nano-Fe_3O_4 caps removed and the larger the bare surface of MSN exposed, resulting in a larger burst. In addition, the MSN@Fe_3O_4 nanocarriers showed great potential as probes in MRI and an efficient uptake by A549 cells and also demonstrated an excellent cytocompatibility. Together with a well-regulated controlled release design, the nanocarriers are expected to offer great advantages as an effective multifunctional drug delivery and imaging for cell-based therapeutic purposes.

Chapter 5

Geometrical Confinement of Quantum Dots in Porous Nanobeads with Ultra-efficient Fluorescence for Cell-specific Targeting and Bioimaging

5.1 Introduction

Design and fabrication of nanoobjects with sophisticated nanoscopic structures are technically important in advanced applications in areas including renewable energy,[120,121] biomedicine,[122,123] therapeutics,[124,125] complex materials and catalysis.[126-128] Composite structures integrating multi-functionalities in a given nanometric volume with elaborate advantages of such as optical and electronic properties over their single constituent have been widely-studied topics for recent decades.[129,130] One important strategy for construction of composite nanostructure is to introduce molecular, oligomeric or macromolecular precursors with self-assembled capability into the nanostructures.[131,132] However, most chemical modifications are complex, time-consuming and even in a risk of losing original function of the starting nanomatrix. For example, optical probes such as quantum dots coated by silica, copolymer or lipids demonstrated a great damage of quantum yield approximately 30-50% lower than their original brightnes, limiting their applications.[133,134] Furthermore, for biological applications, the optical probes should be stabilized between pH 4 and 8, a physiological range that has frequently found in human body. Therefore, the development of multifunctional nanoprobes enabling new imaging modalities beyond the intrinsic limitations of individual components is essential and considerable attention has been received in a number of areas, ranging from fundamental biology to molecular imaging and medical diagnostics.

Recently, Gao et, al.[135,136] have reported mesoporous silica and polystyrene microbeads encoded with quantum dots maintain high fluorescence intensity and uniformity. The pore sizes are typically engineered to 30-100 nm for fast QD doping and uniform QD distribution inside the microbeads. A key factor contributing to the improved brightness is the multi-stage doping QDs and the inner pore chemical structures, which stabilizes QDs via physical adsorption and leads to nearly no sacrificing the optical properties. On the other hand, Tasciotti et al. and Ananta et Al. [137,138] also reported the porous micro-sized silica particles successfully doped with functional nanoparticles such as QDs, carbon nanotubes, Gd-based materials, or therapeutic agents through multi-stage modification, leading to a functionalized nanocarrier for imaging and biomedical uses. Despite these recent achievements, a number of issues have addressed limited applications of this type of functionalized nanocarrier in biomedical research before its clinical translations. To a significant extend, size mismatch is one of major reasons between current doped porous nanoobjects and the biological systems. On the length scale of micrometers, synthetic approaches based on silicon etching or chemical synthesis for making uniform nano-sized porous structures of tunable composition are well-established. However, a key problem is that the sizes of these mesoporous particles range of 1-10 μm, which are too big for applications such as molecular imaging, drug delivery, and biomolecule labeling. In addition, recent reports on mesoporous silica have demonstrated their feasibility for use in a variety of biological applications.[139,140] However, using mesoporous silica matrix with pore size about 2~3 nm to load guest molecules by chemical bridge, it will limit tagged large molecule weight molecules or particles and damage the property through chemical bridge. Furthermore, the porous silica materials are less hydrophobic over both external and internal regions of the pores because of their highly hydrophilic groups i.e., Si-O, Si-OH, distributed over the regions, which adversely affects the loading efficiency of many water insoluble active molecules of technically or therapeutically interest.

To overcome these problems, we employ QDs as the guest “molecule” internalized with nano-sized mesoporous silica nanoparticles, wherein a multifunctional nanoobject capable of imaging and targeting was constructed. This multifunctional nanocarrier was prepared via a facile, step-wise procedure, including (1) preparing a highly hydrophobic octadecyltrimethoxysilane-modified mesoporous silica nanoparticle (hydrophobic porous nanobeads) with pore size greater than 10 nm, (2) internalizing hydrophobic QDs, and (3) bridging the peptide cRGD on the surface of QD-tagged nanobeads by using noncovalent biotin-streptavidin link rendering a potential cellular-based targeting achievable. This multifunctional nanocarrier, designed in this work, to our knowledge, provides exceptionally highly chemical and pH stability and in the meantime, offers a wide spectrum of multiplex color codings for targeting and imaging modality.

5.2 Experimental section

Synthesis of hydrophobic porous nanobeads (NBs): 300 mg cetyltrimethylammonium bromide (CTAB) was dissolved in a mixture of 45 ml octane and 96 ml dilute water at 70^{o}C. After stirred magnetically for 20 min, 8.5ml styrene monomer, 66 mg lysine, 3000 mg tetraethylorthosilicate (TEOS), and 115 mg AIBA were subsequently added to the system and stirred magnetically for 4 h. After 4 h, the heating was stopped and the suspension was cooled naturally to room temperature. The products were collected by centrifugation at 6000 rpm for 10 min and then washed 3 times with an excess of pure methanol. Finally the template was completely removed by heat treatment at 600^{o}C under atmospheric conditions. The products, 500 mg mesoporous beads, were redispersed into a mixture of 3 ml octadecyltrimethoxysilane and 10 ml toluene. After stirred magnetically for 96 h at room temperature, the products were collected by centrifugation at 6000 rpm for 10 min and then were redispersed into *n*-butanol.

Hydrophobic porous nanobeads incorporation of quantum dots and lipid-PEG$_{2000}$-COOH coating (LQNBs): Incorporation of QDs was achieved by swelling the nanoporous beads in a solvent mixture containing 5% (vol/vol) chloroform and 95% (vol/vol) *n*-butanol, and then by adding a controlled amount of ZnS-capped CdSe QDs to the mixture. After stirred magnetically for 2 h, the products were collected by centrifugation at 8000 rpm for 10 min and then were redispersed into *n*-butanol (1 ml). Lipid-PEG_{2000}-COOH (3 mg) was added to the solution and sonicated for 3 min. Excess lipid were purified out from the solubilized beads with incorporation of QDs using repeated centrifugation at 8000 rpm for 10 min. The purified nanoparticles were redispersed in DI water.

Bioconjugate formation and cRGD-encoded: The LQNBs were activated by sonicating with 2 ml of 0.5% EDC containing *N*-hydroxysuccinimide (NHS) (0.2 wt%) aqueous solution. After stirred magnetically for 30 min, the nanoparticles were calibrated with sodium acetate buffer (pH 4.5). Streptavidin-NH_2 (0.1 mg/mL) in the same buffer solution was then applied for immobilization. At saturation, the nanocapsules were washed by distilled water. The cRGD-PEG_2-biotin was used to form a noncovalent biotin-streptavidin bridge for direct sensing of recombinant prion protein, the streptavidin surface of nanobeads was directly exposed to cRGD-PEG_2-biotin (0.05 mg/mL) in PBS buffer for incubation.

Quantum yield measurement: Photoluminescence quantum yields (QY) of the samples were determined from the following equation (3):

$$Quantum\ yield\ (QY)\% = Qst(Ast/As)(Ds/Dst) \qquad (3)$$

Here, Qst is the quantum yield of the standard substance, Rhodamine B, known to be 0.31 in H_2O; Ast and As are the absorbance values of the Rhodamine B solution and samples, respectively, at a wavelength of 514 nm; and Ds and Dst are the corresponding integrated wavenumber values for the sample and Rhodamine B, respectively, in the PL spectra.

Porous nanobeads embedded multicolor quantum dots: Three quantum dots (having green, yellow and red emissions) were mixed by different ratio. Furthermore, incorporation of QDs was achieved by swelling the nanoporous beads in a solvent mixture containing 5% (vol/vol) chloroform and 95% (vol/vol) *n*-butanol, and then by adding a controlled amount of different mixed ratio QDs to the mixture. After stirred magnetically for 2 h, the products were collected by centrifugation at 8000 rpm for 10 min

5.3 Preparation and of cRGD-conjugated quantum dots in porous silica nanobeads

Figure 5.1a illustrates the synthesis of quantum dots (QDs) tagged porous nanobeads through biotin-streptavidin bridged cRGD peptide. The first step is to synthesize the porous silica nanobeads with functionalized octadecyltrimethoxysilane (C_{18} hydrocarbon chain). The morphology and particle size of the porous nanobeads were analyzed with scanning and transmission electron microscopy as shown in **Figure 5.1b and 5.1c,** respectively. A highly porous particle with an average size of 120 nm in diameter was observed. The N_2 adsorption/desorption isotherms of the nanobeads showed relatively large surface area of 819.15 m^2g^{-1} with Brunauer-Emmett-Teller (BET) analysis and a pore size of 5.28 nm (radius) in average was obtained using the Barret-Joiner-Halenda (BJH) method (**Figure 5.2)**. The QDs were chemically anchored via hydrophobic interactions between the C_{18} hydrocarbon chain and tiroctylphosphine oxide (TOPO) molecules, and tagged occurs when the hydrocarbon and surfactant molecules (both are flexible molecules) were intermolecularly inserted to form a stable, interdigitated configuration. **Figure 5.1d and 5.1e** indicate the nanobeads decorated with QDs (black dots) show lattice patterns in the high resolution TEM images. The incorporation of quantum dots (QNBs) was further evidenced using the elemental mapping and energy-dispersive X-ray spectroscopy by TEM (**Figure 5.3)**. The C_{18} hydrocarbon chain modified not only the surface but also the inner porosity of the nanobeads, wherein the QDs efficiently localized and stabilized within the porous nanobeads via chemical anchorage. In contrast, in the absence of the chemical modification, the QDs aggregated outside of the porous nanobeads and the solution also showed fluorescence color (**Figure 5.4a and 5.4c**), indicating the QDs remained staying in the solution, rather than localized inside the nanobeads. Furthermore, the QNBs were coated with functionalized lipid-PEG_{2000}-COOH to give carboxylic acid along the nanobead surface and consequently

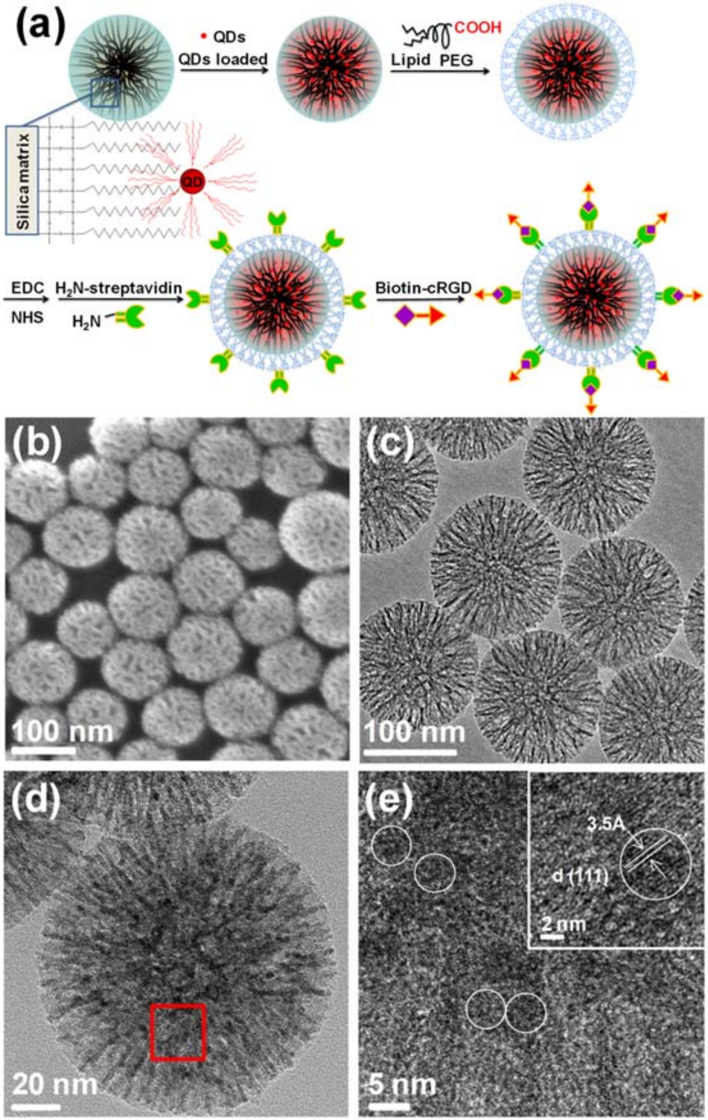

Figure 5.1 (a) Schematic illustration of the synthesis and structure of the cRGD-encoded lipid coated quantum dots tagged porous nanobeads (cRGD-encoded LQNBs). (b) SEM image and (c) TEM image of porous nanobeads. (d) TEM image and (e) High resolution TEM image of QDs tagged porous nanobeads. The circles indicated the QDs.

changed the surface from hydrophobic to hydrophilic. Furthermore, the formation of amide bonds between the carboxylic acids and amines was catalyzed by 1-ethyl-3-(3-dimethy-laminopropyl) carbodiimide which activated the carboxyl groups on the linkers to form O-*urea* derivatives. The addition of *N*-hydroxysuccinimide catalyzed the formation of the intermediate active esters that further reacted with the amine of the streptavidin to give the amide bond between the streptavidin and the carboxyl group along the surface of nanobeads.

Finally, the cRGD-PEG$_2$-biotin was used to form a noncovalent biotin-streptavidin bridge on the surface of the lipid-PEG$_{2000}$-COOH coated QNBs (LQNBs). The QDs incorporated within the pores in a rapid manner by strong hydrophobic interactions and left negligibly small amount of QDs (less than 0.1%) in free solution after 2 hours of impregnation.

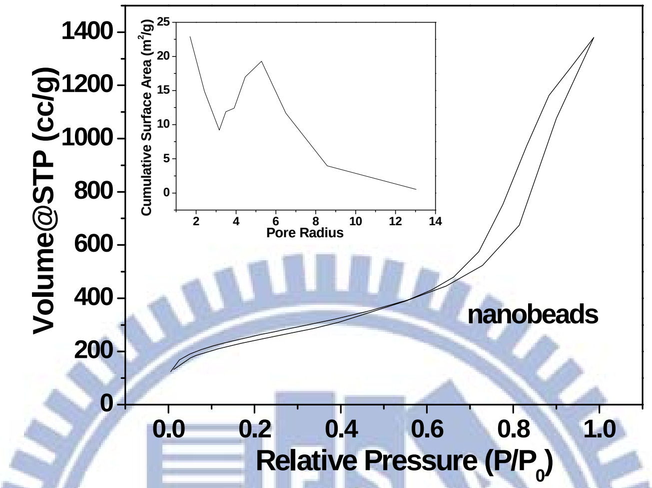

Figure 5.2 The N$_2$ adsorption/desorption isotherms of the nanobeads with Brunauer-Emmett-Teller (BET) and Barret-Joiner-Halenda (BJH) analysis.

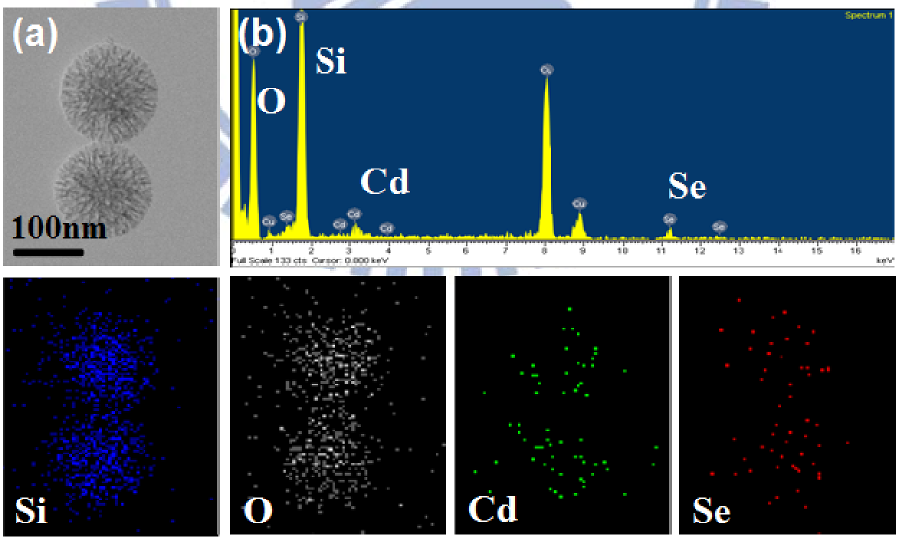

Figure 5.3 The elemental mapping and energy-dispersive X-ray spectroscopy of the incorporation of quantum dots (QNBs) by TEM.

5.4 Characterization of QNBs nanoprobes

Figure 5.5 shows the loading efficiency of QDs in the nanobeads in terms of emission character of QDs. The loading efficiency (LE %) of QNBs is determined using equation (4) :

$$\text{LE \%} = A/B \tag{4}$$

where A is the fluorescence intensity of QNBs at a specific time, and B is the fluorescence intensity of saturated QNBs loading. In the work, the fluorescence intensity of QNBs unchanged after 2-h impregnation, indicating a complete uptake of the QDs into the nanobeads. **Figure 5.5a** showed similar loading efficiency profiles but diverse loading amount. In the early-phase uptake, the QNBs emitted at 530 nm showed higher loading efficiency than others because of smaller size, which is easier accessible to the porous structure of the nanobeads. As well recognized, the different-sized QDs show different emission spectrum, for example, QDs emitted at 530 nm, 560 nm and 600 nm with particle size ranging from approximately 3 nm, 4 nm and 5 nm, respectively. Thus, the 530-nm emitting QDs were much smaller in size than the 600-nm emitting QDs, which translated a faster loading rate for the 530-nm emitting QDs than the others at early-phase uptake.

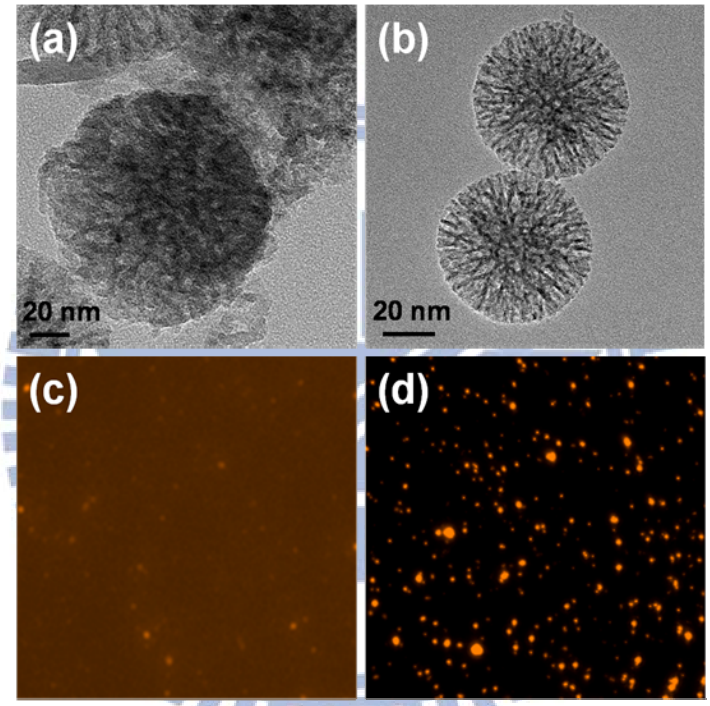

Figure 5.4 (a) TEM and (c) fluorescence images of QDs tagged porous nanobeads without surface modification and (b), (d) showed corresponding images of QDs tagged porous nanobeads which are surface modification of C_{18} hydrocarbon chain.

However, after one hour of QD uptake, emission intensity of the three encapsulated QDs approached an equilibrium status and appeared to reach a maximum emission after two-hour uptake with no further increase in loading efficiency. This finding also proved an efficient loading of the QDs via hydrophobic interactions between hydrocarbon and TOPO molecules.

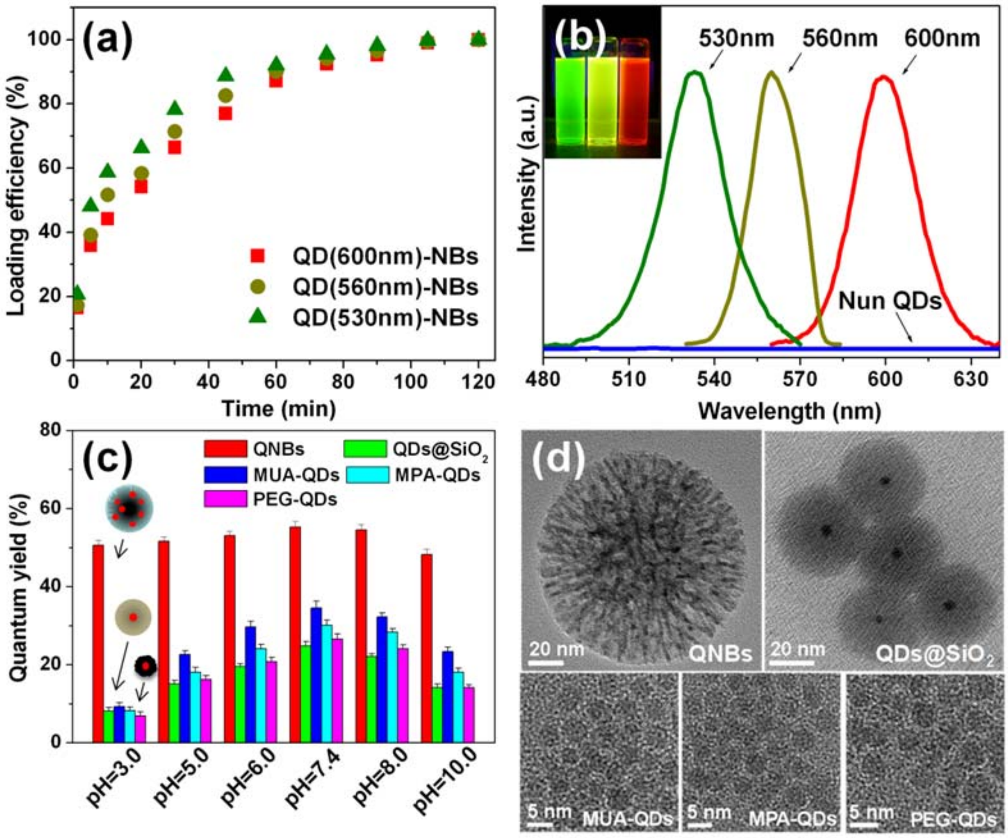

Figure 5.5 (a) The loading efficiency profiles of QDs tagged the nanobeads within the soaking aqueous stock solution time by different emission of QDs. (b) The fluorescence spectrum, showing three separated peaks (530, 560, and 600 nm) with nearly equal intensities. The inset shows three distinguishable emission colors of QNBs excited with a near-UV lamp. (c) The quantum yield comparison of QNBs, with traditional surface coatings, QDs@SiO_2, MUA-QDs, MPA-QDs and PEG-QDs dispersed in PH 3.0, 5.0, 6.0, 7.4, 8.0 and 10.0. (d) TEM images of QNBs, QDs@SiO_2, MUA-QDs, MPA-QDs and PEG-QDs.

Once being loaded, the leakage of the QDs was determined by exposing to various diluting media included water, ethanol and butanol for 24 h. The inset of **Figure 5.6** showed well suspension of the QNBs in these solvents after 24 hours and then centrifuged to separate the QNBs from those diluting media. The resulting supernatants showed colorless under UV exposure, whilst the collected QNBs showing red-orange appearance. From the photoluminescence spectrum, no detectable fluorescence intensity of the supernatants from those solutions was observed, indicating the QDs were readily chemically stabilized within the nanobeads (**Figure 5.6**). The distribution of the QDs in the nanobeads was also examined, since aggregation of QDs causes problems such as spectral broadening, self-quenching, and wavelength shifting of the resulting design. **Figure 5.5b** shows the emission spectra, i.e., orange-red-, yellow- and green-emitting QNBs, where the optical images of QNBs with three different emission appearances were clearly displayed. Besides, the quantum yield of the GNBs was determined experimentally, in comparison, we also prepared a number of quantum dots of the same kind followed by surface modification with various materials according to literature reports.[141] As given in **Figure 5.5c and 5.5d**, the QNBs illustrated the highest quantum yield (~55.2%) than other QDs coated with various materials, e.g., the quantum yield for QDs@SiO_2, QDs functionalized 11-mercaptoundecanoic acid (MUA-QDs), QDs functionalized 3-mercaptopropionic acid (MPA-QDs) and QDs functionalized polyethylene glycol (PEG-QDs) is determined to be 24.8%, 34.5%, 30.1% and 26.6%, respectively. One of the plausible reasons is the QDs localized within the nanobeads being least in surface coverage with C_{18} ligands (through chemical linkages). In other words, the QDs exposed largest surface area to the environment while preparing into a nanostructure presently designed in this work compared to other nanostructural morphologies, where thick surface capping materials suppressed considerably the quantum efficiency. Concerning the effect of pH, the quantum yield of the surface-modified QDs included QDs@SiO_2, MUA-QDs, MPA-QDs and PEG-QDs, showed significant quenching effect at low pH, whilst the QNBs remained relatively high quantum yield, more than 48% at low pH , and high pH as well (pH 3 and 10). However, a slight decay in quantum yield of the QNBs was observed at pH 10 which is due to chemical instability of silica matrix in basic conditions. Therefore, the QDs stabilized inside the mesoporous silica matrix prepared under current study achieved not only the excellent chemical stability but also reached exceptionally high quantum efficiency among other alternative nanostructures. This finding indeed allows the QNBs potentially applicable for quantitative cellular and molecular imaging.

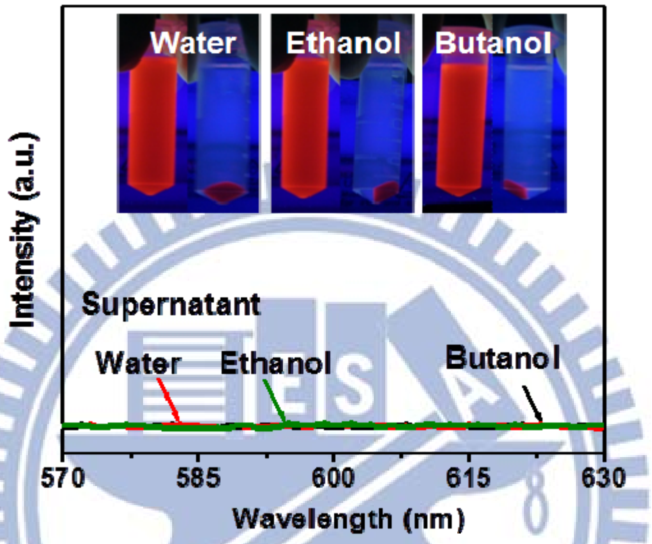

Figure 5.6 The fluorescence data shows the supernatant of LQNBs dissolved in dilute water, ethanol and butanol, which is in the absence of QDs in the solution.

5.5 Optical coding of quantum dots in silica nanobeads

Concerning the wide versatility of the QNBs with various combinations of the QDs of different sizes tagged with the nanobeads, **Figure 5.7a** shows quantitative results obtained from three quantum dots (having green, yellow and red emissions) tagged into the nanobeads. The use of m intensity levels (0, 1, 2, … m) at n different wavelength of the quantum dots gives ($m^n - 1$) color codes. However, the actual coding capabilities are likely to be substantially lower because of spectral overlapping and signal noise. Thus, using 3-5 colors with five intensity levels (designating as 0, 1, 2, 3, 4), yielding approximately 100 to 3000 recognizable color codes is realistic. Following a number of QD combinations tagged with the nanobeads, **Figure 5.7b** shows 7 clear and distinguishable fluorescence emission colors observed from resulting QNBs excited with a UV lamp and separated peaks in fluorescence spectrum. This simple combination opens a wide variety of imaging potential for biomedical uses.

The true-color fluorescence images of nanobeads tagged with QDs emitting at 530 (green), 560 (yellow) and 600 nm (orange-red) are shown in **Figure 5.7c**. These QNBs were considered monochromatic because they were prepared using single-color QDs, and were mixed and spread on a glass surface for fluorescence imaging. Although only a single light source (UV lamp) was used for excitation, all the LQNBs were distinctly and clearly observed. To further testify the imaging capability of the nanobeads, an *in vivo* test was carried out using two types of LQNBs, each doped with green and red QDs, respectively, followed by injecting into nude mouse at two different locations for in-vivo imaging detection, via a non-invasion in vivo imaging system (IVIS). As given in **Figure 5.7d**, the nude mouse at left side, i.e., control group shows no any detectable imaging contrast, whilst for the right-side group, a sharp contrast of the green and red imaging (circle) was distinctly detected.

5.6 Cell uptake and flow cytometry for targeting effect

The cell uptake and intracellular distribution of cRGD-encoded LQNBs with 530 nm QDs were evaluated by confocal laser scanning microscopy (CLSM). Endocytosis-mediated intracellular trafficking of ligands via the $\alpha_v\beta_3$ receptor of MCF-7 cells and the $\alpha_v\beta_5$ integrin receptor into the perinuclear region of HeLa cells was documented, which is devoid of the functional $\alpha_v\beta_3$ receptor. However, for the HeLa cells, which express the $\alpha_v\beta_3$ low level, a lower invasive potential than MCF-7 cells was demonstrated. **Figure 5.8a** and **Figure 5.9** show the cell uptake after incubation for a period of 2 h. The cRGD-free LQNBs took by MCF-7 and HeLa cells seemed to be arrested on the surface of MCF-7, and the same fluorescent signals can also be observed for HeLa cells (**Figure 5.8a**). In comparison, a significant difference in cellular uptake for the cRGD-encoded LQNBs by MCF-7 and HeLa cells for 2 h was determined, as given in **Figure 5.8a,** respectively. Numerous regions of strong green fluorescent emission displayed on the surface and the cytoplasm regions of the MCF-7 cells and some of them were closed to the nucleus (**Figure 5.9b**). However, poor green fluorescent illuminations presented in the regions of cytoplasm and surface of HeLa cells (**Figure 5.9c**). It can be concluded that the cRGD peptide on LQNBs surface was responsible for cell uptake behavior for those $\alpha_v\beta_3$-expressing cells.

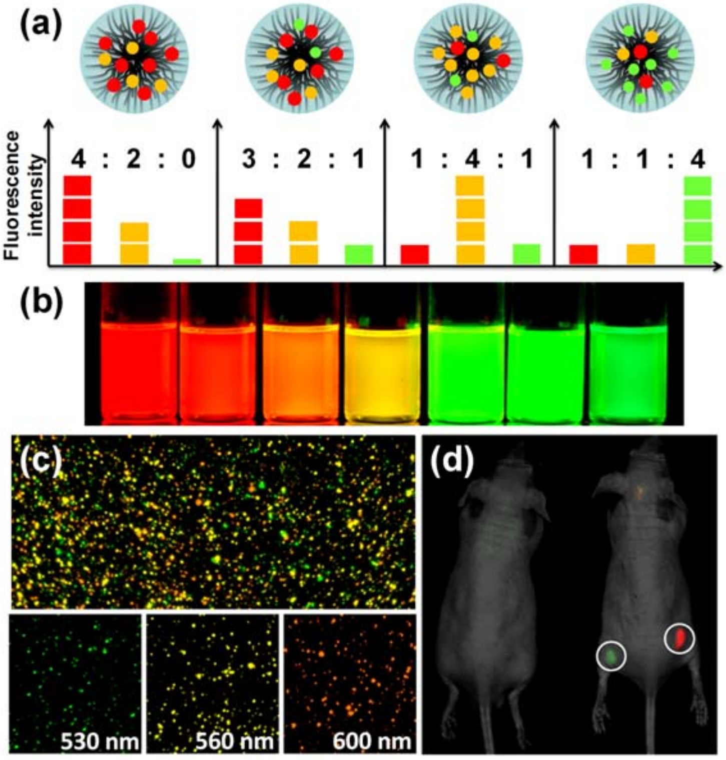

Figure 5.7 (a) Schematic illustration of optical coding based on wavelength and intensity multiplexing. (b) Seven distinguishable emission colors of QNBs excited with a near-UV lamp. From left to right (red to green), the emission maxima are located at 598, 586, 575, 558, 549, 541 and 532 nm. (c) Fluorescence images of nanobeads doped with single-color QDs emitting light at 530 (green), 560 (yellow), and 600 nm (orange-red). (d) Two kinds emitting light of LQNBs, green and red QDs, subcutaneously injected into a nude mouse. The left nude mouse is without injection.

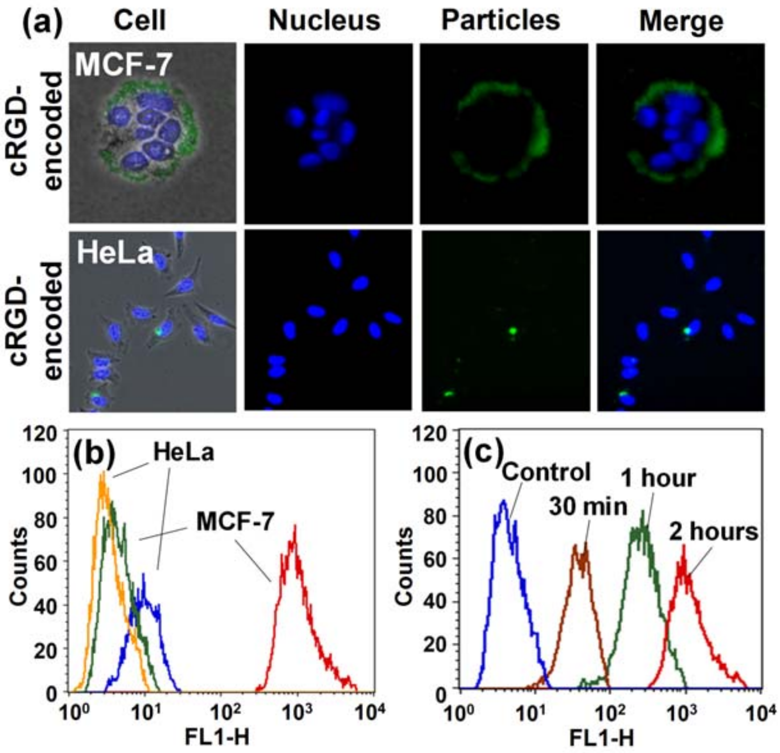

Figure 5.8 (a) The cell uptake for incubation 2 h with cRGD-encoded LQNBs to MCF-7 and HeLa cells. The cell nucleus is stained with DAPI (blue) and LQNBs emitted light at 530 nm (green). (b) Quantitative flow cytometric data shows that the fluorescence brightness and uniformity levels of cRGD-free and cRGD-encoded LQNBs uptake by MCF-7 and HeLa cells for incubation 2 h. (c) Flow cytometry analysis for the cRGD-encoded LQNBs accumulated in MCF-7 cells for incubation of 30 min, 1 h and 2 h.

A further investigation using flow cytometry toward the LQNBs with MCF-7 and HeLa cells is given in **Figure 5.8b.** The cRGD-free LQNBs taken by HeLa (orange) and MCF-7 (green) displayed uniform signal intensities but for the cRGD-encode LQNBs taken by MCF-7 (red), the signal intensity was 100 times higher than that taken by HeLa cells (blue). The comparison strongly indicated that the cRGD-encoded LQNBs with the normal $\alpha_v\beta_3$ expression level of MCF-7 cells were taken more efficiently than the $\alpha_v\beta_3$ low expressing HeLa cells which expressed the $\alpha_v\beta_5$ integrin and correlated with low invasiveness. The cRGD-encoded LQNBs were capable of penetrating the MCF-7 cells, **Figure 5.8c,** for a time period from 30 min to 2 h. The fluorescence intensity determined by flow cytometry rapidly increased, even clearly measurable at a starting 30-min period, further indicating a highly efficient cellular internalization. This finding ascertains the advantageous design of LQNBs for cell-specific contrast imaging. Furthermore, the result of the MTT (3-(4,5-dimethyldiazol-2-yl)-2,5 diphenyl tetrazolium bromide) assay as a measure of metabolic competence of the cells with the nanobeads, LQNBs and 3-mercaptopropionic acid (MPA)-functionalized QDs of different concentrations were shown in **Figure 5.10**. The LQNBs demonstrated equivalent toxicity to the nanobeads, indicating a relatively low or little cytotoxicity of these newly-designed nanobeads to the MCF-7 cells. As a critical requirement for targeting and imaging modalities using quantum dots, significant reduction of the cytotoxicity toward QDs through the use of the nanobeads can be critical. To this point, the multifunctionalized nanobeads designed and developed in this work are able to act as a potential contrast modality with improved not only imaging capability but also sufficient biocompatibility for medical practices.

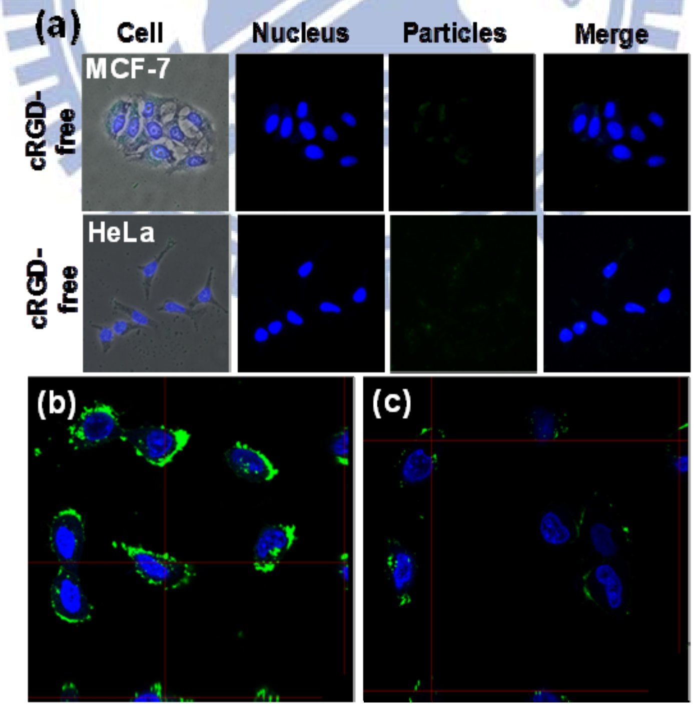

Figure 5.9 (a) The cell uptake for incubation 2 h with cRGD-free LQNBs to MCF-7 and HeLa cells. The cell nucleus is stained with DAPI (blue) and LQNBs emitted light at 530 nm (green). The CLSM images of cRGD-encoded LQNBs uptake with (b) MCF-7 cells and (c) HeLa cells.

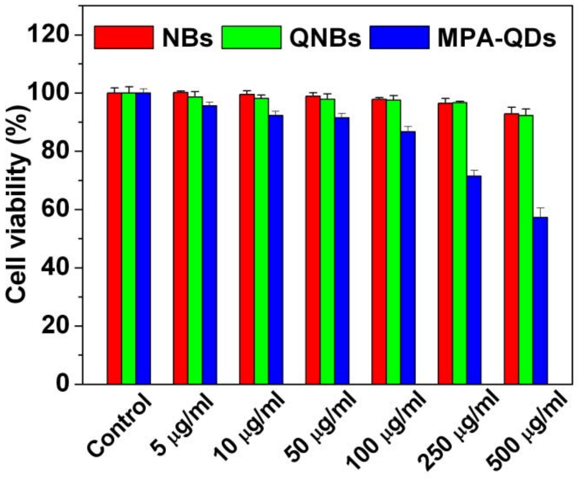

Figure 5.10 Cell viability of MCF-7 cells after 24 h of incubation with nanobeads, QNBs, and MPA-QDs.

5.7 *In vivo* target effect of cRGD-encode LQNBs

In vivo fluorescence and bioluminescence imaging of the nude mice bearing MCF-7 xenografts implanted after intracortical injection with 50 μL cRGD-free and cRGD-encoded LQNBs were shown in **Figure 5.11a, 5.11b**. For subcutaneously injected cRGD-free LQNBs, the fluorescence signals were rapidly decreasing at the tumor site after 1 day. The total flux (fluorescence intensity, TF) showed initial value 2.98×10^{10} p/s/cm^2/sr decreased by nearly 100-fold to 3.06×10^{8} p/s/cm^2/sr after 7 days. In comparison, the cRGD-encoded LQNBs presented long lasting signals and the TF value showed almost slowly decrease tendency (by about 5-fold only) from 3.04×10^{10} p/s/cm^2/sr to 6.03×10^{9} p/s/cm^2/sr. The TF values of cRGD-encoded LQNBs were higher by 20 times than cRGD-free LQNBs in 7 days. Clearly, the decrease in the rate of the fluorescent LQNBs in the tumor site is closely related to the cRGD peptide encoded or not. It is important to point out here that the cRGD-encoded LQNBs were responsible for targeting behavior for those $\alpha_v\beta_3$-expressing MCF-7 tumors. Therefore, the cRGD-encoded LQNBs exhibited moderately prolonged accumulation time at the MCF-7 tumor site but the cRGD-free LQNBs were disappeared rapidly at tumor site by

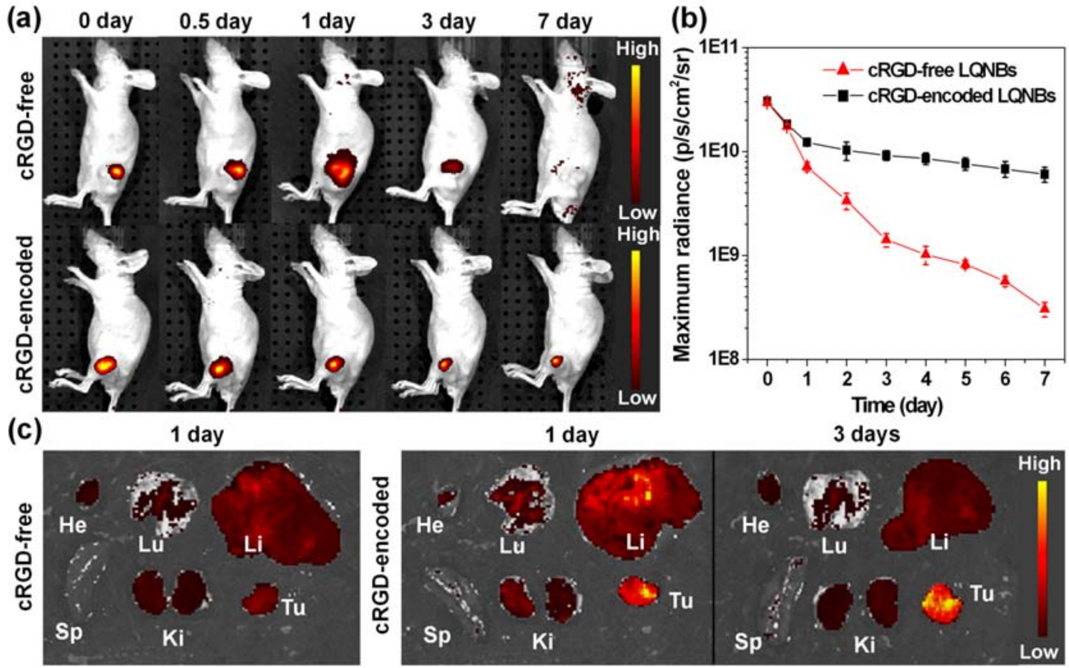

Figure 5.11 (a) *In vivo* fluorescence imaging of nude mice bearing MCF-7 xenografts implanted after subcutaneously injection with 50 µL cRGD-free and cRGD-encoded LQNBs in tumors. Total photon fluxes (TF) were determined at 0, 0.5, 1, 3 and 7 days using region-of-interest (ROI) measurement and expressed in photons/s. Color bar units are p/s/cm^2/sr, where p is for photon and sr is for steradian. (b) The change in luminescence over time for cRGD-free and cRGD-encoded LQNBs. (c) Photographic images of several organs and xenograft tumor from sacrificing the nude mice after intravenously injection with cRGD-free and cRGD-encoded LQNBs for 1 and 3 days. The organs are heart (He), lung (Lu), liver (Li), spleen (Sp), kidneys (Ki) and tumor (Tu).

blood circulation. **Figure 5.11c** shows the major organs from sacrificing the nude mice bearing MCF-7 xenografts implanted after intravenously injection with 50 µL cRGD-free and cRGD-encoded LQNBs. The fluorescence was barely detected in the heart and spleen, but observed in the kidneys, liver, and lung. Because intravenously injected nanoparticles arrived at the heart as first stop, followed by the lung, liver, and then other organs, we suspected that some aggregated nanoparticles were filtered by the lung, liver, and kidneys, resulting in accumulated fluorescent signal. However, the higher fluorescence intensity was observed in the tumor after intravenous injection with cRGD-encoded LQNBs compared to the cRGD-free LQNBs. Furthermore, the accumulations of the fluorescent (cRGD-encoded

LQNBs) became more pronounced after 3 days of injection. Thus, it can be conceivable that the cRGD-encoded LQNBs were able to provide targeting and imaging modalities for specific tumor cells.

5.8 Summary

Highly biocompatible cRGD-encoded lipid-coated QDs tagged porous nanobeads (cRGD-encoded LQNBs) were successfully developed for cancer targeting and imaging *in vitro* and *in vivo*. The larger pores of the octadecyltrimethoxysilane modified nanobeads facilitated the internalization and stabilization of QDs. The QDs tagged nanobeads showed highly chemical stability and a wide spectrum of multiplex color codings. *In vivo* and *in vitro* imaging studies showed a relatively sharp, stable and distinguishable contrast modality. Furthermore, cRGD-encoded LQNBs demonstrated a technically potential for visualizing the variations of uptake behavior between MCF-7 and HeLa cells, which may enable a further understanding on cellular behavior on a nanometric-to-molecular scale. In MCF-7 xenograft nude mice, the cRGD-encoded LQNBs also exhibited long lasting signals at the tumor site. With their nanostructural features, the cRGD-encoded LQNBs are expected to offer greater advantages in effective over a wide range of targeting and cellular imaging modality for minimally invasive nano-imaging and nanodiagnosis applications.

Chapter 6

A Novel Multifunctional Nano-platform with Enhanced Anti-cancer and Photoacoustic Imaging Modalities using Gold-nanorod-filled Silica Nanobeads

6.1 Introduction

The development of nanoobjects has gained considerable attention for a number of advanced applications in areas including biomedicine, therapeutics, complex materials and catalysis. Composite structures integrating multi-functionalities in a given nanometric volume with elaborate advantages of such as imaging and therapy modalities over their single constituent have been widely-studied topics for recent decades. In particular, a new imaging system, photoacoustic imaging, is a nonionizing and noninvasive imaging modality that combines the advantages of both optical and acoustic functionalities.[142-144] In photoacoustic imaging, the intensity modulated electromagnetic radiation, e.g., a beam of pulsed laser light, is directed at the imaging target. The light absorbed and converted to an outgoing thermoacoustic wave can be detected by an ultrasound transducer and used to reconstruct images.[145-147] Key factors for photoacoustic imaging efficiency are how many incident photons can be absorbed and converted to heat, and how fast generated heat can diffuse out from the target during thermoelastic expansion and wave generation. When a uniformly absorbing target is irradiated by pulsed laser, the amplitude of the generated photoacoustic signal is proportional to the optical absorption and the thermoacoustic properties of the absorbing medium. In contrast, in a heterogeneous medium containing plasmonic nanoobjects, the amplitude of the photoacoustic signal depends strongly on the transfer of heat between the two materials.[148] In recent studies, the photoacoustic imaging has been demonstrated successfully using gold nanorods, nanocages, and nanoshells with high and tunable optical absorption cross section. However, upon photoacoustic imaging, gold nanoobjects are exposed to high energy nanosecond laser pulses and easily collapseoriginal shape because of the generated heat, resulting in a reduction in absorption cross section and considerable variation of optical behaviors and reduction of imaging capability.[149] One important strategy to stabilize the nanostructure of gold nanoobjects is to physically trap the nanoobject in a confined and thermally-stable entity, such as carbon, silica and polyethylene glycol (PEG).[150,151] However, most chemical modifications are complex, time-consuming and even in a risk of losing original function of the starting nanomatrix. Therefore, a major challenge is how to engineer molecular probes with integrated functionalities while still maintaining compact geometry, photothermal stability, and biocompatibility. Furthermore, it is highly desirable that the nanoobjects with coupled functionalities will enable new imaging modes not available from each individual component for enhanced contrast specificity.

Recently, gold nanostructure (AuNSs), in a geometric form of spherical nanoparticles, nanorods and /or nanoshells, has been actively investigated and well recognized as a promising and versatile platform for cancer treatments. Due to tunable localized surface plasmon resonance (LSPR), nanometric gold has recently been explored to induce hyperthermal cytotoxicity.[152] When irradiated with a laser through the photothermal effect, the conduction-band electrons of the nanostructured gold generate heat that is transmitted to the cells and surrounding tissues. Thermal therapy provides advantage of killing cancer cells without causing resistance regardless of the genetic background, and thus can be applied to all cancer patients. A key factor contributing to clinical therapies requires adequate accumulation of nanometric gold in the tumor site and sufficient tumor penetration of the excitation energy. However, in current studies, the tumor delivery of AuNSs has been relied on the enhanced permeability and retention (EPR) effect, a result of tumor blood vessel leakiness due to a state of ongoing angiogenesis, [153] which thus has not been very efficient because AuNSs accumulate unevenly in the tumor site depending on particle size, surface charge, and other factors, [154,155] which makes it difficult to eradicate the whole tumor tissue with this approach. Therefore, the development of multifunctional nanoobjects enabling new imaging and therapy modalities beyond the intrinsic limitations of individual components is essential.

Here, we report a new nano-seaurchin structure where the nanoporosity within uniform mesoporous silica nanobeads was filled with gold nanorod, giving a multifunctional nanoprobe capable of performing photoacoustic imaging and thermotherapeutics. This multifunctional nanoprobe was fabricated in a facile, step-wise procedure, including (1) formation of 3-aminopropyltrimethoxy silane-functionalized mesoporous silica nanoparticles with pore size greater than 10 nm, (2) seeding of gold nanoparticles in the cavity of porous silica, (3) confined growth of gold initiated from the embedded gold precursor, forming high density gold nanorods conformed with the nanoporosity of the porous silica. This multifunctional nanoprobe, to our knowledge, provides exceptionally highly photothermal stability and tunable heating capability, which offers potential advantages for anti-cancer purpose and photoacoustic imaging.

6.2 Experimental section

Synthesis of porous silica nanobeads (NBs): 300 mg cetyltrimethylammonium bromide (CTAB) was dissolved in a mixture of 45 ml octane and 96 ml dilute water at 70°C. After stirred magnetically for 20 min, 8.5 ml styrene monomer, 66 mg lysine, 3000 mg tetraethylorthosilicate (TEOS), and 115 mg AIBA were subsequently added to the system and stirred magnetically for 4 h. After 4 h, the heating was stopped and the suspension was cooled naturally to room temperature. The products were collected by centrifugation at 6000 rpm for 10 min and then washed 3 times with an excess of pure methanol. Finally the template was completely removed by heat treatment at 600°C under atmospheric conditions.

Gold seed filled porous silica nanobeads (AuSNBs): CTAB solution (5 mL, 0.20 M) was mixed with 5.0 mL of $HAuCl_4$ (0.0005 M). To the stirred solution, 0.60 mL of ice-cold

0.010 M $NaBH_4$ was added, which resulted in the formation of a brownish yellow solution. Vigorous stirring of the seed solution was continued for 2 hours. After the solution was stirred, it was kept at 25 °C. Furthermore, incorporation of gold seeds was achieved by swelling 1 mM porous silica beads with 1 ml seed solution and stirred magnetically for 2 h. The products were collected by centrifugation at 10000 rpm for 10 min and then were redispersed into dilute water (1 ml).

Templated synthesis of gold nanorods filled porous silica nanobeads (AuRNBs): CTAB (5 mL, 0.10 M) was added to (0.02, 0.04, 0.06, 0.08, 0.10 mL) of 0.01 M $AgNO_3$ solution at 25 °C. To these solutions, 0.5 mL of 0.01 M $HAuCl_4$ was added, and after gentle mixing of the solution, 55 μL of 0.1 M ascorbic acid was added. Ascorbic acid as a mild reducing agent changes the growth solution from dark yellow to colorless. The final step was the addition of 20 μL of the seed solution (AuSNBs) to the growth solution at 27-30 °C. The color of the solution gradually changed within 10-20 min. For longer NRs, the color change takes place more slowly. The temperature of the growth medium was kept constant at 27-30 °C in all the experiments and stirred magnetically for 24 h.

Selective etching of the gold nanorods filled porous silica nanobeads: The 3 mL gold nanorods filled porous silica nanobeads (AuRNBs) were dispersed in 30 mL of NaOH solution (0.25 M) to obtain gold nanorods. The dispersion was stirred at room temperature for 1 h. Product was collected by centrifugation at 10000 rpm for 10 min and washed with water until neutral pH.

Volume fraction of gold nanorods in nanobeads: The atomic concentration fraction of gold (Au) to silicon (Si) was analyzed to be 0.186 from inductively coupled plasma (ICP). The volume fraction of Au nanorods is determined using the equation (5) :

$$\frac{\text{Au (ppm)}}{\text{Si (ppm)}} = \frac{\text{Au (mmol)}}{\text{Si (mmol)}} = \frac{\text{Au (mol)}}{\text{Si (mol)}} = 0.186$$

$$\frac{\mathrm{Au}\ (\mathrm{v}\%)}{\mathrm{SiO_2}(\mathrm{v}\%)} = \frac{\mathrm{Au}\ (\frac{\mathrm{gcm^3}}{\mathrm{g}})}{\mathrm{SiO_2}\ (\frac{\mathrm{gcm^3}}{\mathrm{g}})} = \frac{\frac{\mathrm{Au\ (mol)}}{\mathrm{D_{Au}}}\ \mathrm{x}\ \mathrm{m_{Au}}}{\frac{\mathrm{SiO_2\ (mol)}}{\mathrm{D_{SiO2}}}\ \mathrm{x}\ \mathrm{m_{SiO2}}} = \frac{\mathrm{Au\ (mol)\ x}\ \frac{\mathrm{m_{Au}}}{\mathrm{D_{Au}}}}{\mathrm{Si\ (mol)\ x}\ \frac{\mathrm{m_{SiO2}}}{\mathrm{m_{Si}}}\ \mathrm{x}\ \frac{\mathrm{m_{SiO2}}}{\mathrm{D_{SiO2}}}}$$

$$= 0.0837 = 8.37\%$$

, where m_{Au} (196.97), m_{Si} (28.08) and m_{SiO2} (60.08) are the molecular weight of Au, Si and SiO_2, respectively. D_{Au} (19.3 g/cm^3) and D_{SiO2} (2.648 g/cm^3) are the density of Au and SiO_2, respectively.

6.3 Preparation of mesoporous silica nanobeads with gold nanorods filled nano-seaurchin structure (AuRNBs)

Figure 6.1 illustrates the synthesis of mesoporous silica nanobeads with gold nanorods filled nano-seaurchin structure (AuRNBs). The first step is to synthesize the 3-aminopropyltrimethoxy silane-functionalized mesoporous silica nanobeads using an organic template method. The morphology and particle size of the porous nanobeads were analyzed using scanning electron microscopy and transmission electron microscopy, as shown in **Figure 6.2a** and **6.2b**, respectively. Monodispersed spherical porous nanobeads with an average size of 125 nm in diameter were observed. As well-known, gold species, including $AuCl_4^-$ and metallic gold, have a high affinity to amino groups due to electrostatic and/or

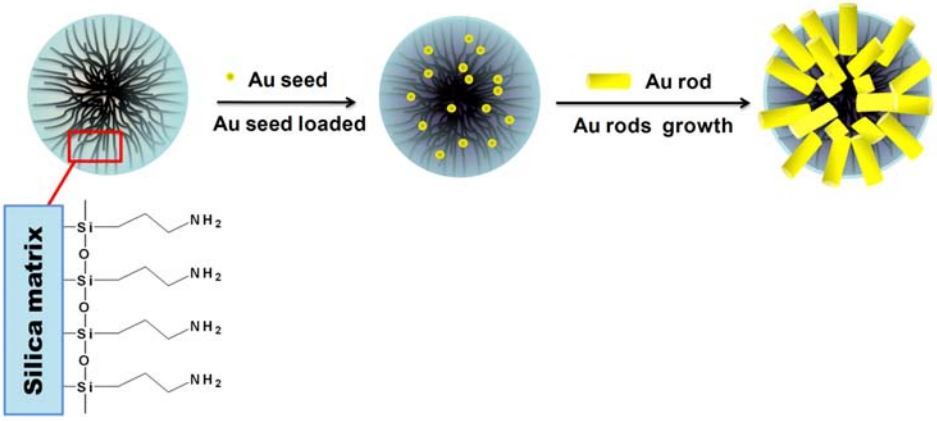

Figure 6.1 Schematic illustration of the synthesis and structure of the mesoporous silica nanobeads with gold nanorods filled structure (AuRNBs).

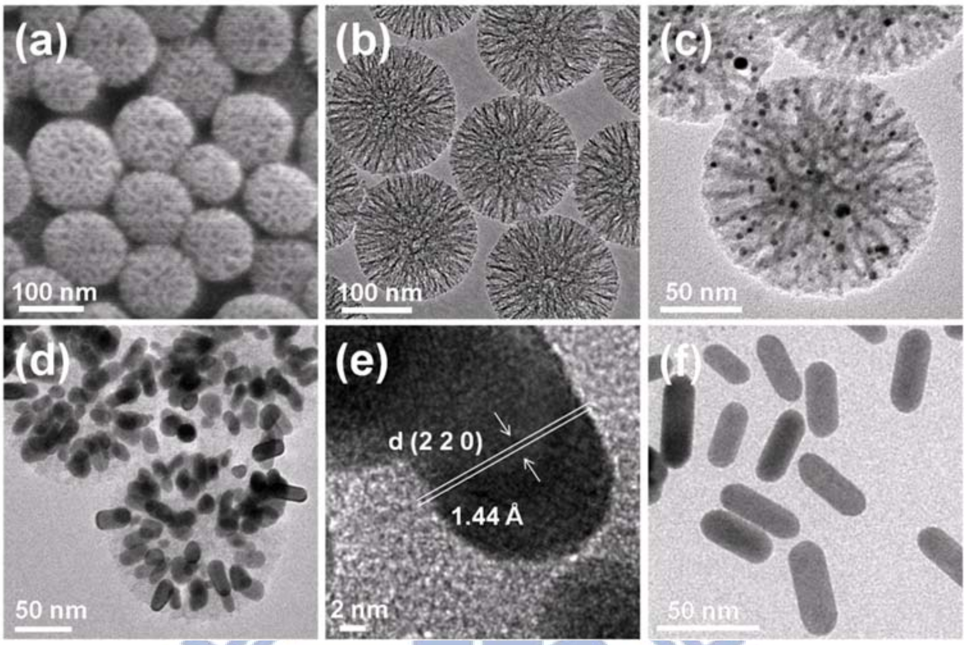

Figure 6.2 (a) SEM image and (b) TEM image of porous nanobeads. (c) TEM image of the gold seeds formed inside silica nanobeads (AuSNBs). (d) TEM image of mesoporous silica nanobeads with gold nanorods pore-filled structure (AuRNBs). (e) High resolution TEM image of mesoporous silica nanobeads gold nanorods pore-filled structure, which showed that lattice spacing of 1.44 Å for Au nanorods (2 2 0) plane. (f) TEM image of well-defined AuRNBs after removing the silica matrix by sodium hydroxide (NaOH) etching.

coordinate interactions. The selective modification of the inner surface of the silica nanobeads with amino group allows the retention of gold species inside the templates during the chemical adsorption of gold seeds. Thus, the gold seeds were intermolecularly inserted to form a stable, interdigitated configuration. After seeding, gold nanoparticles about 4 nm in size were formed within the porosities of each silica nanobead (**Figure 6.2c**). No obvious nucleation of the gold seeds deposited along the outermost regions of the silica nanobeads has been observed. Furthermore, the key in the growth step of gold seeds is to maintain a low reaction rate and minimize self-nucleation events. For example, we used ascorbic acid as a weaker reducing agent to replace $NaBH_4$ for the reduction of gold salt. To further slow down the gold growth, a coordinating ligand, potassium iodide (KI), was introduced, which reacted with $AuCl_4^-$ forming a stable complex AuI_4^- with a strong Au-I affinity.[156] An additional capping ligand, typically polyvinylpyrrolidone (PVP), was also added to the solution to stabilize the atomic monomer species and further delay the self-nucleation.[157] PVP also has the function of preventing the final products from agglomeration. After the seed-carrying nanobeads (AuSNBs) were immersed into the gold growth solution, the growth of gold seeds occurred as evidenced by the color change of the mixture, forming the silica nanobeads with AuR-filled structures, wherein the Au grew into a nanorod geometry to fill up the nanocavity of silica matrix (**Figure 6.2d** and **Figure 6.2e**). The silica nanobeads with AuR-filled structures (AuRNBs) were further evidenced using the energy-dispersive X-ray spectroscopy by TEM (**Figure 6.3**). Furthermore, well-defined gold nanorods were obtained after dissolving the silica matrix by sodium hydroxide (NaOH) etching, as shown in **Figure 6.2f**, where the resulting gold nanorods exhibited a uniform size, substantiating a successful Au growth in confined nanospace. A Brunauer-Emmett-Teller (BET) analysis also showed a considerable reduction of surface area and average pore size from 862.25 m^2g^{-1} and 6.5 nm (radius) to 128.96 m^2g^{-1} and 2.1 nm (**Figure 6.4**), which supported that the nanoporosity of the silica nanobeads was extensively filled up by the gold nanorods.

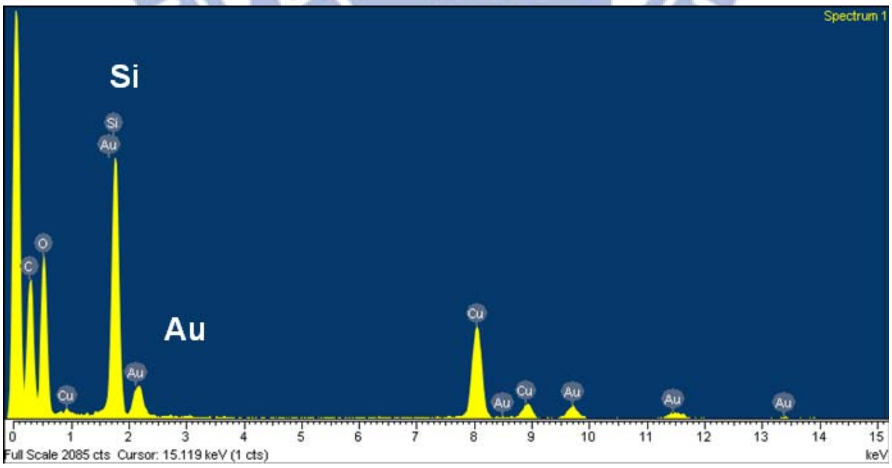

Figure 6.3 The energy-dispersive X-ray spectroscopy of the mesoporous silica nanobeads with gold nanorods pore-filled structure by TEM.

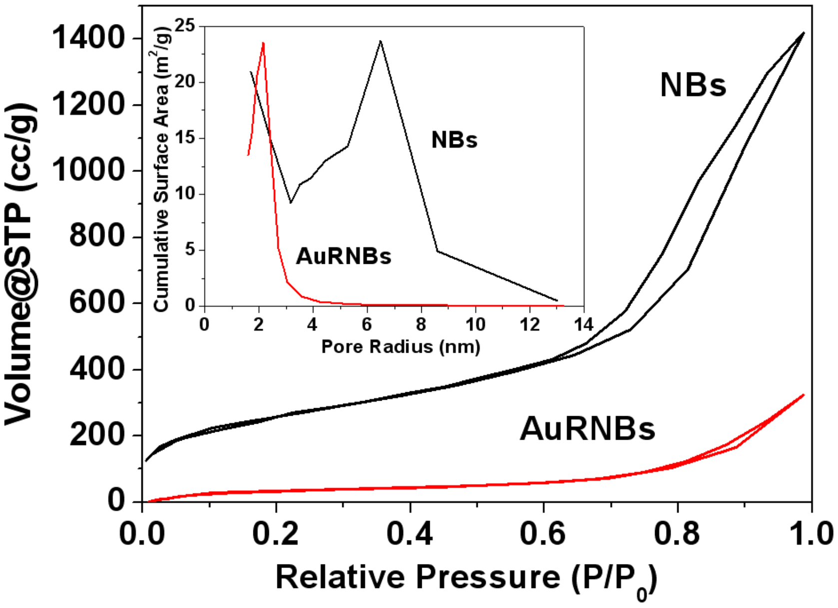

	Surface area (m²/g)	Pore volume (cc/g)	Pore radius (nm)
NBs	862.25	1.908	6.5
AuRNBs	128.96	0.378	2.1

Figure 6.4 The N_2 adsorption/desorption isotherms of the nanobeads with Brunauer-Emmett-Teller (BET). The inset showed that the Barret-Joiner-Halenda (BJH) analysis of the nanobeads and AuRNBs.

6.4 Growing gold nanorods with different aspect ratios

The growing gold nanorods with different aspect ratios can be easily manipulated by adjusting the silver ion ($AgNO_3$) content in the growth solution. **Figure 6.5a** shows the effect of adding identical growth solution to 20-100 μL of 0.01M $AgNO_3$ solution. It can be seen that by controlling the silver concentration, the longitudinal plasmonic band of AuRNBs can be adjusted. Structural morphology and size distribution of the Au nanorods of varying aspect ratios were examined using TEM as shown in **Figure 6.5b** and **6.5c**, and **Figure 6.6**, respectively. With the average aspect ratio increasing from 2.3 to 4.5, the longitudinal plasmonic band was subjected to an extensive red-shift from 636 to 821 nm, which is close to the values predicted by theoretical calculations ($\lambda_{max} = 95R + 420$ nm; R: aspect ratio).

6.5 Thermal stability of AuRNBs

The thermal stability of pure gold nanorods, as well as AuRNBs was compared using UV-vis spectroscopy. The longitudinal plasmonic peak is a good indicator for shape changes of the nanorods, because the peak position strongly depends on the aspect ratio of the nanorod. Indeed, after irradiating the pure AuR and AuRNBs with 10 mJ/cm^2 pulse laser at 100 to 1500 laser pulses, the shape and intensity of the longitudinal plasmonic peak were changed in all cases (**Figure 6.7a, 6.7b**). The fluences 10 mJ/cm^2 induced a 30% reduction in amplitude for the gold nanorods after 100 laser pulses, while about 10% reduction was observed for AuRNBs. Further increasing the number of laser pulses led to a dramatic decrease in the spectral amplitude, a strong blue shift of the longitudinal peak and a strong increase of the absorption in the 600-700 nm range were detected, which are all consistent with a rounding of the gold nanorods. In contrast, the porous silica matrix introduced a stabilizing effect onto the gold nanorods. Although above 1000 laser pulses the peak only slightly decreased, no shoulder in the 600-700 nm range was evolved. It is therefore clear that the gold nanorods

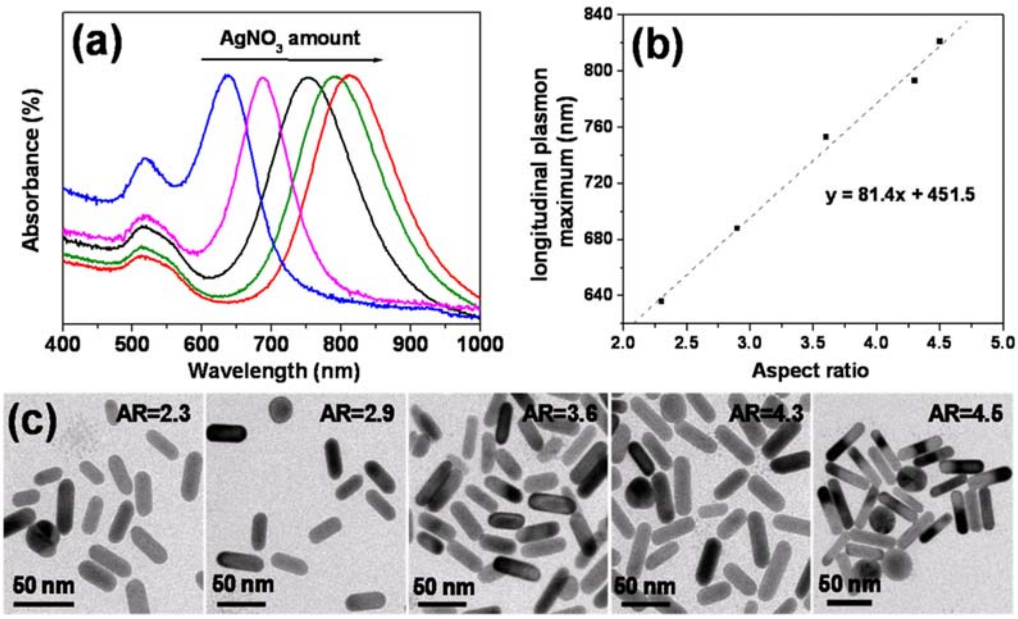

Figure 6.5 (a) Extinction spectra of AuRNBs by controlling the aspect ratio during varying the silver ion ($AgNO_3$) content in the growth solution. (b) The longitudinal plasmon maximum effect with different aspect ratio. (c) AuRNBs after removal of silica matrix.

LSPR (nm)	$AgNO_3$ (μL)	Length (nm)	Width (nm)	Aspect ratio
636	20	28.7	12.5	2.3
688	40	35.2	12.1	2.9
753	60	40.7	11.3	3.6
793	80	47.7	11.1	4.3
821	100	49.1	10.9	4.5

Figure 6.6 Different aspect ratio of the AuRNBs.

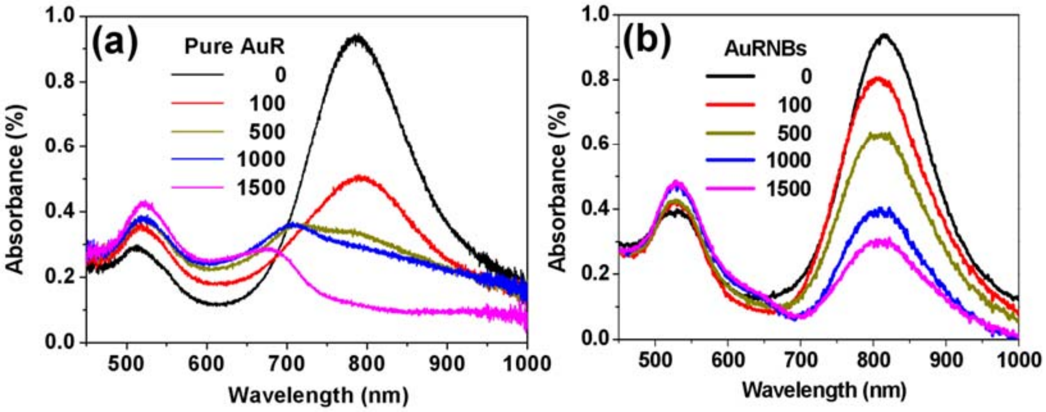

Figure 6.7 Measured UV-Vis extinction spectra of (a) pure AuR and (b) AuRNBs before and after irradiation with various laser pulses.

physically confined within the porous silica nanobeads were stabilized from structural collapsing, ensuring high and stable emitting efficiency, suggesting that the newly-synthesized AuRNBs can be a promising contrast substance for photoacoustic imaging application.

6.6 Mechanism for the photoacoustic signal enhancement

The amplitude of the photoacoustic signal at nanosecond time scales is related to the temporal temperature gradient generated in the surrounding medium by heat dissipation from the nanorod. **Figure 6.8** shows a mechanism for the photoacoustic signal enhancement from gold nanorod-filled nanobeads, emphasizing the importance of the heat transfer to the water. Pure gold nanorods have a slower heat transfer resulting in a broader heat peak due to their interfacial properties, but the gold nanorods filling in silica nanobeads can reduce the interfacial resistance and lead to a sharper peak. Furthermore, the gold nanorods filled nanobeads shows three-fold higher photoacoustic signal amplitude than pure gold nanorods. We therefore expected that the photoacoustic signal enhancement must come from an increased thermal transfer through the gold interface. Thus, the porous silica nanobeads with AuR-filled structure could amplify the photoacoustic response by increasing the interfacial heat conduction from gold to water due to the presence of silica matrix.

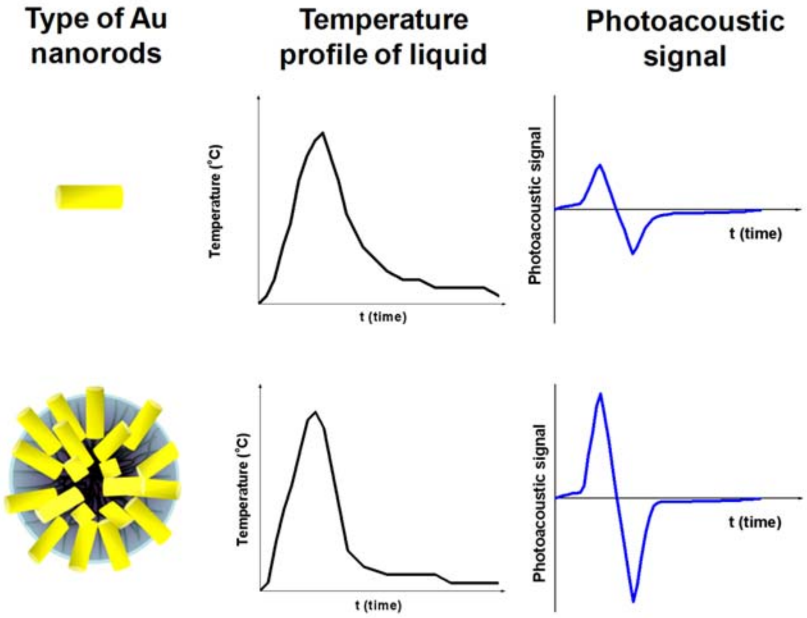

Figure 6.8 The proposed thermal transport processes from the nanoparticle to the environment and resulting temporal profiles of the temperature and the amplitude of the photoacoustic signal.

6.7 *In vitro* and *in vivo* photoacoustic signal of pure AuR and AuRNBs

For *in vivo* measuring the efficiency of the photoacoustic signal of pure AuR and AuRNBs, the mouse which bore a CT26 tumor (mouse colon cancer) was intravenously injected with AuRNBs solution (200μL, 1mg mL^{-1}). Three-dimensional ultrasound and photoacoustic images of the tumor site and its surrounding are acquired before and up to 16 h after injection (**Figure 6.9a**). We found that mice injected with AuRNBs showed a significant increase of photoacoustic signal in tumor site compared with injected with pure AuR. The images from different time intervals were aligned with one another using simple vertical translations to account for small vertical movements in the transducer positioning. This alignment allowed quantification of the photoacoustic signal at all time points using a single region of interest. We then calculated a subtraction photoacoustic image signal between the photoacoustic image taken at 16 h post-injection and the image taken before injection. The photoacoustic signal was calculated by drawing a 3D region of interest around the tumor (tumor boundaries were clearly visualized in the ultrasound images). The quantified photoacoustic signal is increased as a function of time as shown in **Figure 6.9b**. At pre-injection, there is no photoacoustic signal in tumor site. Conversely, at the 16 h post-injection, mice injected with AuRNBs showed a significantly higher photoacoustic signal than mice injected with pure AuR, indicating that the AuRNBs bind to the tumor site more than pure AuR. On average, at 16 h post-injection, the AuRNBs demonstrated 4.7 times higher intensity in photoacoustic signal compared with pure AuR, which is indicative of a promising contrast agent for photoacoustic imaging modalities.

6.8 Cell uptake

Cellular uptake of the FITC-labeled AuRNBs (green color emitted) was monitored by confocal laser scanning microscopy (CLSM). **Figures 6.10a and 6.10b** show that the AuRNBs are gradually internalized after incubating with the MDA-MB-231 cell for 4-h and 12-h durations. The green fluorescent dye was clearly observed in the region of cytoplasm over short time periods of incubation. For 4-h incubation, some of the nanoobjects appeared to attach rapidly to the cell membranes. However, numerous regions of the cytoplasm displayed strong green fluorescent emission at 12 hours. This observation implies that the

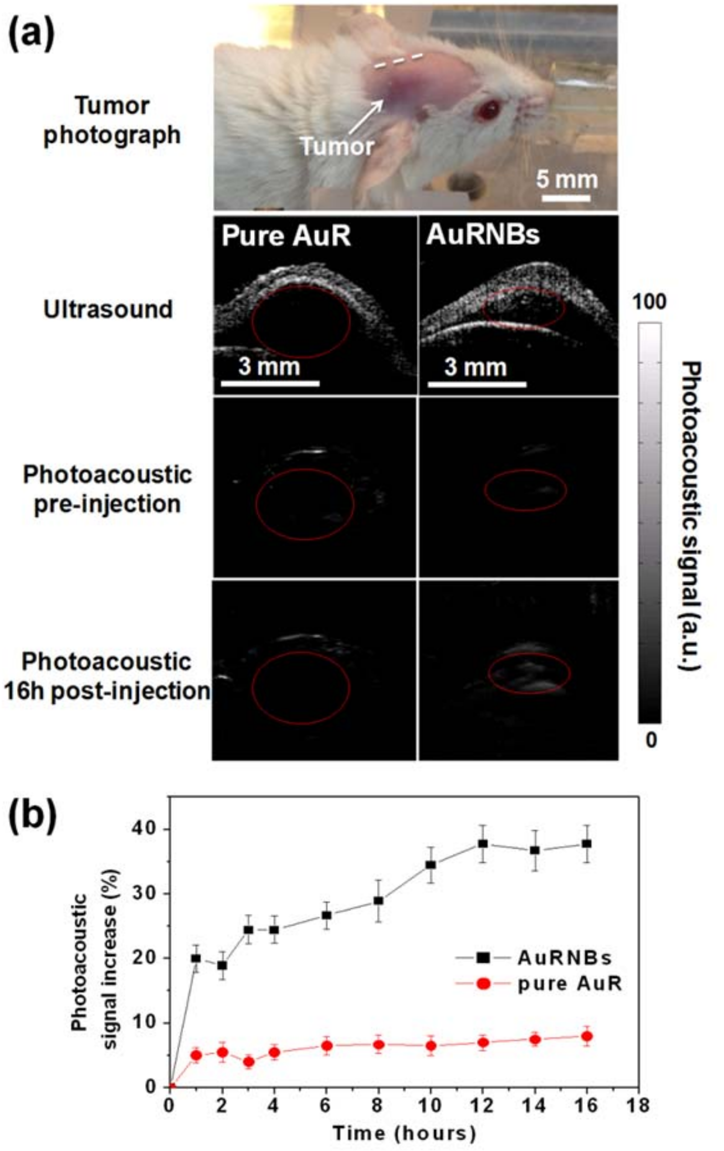

Figure 6.9 (a) Ultrasound and photoacoustic images of one vertical slice through the tumor. The ultrasound images show the skin and tumor boundaries. Subtraction images were calculated as the 16 h post-injection image minus the pre-injection image. (b) Mice injected with AuRNBs showed a significantly higher photoacoustic signal than mice injected with pure AuR.

nanoprobes can be internalized rapidly upon cellular uptake. A further investigation using flow cytometry toward the AuR and AuRNBs with MDA-MB-231 cells is given in **Figure 6.10c**. The AuR taken by MDA-MB-231 (blue color) displayed low signal intensity but for the AuRNBs (brown color), the signal intensity was 30 times higher than that of AuR in 4 h incubation. There are high density gold nanorods in one AuRNBs. That is to say, when the cancer cells uptake one AuRNBs nanoparticles, it is equal to uptake several pure AuR. Thus, AuRNBs showed higher fluorescence intensity than pure AuR. Furthermore, for a time period from 4 h to 12 h, the fluorescence intensity determined by flow cytometry rapidly increased, indicating a highly efficient cellular internalization.

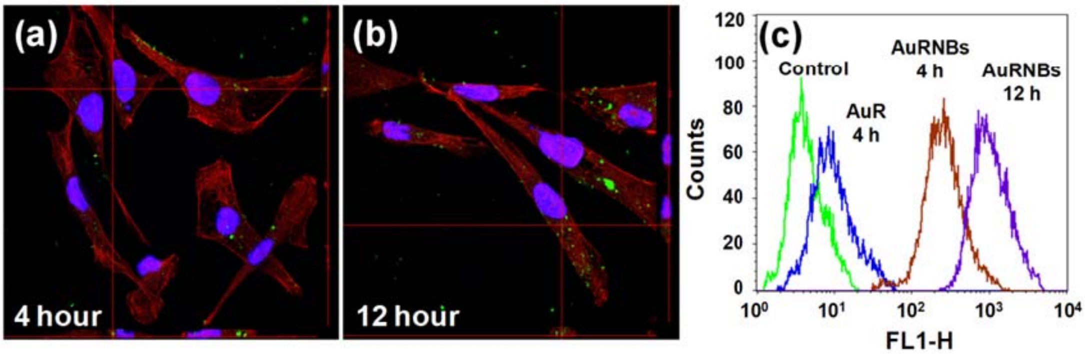

Figure 6.10 Time-course PL microscopy images of MDA-MB-231 cells labeled with FITC-AuRNBs nanoprobes and incubated for (a) 4 hour and (b) 12 hours. The cell skeleton was stained with rodamin phalloidin (red), and the cell nucleus with DAPI (blue). (c) Quantitative flow cytometric data shows that the fluorescence brightness and uniformity levels of pure AuR and AuRNBs uptake by MDA-MB-231 for incubation 4 h and 12h.

6.9*In vitro* photothermal efficacy and cell viability

To evaluate photothermal efficacy, a NIR wavelength of 808 nm with 2 W/cm^2 was irradiated to MDA-MB-231 cells for 2 min incubated with AuRNBs for 24 hr at. Before and after irradiation, the cells were stained with clacein AM and ethidium homodimer (EthD-1) to characterize cell viability: live cells appeared in green and dead cells appeared in red. Before irradiation, live cells (green) are highly visible in the entire region as shown in **Figure 6.11a**. After irradiation, the region irradiated—its boundary marked by a white dash line in **Figure 6.11b**—has almost no live cells and the dead cells are stained with red color, indicating that irradiation has killed almost all cells. The result of the MTT (3-(4,5-dimethyl diazol-2-yl)-2,5 diphenyl tetrazolium bromide) assay as a measure of metabolic competence of the cell with different concentrations of the NBs (silica nanobeads), AuSNBs (AuS-filled silica nanobeads) and AuRNBs (AuR-filled silica nanobeads) were shown in **Figure 6.11c**. The nanoparticles

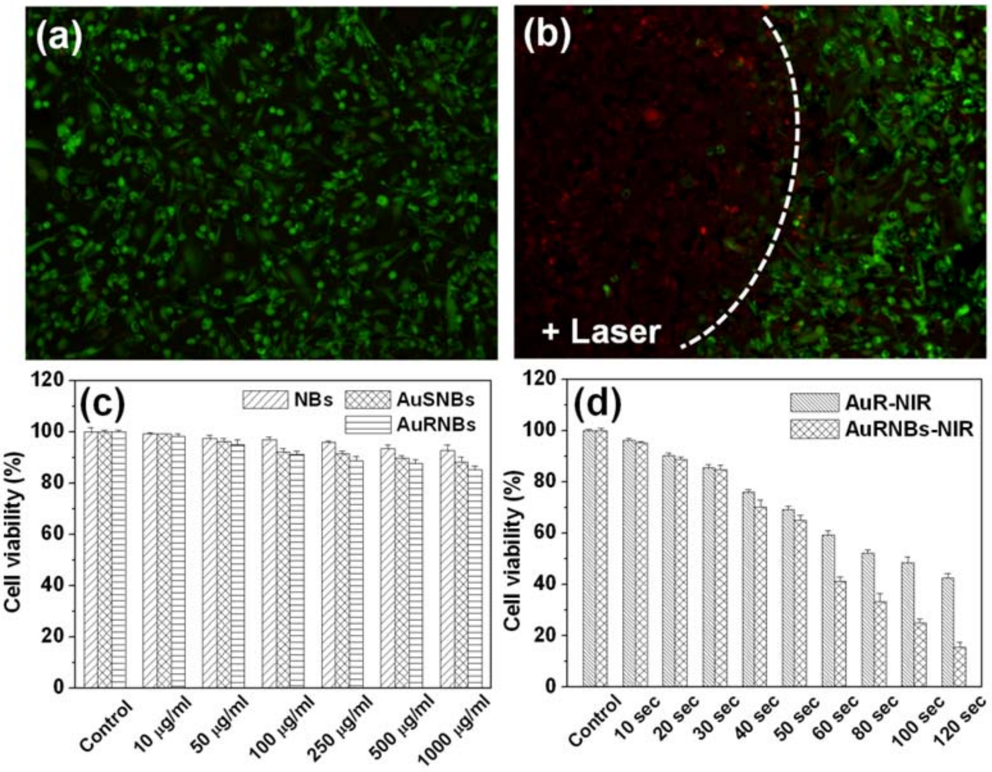

Figure 6.11 (a) Before irradiation, cells incubated with AuRNBs. Live cells were stained with clacein AM to appear in green. (b) After irradiation (808 nm for 2 min, in region left of the marker curve), essentially all cells were killed and the dead cells were stained with ethidium homodimer (EthD-1) to appear in red. (c) Cell viability of MDA-MB-231 cells after 24 h of incubation with nanobeads, AuSNBs, and AuRNBs. (d) Cell viability of MDA-MB-231 cells after 24 h of incubation with pure AuR and AuRNBs versus duration of irradiation.

were incubated with MDA-MB-231 cancer cells for 24 hours. The AuSNBs and AuRNBs demonstrated equivalent cell viability to the NBs, indicating a relatively low or little cytotoxicity of these newly-designed AuRNBs to the MDA-MB-231 cells. To evaluate photothermal therapy, we irradiated MDA-MB-231 cells administrated with AuR and AuRNBs (the same dose of gold, incubated for 24 hr) at a NIR wavelength of 808 nm with 2 W/cm^2 for different irradiated time and monitored cell viability as shown in **Figure 6.11d**. With increasing NIR laser treatment time, the cell viability of MDA-MB-231 obviously reduced. However, after irradiation, the AuRNBs showed the lower cell viability than pure AuR. From flow cytometric data **(Figure 6.10c)**, the cell uptake efficiency of AuRNBs are higher than pure AuR under the same concentration and incubation time, which accordingly the AuRNBs should expect to have higher hyperthermia efficiency than that from pure AuR upon NIR laser treatment.

6.10 *In vivo* photothermal efficacy

For *in vivo* measurement of light-to-heat efficiency of AuRNBs, infrared thermal mapping apparatus was used to monitor the temperature raise when 808 nm NIR laser irradiated onto MDA-MB-231 tumor-bearing nude mouse (~5.5 mm × 5.5 mm) as shown in **Figure 6.12a**. The mouse was intravenously injected with AuRNB-containing solution (200µL, 1mg mL^{-1}) and then anesthetized with isoflurane and irradiated the tumor region with NIR light (2 W cm^{-2}) at 12 h post-injection. During this irradiation for 2 min, the temperature of the tumor site obviously increased from 31.2°C to 68.4°C in the focal region due to electron-phonon and phonon-phonon process of the NIR absorbing AuRNBs (**Figure 6.12b**). Then, another MDA-MB-231 tumor-bearing nude mouse was intravenously injected with 200µL phosphate saline-buffered solution (PBS buffer). The nude mouse was also irradiated and monitored on the tumor site under the same irradiation control. No obvious temperature variation was observed in the control group (**Figure 6.12c**). **Figures 6.12d, 6.12e, and 6.12f** show the MDA-MB-231 tumor-bearing nude mouse intravenously injected with AuRNBs solution and irradiated for 2 min with NIR laser as pretreatment, and monitor at day 2 and day 14. At day 2, the mice had small scars on the skin at the tumor site with a dark gray color, but the scars on mice fell off at day 14. As shown in **Figure 6.12g**, the tumor injected with AuRNBs via a single dose of irradiation with NIR laser completely regressed, whereas tumors in the control group were under developing after 14 days. On this base, it can be conceivable that the AuRNBs currently developed in this study are proved to be a potential photothermal therapeutic vehicle with exceptionally higher heating efficiency than conventional pure Au nanoobjects for anti-cancer therapy.

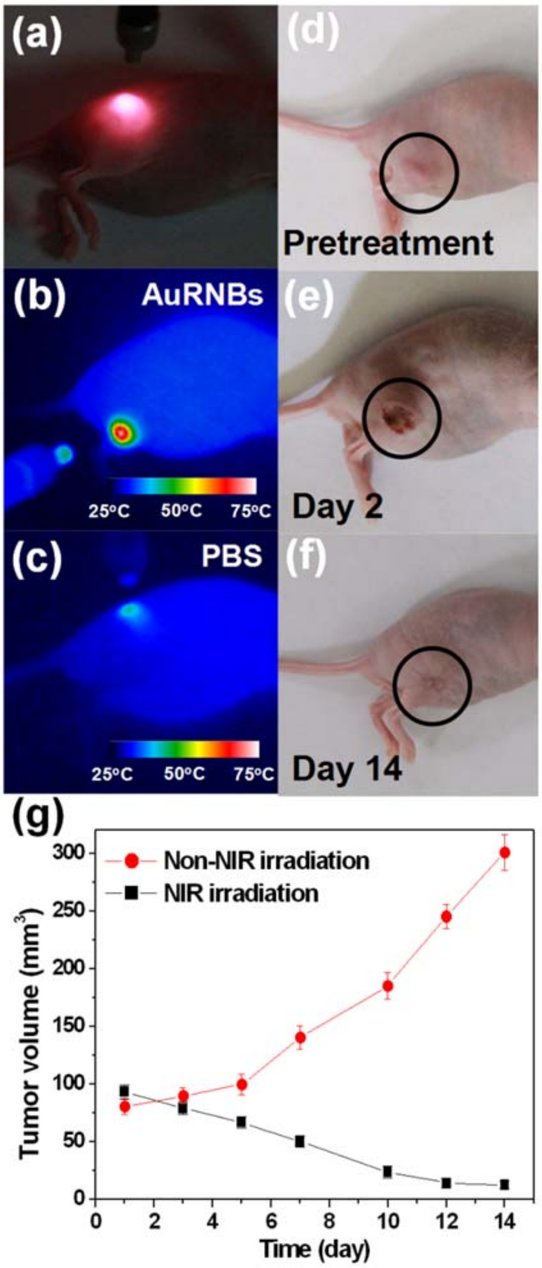

Figure 6.12 (a) (b) (c) converting light absorption into heat by the photothermal effect of AuRNBs and PBs, and infrared thermal mapping apparatus was used to monitor the temperature increasing when 808 nm NIR laser irradiated a MDA-MB-231 tumor-bearing nude mouse. (d) (e) (f) the MDA-MB-231 tumor-bearing nude mouse intravenously injected with AuRNBs solution and irradiated 2 min on the tumor site with NIR laser for pretreatment, treatment after 2 days and 14 days. (g) The volume of tumor variation by treated with NIR light.

6.11 Summary

Highly biocompatible mesoporous silica nanobeads with pores filled with gold nanorods (AuRNBs), showing a nano-seaurchin structure, were successfully developed for cancer treatment and photoacoustic imaging *in vitro* and *in vivo*. The larger pores of the 3-aminopropyltrimethoxy silane modified nanobeads facilitated the internalization and stabilization of gold seeds, further forming the high density, well-dispersive conformal and spectrum-controllable gold nanorods structure. The silica nanobeads with gold nanorods filled structure showed highly thermal stability after laser pulses. *In vivo* and *in vitro* photoacoustic imaging studies showed a relatively enhancement contrast modality. The enhancement could be attributed to changes in the interfacial heat conduction from gold to water due to the silica. Furthermore, AuRNBs demonstrated highly cell uptake efficiency, low toxicity and photothermal therapeutic with exceptionally high heating efficiency. Together with a well-regulated design, the AuRNBs are expected to act as a potential photoacoustic imaging contrast modality with improved not only biocompatibility but also effectively photothermal therapy for nano-imaging applications.

Chapter 7

Magnetic Mesoporous Silica Nanobeads Filled with Gold Nanorods for Dual-modal Imaging-Guided Stem Cell Therapy under Magnetic Remote-Controlled

7.1 Introduction

Stem cell, can be utilized for regenerative therapy and treatment of several diseases, including amyotrophic lateral sclerosis, acute myocardial infarction, liver cirrhosis, Parkinson's disease, and repairing of various damaged with their differentiation and tropism. Development of this stem cell-based therapy requires monitoring the fate and distribution of transplanted cells to maximize the therapeutic benefit. Specific limitations to stem cell therapy include cell death, contamination by undifferentiated cells, and cell delivery to untargeted areas.[158] In one of the first human examples of stem cell therapy, cells were misinjected in 50% of patients.[159] In that study, cell imaging during injection could not be performed and the poor injection rates were not identified until postprocedure magnetic resonance imaging (MRI) analysis. Although local delivery improves accuracy, there is no way to image and quantify the number of cells accumulating at the target site in a real-time manner. Indeed, it is currently unclear whether the lack of response observed in some stem cell therapy is due to poor biology or poor graft delivery. Although many researches have been involved with the stem cell-based therapy technology, there are still exist some problems for stem cell-based therapy, such as (1) from intravenous injection, almost 90% stem cells were metabolized to the liver and lung, less than 10% moving to the target site. (2) stem cell-based therapy requires monitoring the fate and distribution of transplanted cells to maximize the therapeutic benefit. In recent studies, labeling MSCs with reporter genes and the use of corresponding optical imaging techniques provide a noninvasive method for tracking and quantifying the fate of administered MSCs *in vivo*.[160,161] Several different methods to label stem cells with exogenous probes including quantum dots (QDs),[162,163] magnetic nanopartciles,[164,165] carbon nanotubes,[166] and silicon nanoparticles[167] have also been developed for in vivo stem cell tracking via various imaging modalities such as optical imaging, magnetic resonance imaging (MRI), and radionucleotide based imaging.[168,169] However, due to the intrinsic limits of current imaging techniques and tracking probes, the accurate detection of small numbers of cells, as well as the remote control homing of stem cells translocation after *in vivo* transplantation, remains challenging in stem cell research.

One alternative approach to these established techniques is photoacoustic (PA) imaging. The light absorbed and converted to an outgoing thermoacoustic wave can be detected by an ultrasound transducer and used to reconstruct images. PA imaging is used tangentially with normal backscatter mode (B-mode) ultrasound and much suitable for stem cell implantation because B-mode ultrasound has been already used to localize the delivery catheter near the diseased site. Furthermore, PA imaging is noninvasive and can quantitate the implanted cells in real time to confirm that an adequate number of cells reach the treatment site. Key factors for photoacoustic imaging efficiency on how many incident photons can be absorbed and converted to heat, and how fast generated heat can diffuse out from the target during thermoelastic expansion and wave generation. PA imaging may use either endogenous contrast such as oxy- and deoxy-hemoglobin or exogenous contrast agents such as small molecules, carbon nanotubes, or gold nanorods (GNRs). However, the contrast agents show poor biocompatibility and thermal stability, result in the poor imaging signals, limiting the applications.

In this report, we designed a new dual imaging nanostructure, i.e., mesoporous silica nanobeads tagged iron oxides nanoparticles, where the nanoporosity was further filled with gold nanorods, giving a multifunctional nanoprobe that can be controlled by external magnetic navigation, capable of performing MR and photoacoustic imaging modalities simultaneously. This multifunctional nanoprobe was fabricated using a facile, step-wise procedure, including (1) functionalizing mesoporous silica nanoparticles with 3-aminopropyltrimethoxy silane, (2) tagging iron oxide NPs in the cavity of porous silica, (3) seeding and growing of gold nanorods from within the nanoporosity over optimal dimension for PA imaging. From experimental observations, this multifunctional nanoprobe provides exceptionally highly photothermal stability in the meantime, its magnetically controllable nature and dual contrast modality offer great advantages for carrying/homing stem cell, therapeutic delivery and real-time detection/diagnosis.

7.2 Experimental section

Synthesis of porous silica nanobeads (NBs): Cetyltrimethylammonium bromide (CTAB, 300 mg) was dissolved in a mixture of octane (45 mL) and distilled water (96 mL) at 70°C. After stirred magnetically for 20 min, styrene monomer (8.5mL), lysine (66 mg), tetraethylorthosilicate (TEOS, 3000 mg), and AIBA (115 mg) were subsequently added to the system and stirred magnetically for 4 h. After 4 h, the heating was stopped and the suspension was cooled naturally to room temperature. The products were collected by centrifugation at 6000 rpm for 10 min and then washed 3 times with an excess of pure methanol. The template was completely removed by heat treatment at 600°C under atmospheric conditions.

Preparation of Fe_3O_4 magnetic nanoparticles (MNPs): Magnetic nanoparticles Fe_3O_4 were prepared by hydrothermal coprecipitation of ferric and ferrous ions using NaOH as base as described by Kouassi et al.. In brief, iron (II) chloride and iron (III) chloride (1:2) were dissolved in DI water at the concentration of 0.25 M iron ions. The dispersion was stirred at room temperature (25°C) for 1 h and was chemically precipitated by adding 1M of NaOH to keep the pH constant at 10. Product was collected by centrifugation at 7000 rpm for 10 min and washed with ethanol until neutral pH.

Synthesis of magnetic porous silica nanobeads (MNBs): 1ml magnetic nanoparticles

(100 μg/mL) mixed with 1mM porous silica nanobeads and stirred magnetically for 8 h. After incorporation of Fe_3O_4 into silica nanobeads, the products were collected by centrifugation at 10000 rpm for 10 min and then were redispersed into distilled water (1 mL).

Templated synthesis of gold nanorods filled magnetic porous silica nanobeads (GRMNBs): CTAB solution (5 mL, 0.20 M) was mixed with 5.0 mL of $HAuCl_4$ (0.0005M). To the stirred solution, 0.60 mL of ice-cold 0.010 M $NaBH_4$ was added, which resulted in the formation of a brownish yellow solution. Vigorous stirring of the seed solution was continued for 2 hours. Furthermore, incorporation of gold seeds was achieved by swelling 1 mL magnetic porous silica beads with 1 mL seed solution and stirred magnetically for 2 h. For the gold nanorods growth, the growth solution included that CTAB (5 mL, 0.10 M), $AgNO_3$ (0.1 mL, 0.01M), $HAuCl_4$ (0.5 mL, 0.01 M) and ascorbic acid (55 μL, 0.1 M) was added to DI water step-by-step. Finally, the 20 μL of the seed solution (incorporation of gold seeds with magnetic silica nanobeads) was added to the growth solution at 27-30 °C. The color of the solution gradually changed within 10-20 min. The temperature of the growth medium was kept constant at 27-30 °C in all the experiments and stirred magnetically for 24 h. The final products were collected by centrifugation at 10000 rpm for 10 min and then redispersed into distilled water (5 ml).

7.3 Preparation of magnetic gold-containing silica nanobeads (GRMNBs)

The synthetic procedure of the magnetic gold-containing silica nanobeads (GRMNBs) is schematically illustrated in **Figure 7.1.** The 3-aminopropyltrimethoxy silane-functionalized mesoporous silica nanobeads were first synthesized using organic template method. The morphology and particle size of the resulting nanobeads were analyzed by transmission electron microscopy (TEM), as shown in **Figure 7.2a**, respectively. Nearly monodispersed spherical porous nanobeads with an average size of 130 nm in diameter were observed. For the tagging process, the *meso*-2,3-dimercaptosuccinic acid functionalized iron oxide nanoparticles (DMSA-Fe_3O_4 NPs) were chemically anchored *via* hydrophilic interactions (or van der Waals interactions), which the amino groups of silica nanobeads and thiol groups of iron oxide NPs were intermolecularly inserted to form a stable, interdigitated configuration. **Figure 7.2b** indicates the nanobeads decorated with iron oxide NPs (black dots) in the TEM images. Next, for the gold seeding process, as well known that the gold species including $AuCl_4^-$ and metallic gold have a high affinity to amino groups due to electrostatic and coordinate interactions. Such a selective modification toward the nanoporosity of the silica nanobeads with amino group allows a subsequent seeding, retention, and growth of gold nanorods to be more technically feasible. Furthermore, the key in the growth step of gold seeds is to maintain a low reaction rate and minimize self-nucleation events such as using a weaker reducing agent (ascorbic acid) to replace an intense reductant ($NaBH_4$). To further slow down the growth rate of gold nanoparticles is by adding potassium iodide (KI), a coordinating ligand, which reacted with $AuCl_4^-$ forming a stable complex AuI_4^- with a strong Au-I affinity. An additional capping ligand, typically polyvinylpyrrolidone (PVP), was also introduced to stabilize the atomic monomer species and delay self-nucleation. After the seed-carrying magnetic nanobeads were immersed into the gold-containing solution, the formation of gold seeds occurred as evidenced by the color change of the mixture, forming the magnetic silica nanobeads with gold nanorods evolved within the nanoporosity, (**Figure 7.2c and 7.2d**). A Brunauer-Emmett-Teller (BET) analysis also shows a considerable reduction of surface area and average pore size from 789.54 m^2g^{-1} and 6.3 nm (radius) to 106.72 m^2g^{-1} and 2.1 nm (**Figure 7.3**), which supported that the nanoporosity of the silica nanobeads was extensively filled with the iron oxide NPs and gold nanorods.

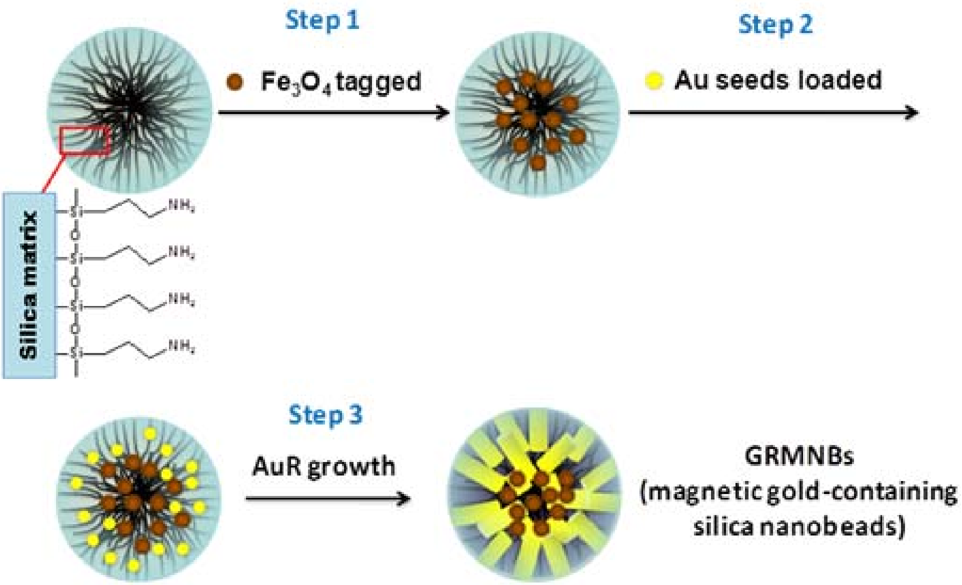

Figure 7.1 Schematic illustration of the synthesis and structure of the magnetic mesoporous silica nanobeads filled with gold nanorods structure (GRMNBs).

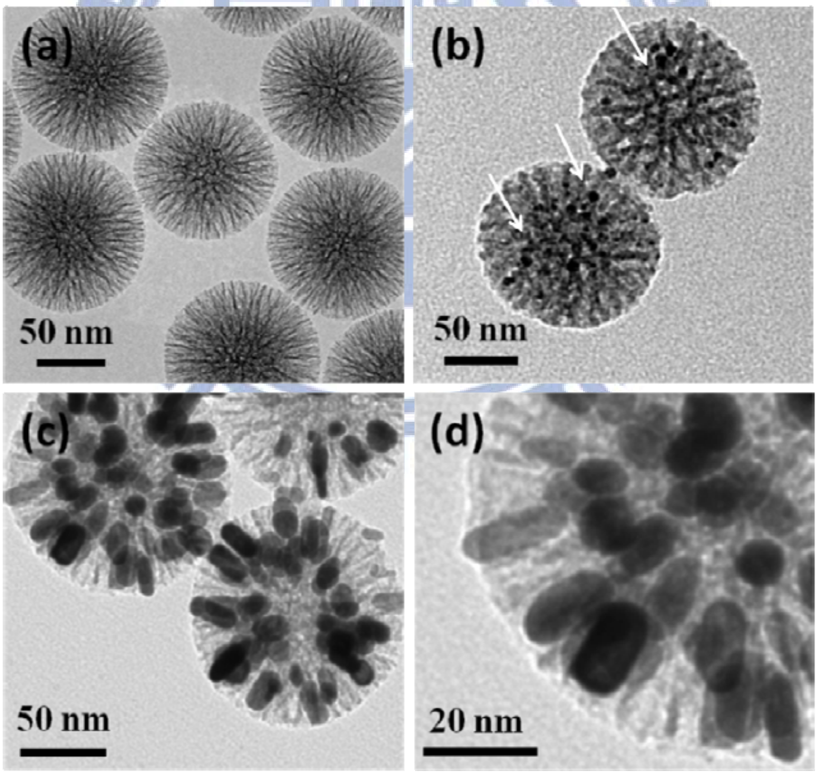

Figure 7.2 (a) TEM image of porous nanobeads. (b) TEM image of the tagged iron oxide nanoparticles inside silica nanobeads (MNBs). (c) TEM image of magnetic mesoporous silica nanobeads filled with gold nanorods structure (GRMNBs). (d) High resolution TEM image of magnetic mesoporous silica nanobeads filled with gold nanorods structure.

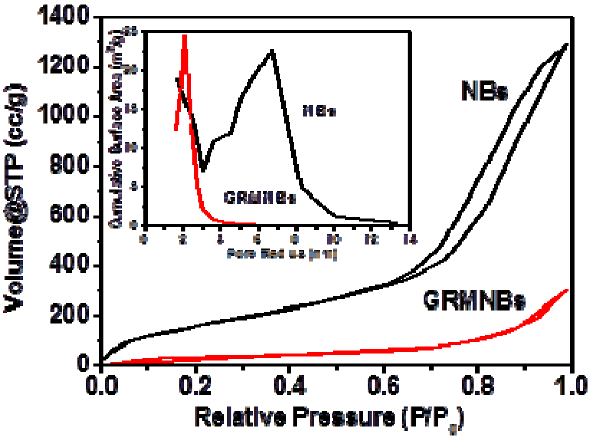

	Surface area (m²/g)	Pore volume (cc/g)	Pore radius (nm)
NBs	789.54	1.821	6.3
GRMNBs	106.72	0.326	2.1

Figure 7.3 The N_2 adsorption/desorption isotherms of the nanobeads with Brunauer-Emmett-Teller (BET). The inset showed that the Barret-Joiner-Halenda (BJH) analysis of the nanobeads and GRMNBs.

7.4 Characteristic and thermal stability of GRMNBs

A typical UV-Vis extinction spectrum of silica nanobeads (NBs), magnetic silica nanobeads (MNBs) and magnetic gold-containing silica nanobeads (GRMNBs) is shown in **Figure 7.4a**. As expected, it showed highly absorption at short wavelength (before 600 nm) for MNBs and slightly absorption for NBs. However, there are no obviously absorptions both in NBs and MNBs after 600 nm. On the contrary, for the GRMNBs, the UV-Vis spectrum has two extinction bands at 525nm (transversal; polarization perpendicular to the long axis) and at ~810 nm (longitudinal; polarization to the long axis). Since the longitudinal plasmonic peak is a good indicator for the shape change of the nanorods, the thermal stability of both gold nanorods and GRMNBs under nanosecond pulsed laser exposure can then be optically characterized by UV-Vis extinction spectroscopy. After irradiating the gold nanorods and GRMNBs solutions with 200 laser pulses at various fluences, the spectral peak changes in shape for all cases (**Figure 7.4b and 7.4c**). The fluences below 4 mJ/cm^2 induced a nearly

60% reduction in amplitude for the gold nanorods after 200 laser pulses, while about only 10% reduction was observed for GRMNBs. Further increasing the number of laser pulses led to a dramatic decrease of the amplitude, a strong shift of the longitudinal peak and a strong increase of the absorption over 600-700 nm region were detected, which are consistent with a rounding of the gold nanorods. In contrast, the porous silica matrix introduced a stabilizing effect onto the gold nanorods. Although the fluences 20 mJ/cm^2 laser pulses the peak only slightly decreased, no shoulder in the 600-700 nm region was evolved. Therefore, it is clear that the gold nanorods physically confined within the porous silica nanobeads were stabilized from structural collapse, ensuring high and stable emitting efficiency, suggesting that the newly-synthesized GRMNBs can be a promising contrast substance for photoacoustic imaging application.

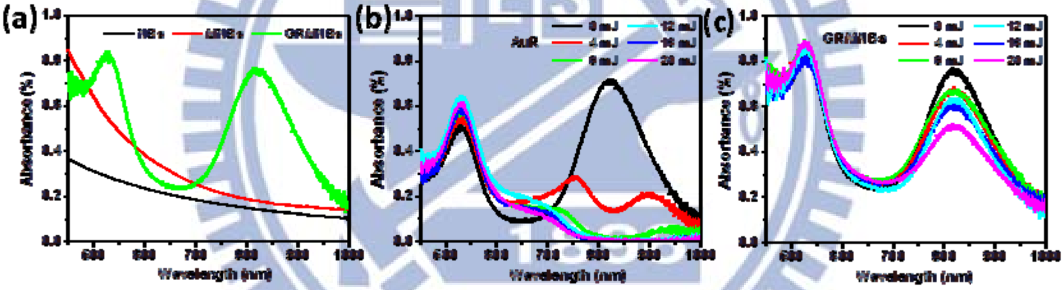

Figure 7.4 (a) Extinction spectra of NBs, MNBs and GRMNBs. Measured UV-Vis extinction spectra of (b) pure AuR and (c) GRMNBs before and after irradiation with various laser fluences.

7.5 Magnetic properties of GRMNBs

The magnetic property of iron oxides nanoparticles (Fe_3O_4 NPs), magnetic silica nanobeads (MNBs) and magnetic gold-containing silica nanobeads (GRMNBs) was estimated by SQUID at 298K with the magnetic field sweeping from -10000 to +10000 G. **Figure 7.5a** shows the correlation of the magnetization with the magnetic field for the Fe_3O_4 NPs, MNBs and GRMNBs where the curves show similar shape with negligible hysteresis. The presence of mesoporous silica nanobeads and gold nanorods dilutes the concentration of Fe_3O_4

nanoparticles, resulting in a lower saturation magnetization (*Ms*) of MNBs and GRMNBs than that of the pure Fe_3O_4 NPs. The magnetic properties of MNBs and GRMNBs were also tested by applying a magnet near the cuvette, where the MNBs and GRMNBs were completely accumulated to the side of the cuvette nearest to the magnet, as illustrated in **Figure 7.5a**. The superparamagnetic characteristics of the Fe_3O_4 NPs accelerate the transverse relation of water protons, and the GRMNBs could be used as a T_2 contrast agent in MR imaging. The longitudinal (T_1) and transverse (T_2) relaxation times of protons from the dispersion containing GRMNBs are shown in **Figure 7.5b**. The MR signal decreased with the increasing content of GRMNBs, demonstrating the efficiency of the GRMNBs in enhancing the transverse (T_2) proton relaxation process. The efficacy and stability of the GRMNBs as an MR contrast agent was further evaluated by measuring the longitudinal (r_1) and transverse (r_2) relaxivities using an MR scanner. **Figure 7.5c** shows that the r_1 of the GRMNBs was 1.205 $s^{-1}mM^{-1}$Fe, and the r_2 value was 127.89 $s^{-1}mM^{-1}$Fe, which is larger than that reported for mesoporous silica nanoparticles decorated with magnetite nanocrystals (76.2 $s^{-1}mM^{-1}$Fe) [119]. The higher transverse (r_2) relaxivities could be attributed to the silica nanobeads tagged the Fe_3O_4 NPs in the pore forming a well-dispersive and chemical stable condition. Therefore, GRMNBs could perform well as a T_2- type MR contrast enhancement agent for cell or molecular imaging and diagnostic applications.

7.6 *In vitro* and *in vivo* photoacoustic signals of GRMNBs

The photoacoustic (PA) signal produced by GRMNBs is observed to be linearly dependent on the concentration as shown in **Figure 7.6**. Next we investigated the PA imaging contrast and magnetic guide of pure gold nanorods and GRMNBs. A phantom experiment which allowed particle flow through a tube was used as a test platform to verify the enhancement of PA signals, and external magnet was placed beside the tube to examine the influence of magnetic guide (**Figure 7.7a**). Pure gold nanorods did not provide sufficient PA imaging contrast enhancement. On the contrary, the GRMNBs without providing external magnet showed better PA signals than the pure gold nanorods. Furthermore, the GRMNBs showed the significant contrast enhancement for PA signal with the presence of external magnet, and it almost enhanced 7.2 times PA signals compare with pure gold nanorods (**Figure 7.7b and 7.9a**). The PA contrast could be further increased by an external magnet, demonstrating their ability to perform active magnetic guide.

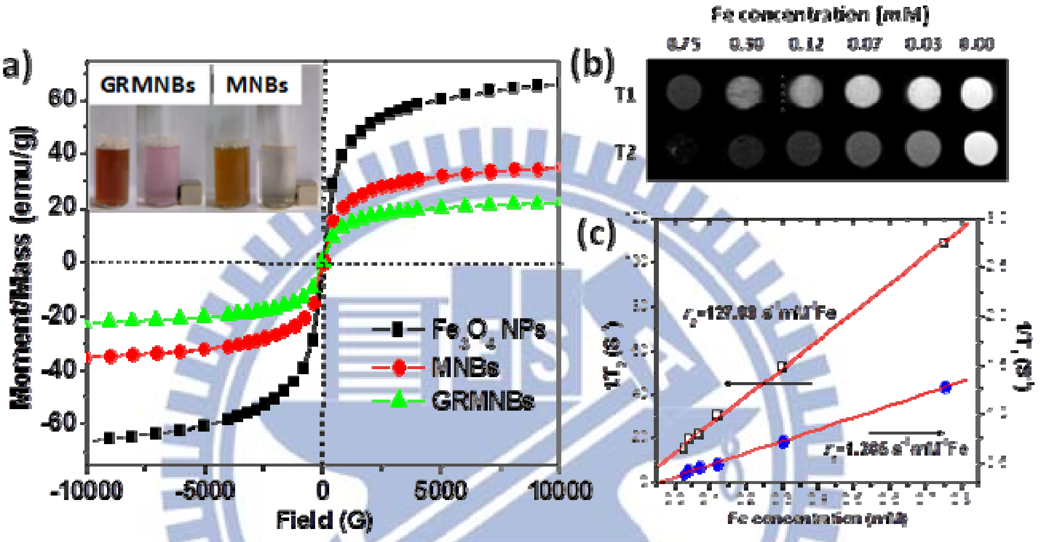

Figure 7.5 (a) Field-dependent magnetization curve of Fe_3O_4 NPs, MNBs and GRMNBs . The inset shows that the MNBs and GRMNBs are attracted by an external magnet. (b) T_1-weighted and T_2-weighted MR images (7.0 T, fast spin-echo sequence: repetition time (TR) = 2500 ms, echo time (TE) = 33 ms) of the aqueous dispersion of MSN@Fe_3O_4 at different Fe concentrations. (c) T_1 and T_2 relaxation rates ($1/T_1$, $1/T_2$) as a function of iron molar concentration obtained at 20°C using a 7.0 T MR scanner.

For *in vivo* measuring the efficiency of the PA signal of GRMNBs with and without an external magnet, the mouse which bore a CT26 tumor (mouse colon cancer) was intravenously injected with GRMNBs solution (200μL, 1mg mL^{-1}). Three-dimensional ultrasound and photoacoustic images of the tumor site and its surrounding are acquired before and up to 12 h after injection (**Figure 7.8a and 7.8b**). In the beginning, we found that mice injected with GRMNBs did not show a sufficiently enhance PA signal in tumor site in the

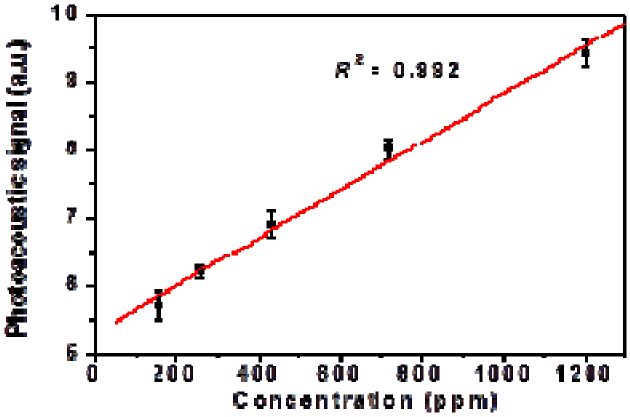

Figure 7.6 The photoacoustic (PA) signal produced by GRMNBs is observed to be linearly dependent on the concentration.

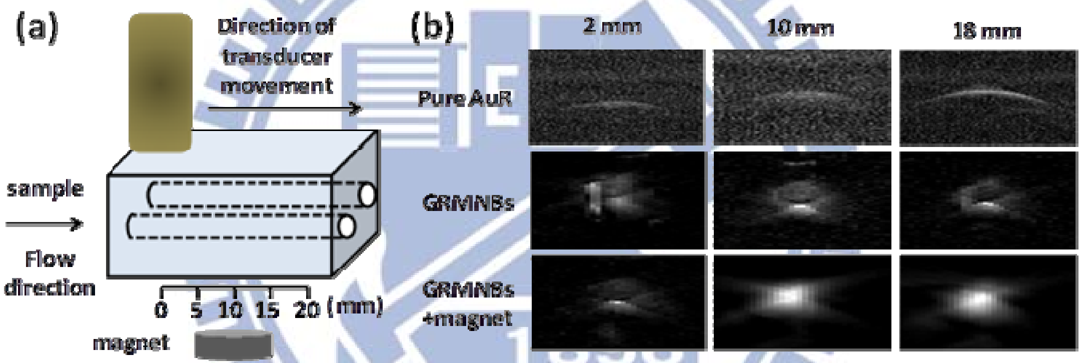

Figure 7.7 (a) Schematic diagram of the magnetic guided experimental set-up for photoacoustic microscopy. (b) PA images in the phantom at different distance of pure AeR, GRMNBs and GRMNBs with an external magnet.

absence of external magnet. However the significant contrast enhancement in PA imaging was observed especially at the magnetic regions when supply the external magnet. Here, three different regions are monitored: edge of the magnet (position 1), central region of the magnet (position 2) and outer regions of the magnet (position 3) (**Figure 7.8c**). As a result, the central region of magnet showed a dramatic enhancement in PA signals, which was contributed as the increase of the localizing concentration of GRMNBs. On the position 1 and 3, the PA signals also increased but less intensive than that in position 2 due to the distance away from the magnet. The images from different time intervals were aligned with one another using simple vertical translations to account for small vertical movements in the transducer positioning. This alignment allowed quantification of the PA signal at all time points using a single region of interest. Then, we calculated a subtraction PA image signal including the PA image taken before injection, the images taken at 12 h post-injection with and without an external magnet. The photoacoustic signal was calculated by drawing a 3D region of interest around the tumor (tumor boundaries were clearly visualized in the ultrasound images). The quantified photoacoustic signal is increased as a function of time as shown in **Figure 7.9b**. At pre-injection, there is no photoacoustic signal in tumor site. Conversely, at the 12 h post-injection without an external magnet, mice injected with GRMNBs showed obviously photoacoustic signals. Furthermore, a 3.5 times increase in PA signaling intensity was

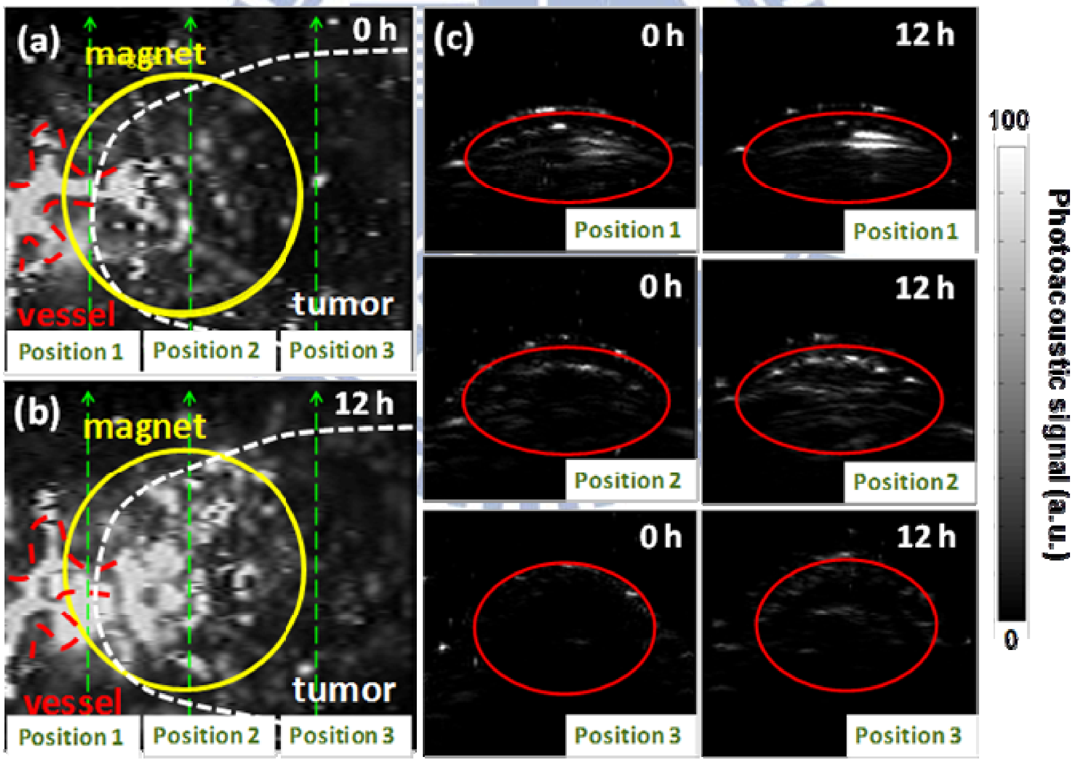

Figure 7.8 (a) PA image of tumor site with pre-injection. (b) Pa images of tumor site with injected GRMNBs for 12 h. (c) PA images of different position slice through the tumor. Subtraction images were calculated as the 12 h post-injection image minus the pre-injection image.

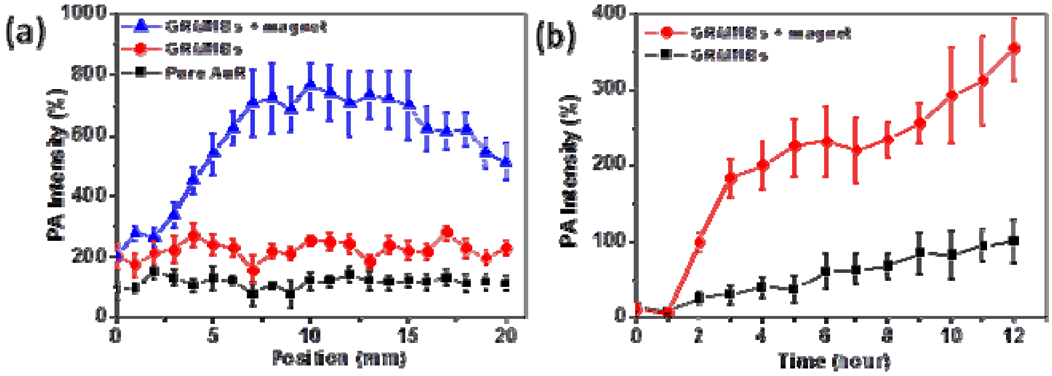

Figure 7.9 (a) PA signal intensity of pure AuR, GRMNBs and GRMNBs with an external magnet at different distances. (b) PA signal intensity of GRMNBs and GRMNBs with an external magnet in 12 h post-injection.

measured for the GRMNBs compared with the case without using the external magnet, which is indicative of a promising contrast agent for photoacoustic imaging modalities with magnetic guide.

7.7 Stem cell uptake

The cellular uptake of the FITC-labeled GRMNBs (green color emitted) was determined by confocal laser scanning microscopy (CLSM). **Figure 7.10a and 7.10b** show that the GRMNBs are gradually internalized after incubating with the human adipose stem cell for 8-h and 24-h durations, respectively. The green fluorescent dye was clearly observed in the region of cytoplasm over the incubation. For an 8-h internal, some nanoprobes appeared to attach to the cell membranes. However, numerous regions of the cytoplasm displayed strong green fluorescent emission at 24 hours. This observation implies that the nanoprobes can be internalized efficiently toward the cells. The fluorescence intensity determined by flow cytometry rapidly increased, even clearly measurable at a 4-h period, indicating an efficient cellular internalization.

As reported, the stem cells need about 2~4 days to migrate toward and spread through the organization.[170] The association persistence between nanoprobes and stem cells is of particular importance during the time course of cell homing. After the GRMNBs was incubated with stem cells for 24 h, the nanoprobes were washed off and the cell were cultured for different additional time periods, i.e., 6, 24 and 48 h, to detect the nanoprobes retention (**Figure 7.10c, 7.10d and 7.10e**). For the GRMNBs, the stem cells showed very strong fluorencence after washing off the unbound nanoprobes, which indicated a prolonged retention of the nanoprobes. With cellular retention time long enough, the nanoprobes could be shipped to the correct position to perform therapy. Several earlier reports have demonstrated that the *in vivo* movement of the cells labeled with magnetic nanoparticles could be manipulated by applying a magnetic field. Here we wondered whether the translocation of GRMNBs-labeled stem cells could be remotely controlled by an external magnet. *In vitro* study revealed that the GRMNBs incubated with stem cells for 24 h and further used trypsin to let GRMNBs-labeled stem cells homogeneously suspending in the DMEM. Then, we put an external magnet under the incubated dish to investigate the variation of the stem cells (**Figure 7.11a**). The GRMNBs-labeled stem cell in the presence of an external magnet could rapidly move toward the magnet within a few minutes. After 8 h, the stem cells adhered to the incubated dish, which showed two different parts (inside the magnet and outside the magnet). Numerous of the GRMNBs-labeled stem cells aggregated and adhered in the inside the magnet parts, on the contrary, there were rarely GRMNBs-labeled stem cells adhered in the outside the magnet parts (**Figure 7.11b**). To this point, the GRMNBs-labeled stem cells were able to reach an “active homing” effect with the magnetic guiding.

7.8 *In vivo* stem cell therapy for MCAO stroke

Inspired by the in vitro results, we nest investigated magnetically induced stem cell translocation *in vivo*. The mouse which was been middle cerebral artery occlusion (MCAO) stroke and set a magnet on the head (**Figure 7.12a and 7.12b**) was intravenously injected

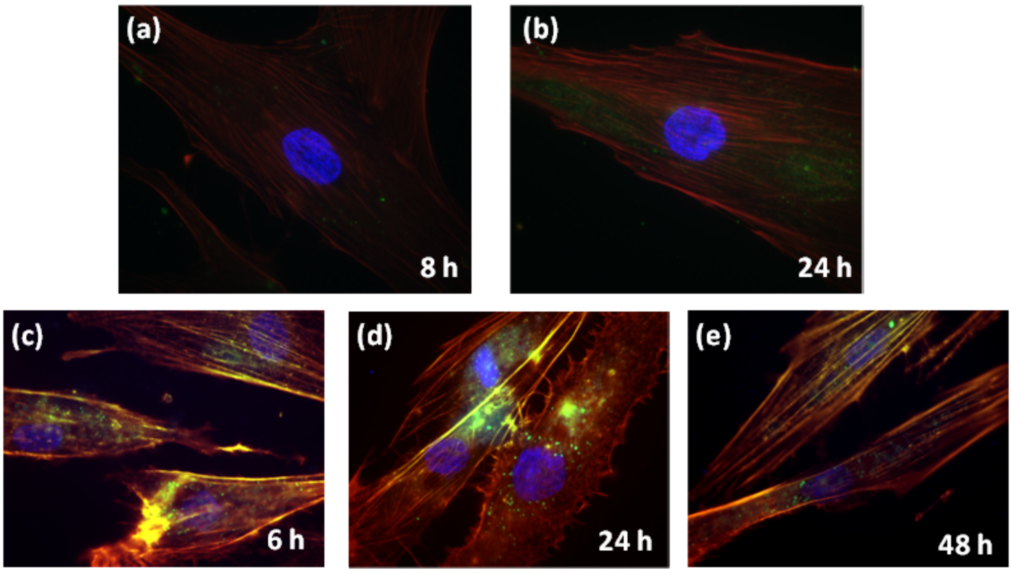

Figure 7.10 Time-course PL microscopy images of human stem cells labeled with FITC-GRMNBs nanoprobes and incubated for (a) 8 hour and (b) 24 hours. Cellular retention of GRMNBs in stem cells cultured for different additional time of (c) 6 h (d) 24 h (e) 48 h. The cell skeleton was stained with rodamin phalloidin (red), and the cell nucleus with DAPI (blue).

with GRMNBs-labeled stem cells solution (200 μL, 1mg mL^{-1} in 2 × 10^{-6} stem cells). As theGRMNBs-labeled stem cells injection, stem cells were guided and homed to the stroke site by the external magnet. After two weeks, we sacrificed the MCAO stroke mouse and brought out the brain tissue (**Figure 7.12 c**). For the MR imaging of brain (**Figure 7.12d**), we found that the mouse injected GRMNBs-labeled stem cells showed a significant increase of darkness signal in the stroke site (right brain) compare with in the normal site (left brain). The MR imaging showed that the darkness signal indicated the GRMNBs-labeled stem cells were truly guided and homed to the stroke site. On average, quantification of the MR signal, the stroke areas (right brain) demonstrated 5.4 times higher intensity in MR signal compared with the normal areas (left brain), which is indicative of a promising magnetic guiding and contrast agent for imaging modalities.

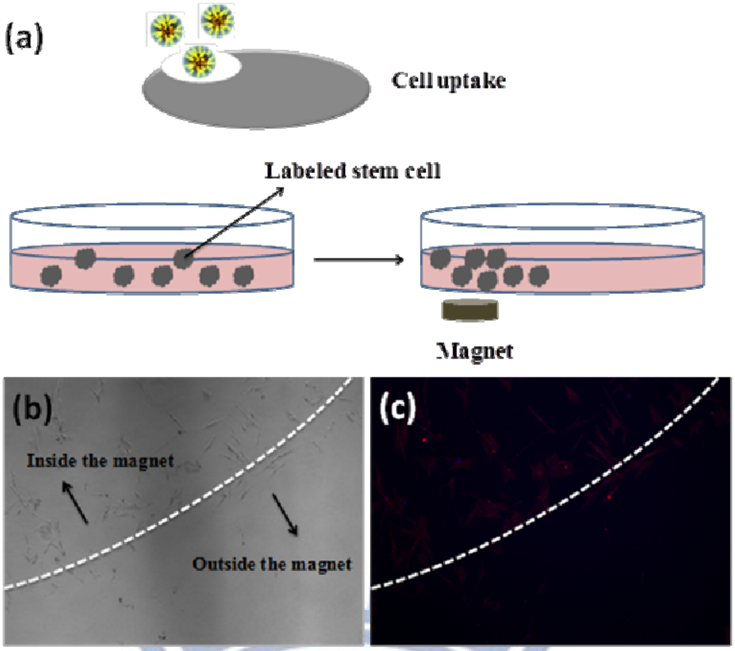

Figure 7.11 (a) Schematic diagram of the magnetic guided experimental set-up under magnetic remote-controlled stem cells. The image of (b) visible microscopy(c) fluorescent microscopy for distribution of stem cells under magnetic remote-controlled.

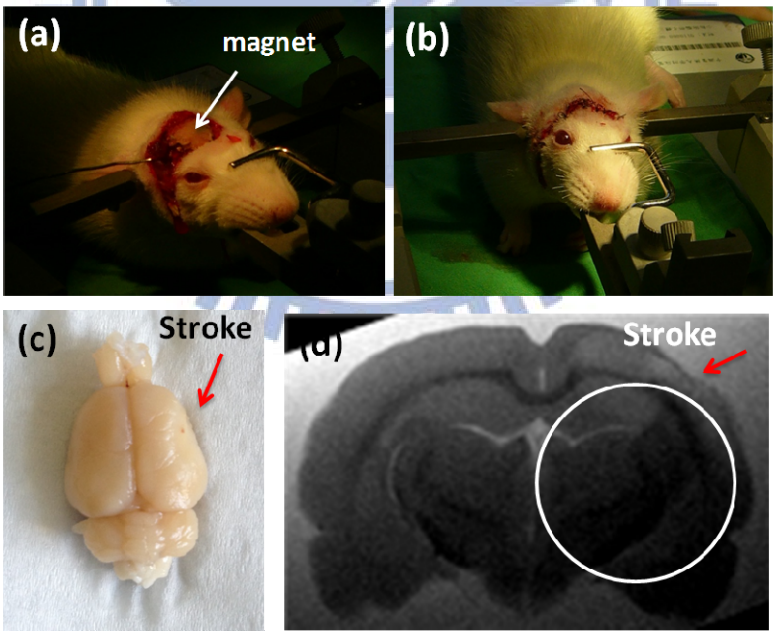

Figure 7.12 (a) (b) the MCAO modal mouse with setting an external magnet on the head. (c) the brain tissue of MCAO modal mouse. (d) MR imaging for the stroke brain.

7.9 Summary

The new dual imaging, MR imaging and photoacoustic imaging, nanostructure where the nanoporosity within uniform mesoporous silica nanobeads tagged iron oxides filled with gold nanorods were successfully developed for stem cell guiding and therapy. The iron oxides were chemically anchored via hydrophilic interactions and internalization and stabilization of gold seeds, further forming the high density, well-dispersive conformal and spectrum-controllable gold nanorods structure. The magnetic nanoprobes showed highly thermal stability after laser pulses and perfect magnetic properties. *In vitro* MR imaging and photoacoustic imaging studies showed a relatively enhancement contrast modality. Furthermore, GRMNBs demonstrated highly cell uptake efficiency and a prolonged retention for 48 hours. In addition, the magnetic nanoprobes were successfully achieved using an external magnet guiding the stem cells to the stroke areas and cell labeling by MR images for *in vivo* MCAO stroke rats. Together with a well-regulated design, the GRMNBs are expected to act as a potential dual-modal imaging contrast modality with improved not only homing stem cells but also nano-imaging tracking for stem cells therapy applications.

Chapter 8

Conclusion

8.1 Removable nanogated lids of Fe_3O_4–capped mesoporous silica nanoparticles

1. Fe_3O_4-capped mesoporous silica nanoparticles (MSN@Fe_3O_4) were successfully developed and displayed a well-dispersed character in an aqueous solution.
2. When CPT drugs was enclosed the deposition of nano-Fe_3O_4 particles to reach a full coverage on the MSN surface, no leakage of the drug from the MSN@Fe_3O_4.
3. Under a magnetic stimulus, the drug eluted in a fast-acting, burst-like profile depending on the time duration of the stimulus.
4. The release profile underlying the stimulus was confirmed to be a result of the removal of the capped Fe_3O_4 nanoparticles from the MSN surface due to the cleavage of the chemical bonds bridging both Fe_3O_4 and MSN.
5. The MSN@Fe_3O_4 nanocarriers showed great potential as probes in MRI and an efficient uptake by A549 cells and also demonstrated an excellent cytocompatibility.

8.2 Geometrical confinement of quantum dots in porous nanobeads

1. Highly biocompatible cRGD-encoded lipid-coated QDs tagged porous nanobeads (cRGD-encoded LQNBs) were successfully developed for cancer targeting and imaging *in vitro* and *in vivo*.
2. The larger pores of the octadecyltrimethoxysilane modified nanobeads facilitated the internalization and stabilization of QDs.
3. The QDs tagged nanobeads showed highly chemical stability and a wide spectrum of multiplex color codings. *In vivo* and *in vitro* imaging studies showed a relatively sharp, stable and distinguishable contrast modality.
4. cRGD-encoded LQNBs demonstrated a technically potential for visualizing the variations

of uptake behavior between MCF-7 and HeLa cells, which may enable a further understanding on cellular behavior on a nanometric-to-molecular scale.

5. In MCF-7 xenograft rude mice, the cRGD-encoded LQNBs also exhibited long lasting signals at the tumor site.

8.3 Gold-nanorod-filled silica nanobeads

1. Highly biocompatible mesoporous silica nanobeads with pores filled with gold nanorods (AuRNBs), showing a nano-seaurchin structure, were successfully developed for cancer treatment and photoacoustic imaging *in vitro* and *in vivo*.
2. The larger pores of the 3-aminopropyltrimethoxy silane modified nanobeads facilitated the internalization and stabilization of gold seeds, further forming the high density, well-dispersive conformal and spectrum-controllable gold nanorods structure.
3. The silica nanobeads with gold nanorods filled structure showed highly thermal stability after laser pulses.
4. *In vivo* and *in vitro* photoacoustic imaging studies showed a relatively enhancement contrast modality. The enhancement could be attributed to changes in the interfacial heat conduction from gold to water due to the silica.
5. AuRNBs demonstrated highly cell uptake efficiency, low toxicity and photothermal therapeutic with exceptionally high heating efficiency.

8.4 Magnetic mesoporous silica nanobeads filled with gold nanorods

1. The new dual imaging, MR imaging and photoacoustic imaging, nanostructure where the nanoporosity within uniform mesoporous silica nanobeads tagged iron oxides filled with gold nanorods were successfully developed for stem cell guiding and therapy.
2. The iron oxides were chemically anchored via hydrophilic interactions and internalization and stabilization of gold seeds, further forming the high density, well-dispersive conformal

and spectrum-controllable gold nanorods structure.

3. The magnetic nanoprobes showed highly thermal stability after laser pulses and perfect magnetic properties. *In vitro* MR imaging and photoacoustic imaging studies showed a relatively enhancement contrast modality.
4. GRMNBs demonstrated highly cell uptake efficiency and a prolonged retention for 48 hours.
5. The magnetic nanoprobes were successfully achieved using an external magnet guiding the stem cells to the stroke areas and cell labeling by MR images for *in vivo* MCAO stroke mouse.

References

[1] V. P. Torchilin , *Mol. Med. Today* **1996** , *2* , 242 .

[2] V. P. Torchilin , *Nat. Rev. Drug Discov.* **2005** , *4* , 145 .

[3] T. K. Jain, M. A Morales, S. K. Sahoo, D. L. Leslie-Pelecky, V. Labhasetwar, *Mol. Pharmaceutics* **2005**, *2*, 194.

[4] T. Isojima, M. Lattuada, J. B. V. Sande, T. A. Hatton, *ACS Nano*. **2008**, *2*, 1799.

[5] Y. W. Won, S. M. Yoon, K. S. Lim, Y. H. Kim, *Adv. Funct. Mater*. **2012**, *22*, 1199.

[6] M. Shao, F. Ning, J. Zhao, M. Wei, D. G. Evans, X. Duan, *J. Am. Chem. Soc.*, **2012**, *134*, 1071.

[7] I. Pastoriza-Santos, J. Perez-Juste, L. M. Liz-Marzan, *Chem. Mater*. **2006**, *18*, 2465.

[8] S. T. Selvan, T. T. Tan, J. Y. Ying, *Adv. Mater*. **2005**, *17*, 1620.

[9] K. R. West, S. Otto, *Current Drug Discovery Technologies*, **2005**, *2*, 123

[10] W. Chen, Y. Shi, H. Feng, M. Du, J. Z. Zhang, J. Hu, D. Yang, *J. Phys. Chem. B* **2012**, *116*, 9231.

[11] I. I. Slowing, B. G. Trewyn, S. Giri , V. S. Y. Lin, *Adv. Funct. Mater.* **2007** , *17* , 1225.

[12] B. G. Trewyn, Slowing II, S. Giri, H. T. Chen, V. S. Y. Lin, *Acc. Chem.Res.* **2007**, *40* , 846.

[13] F. Torney, B. Trewyn, V. S. Y. Lin, K. Wang, *Nature Nanotechnol* **2007**, *2*, 295.

[14] Y. S. Lin, S. H. Wu, Y. Hung, Y. H. Chou, C. Chang, M. L. Lin, C. P. Tsai, C. Y. Mou, *Chem. Mater.* **2006,** *18,* 5170.

[15] Y. Zhao, L. N. Lin, Y. Lu, S. F. Chen, L. Dong, S. H. Yu, *Adv. Mater*. **2010**, *22*, 5255.

[16] B. Munoz, A. Ramila, J. Perez-Pariente, I. Diaz, M. Vallet-Regi, *Chem. Mater*. **2003**, *15*, 500.

[17] J. Lu, M. Liong, J. I. Zink, F. Tamanoi, *Small* **2007**, *3*, 1341.

[18] P. Horcajada, A. Ramila, J. Perez-Pariente, M. Vallet-Regi, *Microporous and Mesoporous Materials* **2004**, *68*, 105.

[19] Y. Piao, A. Burns, J. Kim, U. Wiesner, T. Hyeon, *Adv. Funct. Mater.***2008** , *18* , 3745.

[20] J. Cheon, J. H. Lee, *Acc. Chem. Res.* **2008**, *41* , 1630.

[21] H. Zeng, S. Sun, *Adv. Funct. Mater.* **2007**, *18* , 391.

[22] S. A. Corr, Y. P. Rakovich, Y. K. Gunko, *Nanoscale Res. Lett.* **2008**, *3*, 87.

[23] R. W. Storrs, F. D. Tropper, H. Y. Li, C. K. Song, J. K. Kuniyoshi, D. A. Sipkins, K. C. P. Li, M. D. Bednarski, *J. Am. Chem. Soc.* **1995**,*117* , 7301 .

[24] D. A. Sipkins, D. A. Cheresh, M. R. Kazemi, L. M. Nevin, M. D. Bednarski, K. C. P. Li, *Nat. Med.* **1998**, *4*, 623.

[25] T. K. Jain, J. Richey, M. Strand, D. L. Leslie-Pelecky, C. A. Flask, V. Labhasetwar, *Biomaterials* **2008**, *29*, 4012.

[26] L. O. Cinteza, T. Y. Ohulchanskyy, Y. Sahoo, E. J. Bergey, R. K. Pandey, P. N. Prasad, *Mol. Pharmaceutics* **2006**, *3*, 415.

[27] G. H. Wu, A. Milkhailovsky, H. A. Khant, C. Fu , W. Chiu, J. A. Zasadzinski, *J. Am. Chem. Soc.* **2008**, *130*, 8175.

[28] D. V. Volodkin, A. G. Skirtach, H. Mohwald, *Angew. Chem. Int. Ed.* **2009**, *48*, 1807.

[29] P. Zou, Y. Yu, Y. A. Wang, Y. Zhong, A. Welton, C. Galban, S. Wang, D. Sun, *Mol. Pharmaceutics* **2010**, *6*, 1974.

[30] W. Wang, D. Cheng, F. Gong, X. Miao, X. Shuai, *Adv. Mater.* **2012**, *24*, 115.

[31] I. Gorelikov, N. Matsuura, *Nano Lett.* **2008**, *8*, 369.

[32] Q. Zhan, J. Qian, X. Li, S. He, *Nanotechnology* **2010**, *21*, 55704.

[33] T. Zhao, H. Wu, S. Q. Yao, Q. H. Xu, G. Q. Xu, *Langmuir* **2010**, *26*, 14937.

[34] S. S. Feng, L. Mu, K. Y. Win, G. F. Huang, *Curr. Med. Chem.* **2004**, *11*, 413.

[35] H. S. Yoo, K. H. Lee, J. E. Oh, T. G. Park, *J. Controlled Release* **2000**, *68*, 419.

[36] L. Li, F. Tang, H. Liu, T. Liu, N. Hao, D. Chen, X. Teng, J. He, *ACS Nano* **2010**, *4*, 6874.

[37] Y. Hu, X. T. Zheng, J. S. Chen, M. Zhou, C. M. Li, X. W. D. Lou, *J. Mater. Chem.* **2011**, *21*, 8052.

[38] L. Li, Y. Guan, H. Liu, N. Hao, T. Liu, X. Meng, C. Fu, Y. Li, Q. Qu, Y. Zhang, S. Ji, L. Chen, D. Chen, F. Tang, *ACS Nano* **2011**, *9*, 7462.

[39] F. Hoffmann, M. Cornelius, J. Morell, Mi. Froba, *Angew. Chem. Int. Ed.* **2006**, *45*, 3216.

[40] G. S. Attard, J. C. Glyde, C. G. G. Vltner, *Nature* **1995**, *378*, 366.

[41] B. Smarsly, S. Polarz, M. Antonietti, *J. Phys. Chem. B* **2001**, *105*, 10473.

[42] K. M. Ryan, N. B. Coleman, D. M. Lyons, J. P. Hanrahan, T. R. Spalding, M. A. Morris, D. C. Steytler, R. K. Heenan, J. D. Holmes, *Langmuir* **2002**, *18*, 4996.

[43] A. B. D. Nandiyanto, S. G. Kim, F. Iskandar, K. Okuyama, *Microporous and Mesoporous Materials* **2009**, *120*, 447.

[44] M. Vallet-Regi, A. Ramila, R. P. del Real, J. Perez-Pariente, *Chem. Mater.* **2001**, *13*, 308.

[45] B. Munoz, A. Ramila, J. Perez-Pariente, I. Diaz, M. Vallet-Regi, *Chem. Mater.* **2003**, *15*, 500.

[46] C. Y. Lai, B. G. Trewyn, D. M. Jeftinija, K. Jeftinija, S. Xu, S. Jeftinija, V. S. Y. Lin, *J. Am. Chem. Soc.* **2003**, *125*, 4451.

[47] C. Park, H. Kim, S. Kim, C. Kim, *J. Am. Chem. Soc.* **2009**, *131*, 16614.

[48] S. E. Skrabalak, J. Chen, L. Au, X. Lu, X. Li, Y. Xia, *Adv. Mater.* **2007**, *19*, 3177.

[49] S. Lal, S. E. Clare, N. J. Halas, *Acc. Chem. Res.* **2008**, *41*, 1842.

[50] P. K. Jain, X. Huang, I. H. El-Sayed, M. A. El-Sayed, *Acc. Chem. Res.* **2008**, *41*, 1578.

[51] J. Turkevich, P. C. Stevenson, J. Hillier, *Discuss. Faraday Soc.* **1951**, *11*, 55.

[52] G. Frens, *Nature* **1973**, *241*, 20.

[53] C. M. Cobley, J. Chen, E. C. Cho, L. V. Wang, Y. Xia, *Chem. Soc. Rev.* **2011**, *40*, 44.

[54] A. A. Karabutov, N. B. Podymova, V. S. Letokhov, *Appl. Phys. B-Lasers Opt.* **1996**, *63*, 545.

[55] M. Xu, L. V. Wang, *Review of Scientific Instruments* **2006**, *77*, 041101.

[56] L. V. Wang, *IEEE J. Sel. Topics Quantum Electron*. **2008**, *14*, 171.

[57] G. D. Moon, S. W. Choi, X. Cai, W. Li, E. C. Cho, U. Jeong, L. V. Wang, Y. Xia, *J. Am. Chem. Soc.* **2011**, *133*, 4762.

[58] Y. S. Chen, W. Frey, S. Kim, P. Kruizinga, K. Homan, S. Emelianov, *Nano Lett.* **2011**, *11*, 348.

[59] H. Liu, T. Liu, X. Wu, L. Li, L. Tan, D. Chen, F. Tang, *Adv. Mater*. **2012**, *24*, 755.

[60] M. Arruebo, R. Fernandez-Pacheco, M. R. Ibarra, J. Santamaria, *NanoToday* **2007**, *2*, 22.

[61] D. L. J. Thorek, A. Chen, J. Czupryna, A. Tsourkas, *Ann Biomed Eng* **2006**, *34*, 23.

[62] C. H. Griffiths, M. P. Ohoro, T. W. Smith, *J. Appl. Phys.* **1979**, *50*,7108.

[63] C. B. Murray, D. J. Norris, M. G. Bawendi, *J. Am. Chem. Soc.* **1993**, *115*, 8706.

[64] Z. A. Peng, X. G. Peng, *J. Am. Chem. Soc.***2001**, *123*, 183.

[65] T. Hyeon, S. S. Lee, J. Park, Y. Chung, N. Bin, H. Na, *J. Am. Chem. Soc.* **2001**, *123*, 12798.

[66] J. Park, K. An, Y. Hwang, J. G. Park, H. J. Noh, J. Y. Kim, J. H. Park, N. M. Hwang, T. Hyeon, *Nature Materials* **2004**, *3*, 891.

[67] S. G. Kwon, Y. Piao, J. Park, S. Angappane, Y. Jo, *J. Am. Chem. Soc.* **2007**, *129*, 12571.

[68] R.Weissleder, A. S. Lee, A. J. Fishman, P. Reimer, T. Shen, R. Wilkinson, R. J. Callahan, T. J. Brady, *Radiology* **1991**, *181*, 245.

[69] J. W. M. Bulte, D. L. Kraitchman, *NMR Biomed*. **2004**, *17*, 484.

[70] Y. X. J. Wang, S. M. Hussain, G. P. Krestin, *Eur.J. Radiol*. **2001**, *11*, 2319.

[71] M. F. Bellin, *Eur.J. Radiol*. **2006**, *60*, 314.

[72] R. Weissleder, A. Moore, U. Mahmood, R. Bhorade, H. Benveniste, E. A. Chiocca, J. P. Basilion, *Nat. Med*. **2000**, *6*, 351.

[73] M. Zhao, D. A. Beauregarf, L. Loizou, B. Davletov, K. M. Brindle, *Nat. Med*. **2001**, *7*, 1241.

[74] J. Rockenberger, E. C. Sher, A. P. Alivisatos, *J. Am. Chem. Soc.* **1999**, *121*, 11595.

[75] S. H. Sun, H. Zeng, D. B. Robinson, S. Raoux, P. M. Rice, S. X. Wang, G. X. Li, *J. Am. Chem. Soc.* **2004**, *126*, 273.

[76] N. R. Jana, Y. Chen. X. Peng, *Chem. Mater.* **2004**, *16*, 3931.

[77] W. S. Seo, J. H. Lee, X. Sun, Y. Suzuki, D. Mann, Z. Liu, M. Terashima, P. C. Yang, M. V. McConnell, D. G. Nishimura, H. Dai, *Nat. Mater.* **2006**, *5*, 971.

[78] J. H. Lee, Y. M. Huh, Y. W. Jun, W. Seo, J. T Jane, H. T. Song, S. Kim, E. J. Cho, H. G. Yoon, J. S. Suh, J. Cheon, *Nat Med*. **2007**, *13*, 95.

[79] Y. M. Huh, Y. Jun, H. T. Song, S. J. Kim, J. S. Choi, J. H. Lee, S. Yoon, K. S. Kim, J. S. Shin, J. S. Suh, J. Cheon, *J. Am. Chem. Soc.* **2005**, *127*, 12387.

[80] H. T. Song, J. S. Choi, Y. M. Huh, S. Kim, Y. W. Jun, J. S. Suh, J. Cheon, *J. Am. Chem. Soc.* **2005**, *127*, 9992.

[81] Y. W. Jun, Y. M. Huh, J. S. Choi, J. H. Lee, H. T. Song, S. Kim, S. Yoon, K. S. Kim, J. S. Shin, J. S. Suh, J. Cheon, *J. Am. Chem. Soc.* **2005**, *127*, 5732.

[82] J. H. Lee, Y. W. Jun, S. I. Yeon, J. S. Shin, J. Cheon, *Angew. Chem. Int. Ed.* **2006**, *45*, 8160.

[83] B. M. Seo, M. Miura, S. Gronthos, P. M. Bartold, S. Batouli, J. Brahim, *Lancet* **2004**, *364*, 149.

[84] F. M. Chen, Y. P. Jin, *Tissue Eng Part B Rev.* **2010**, *16*, 219.

[85] E. Bible, D. Y. Chau, M. R. Alexander, J. Price, K. M. Shakesheff, M. Modo, *Nat Protoc* **2009**, *4*, 1440.

[86] L. Cheng, C. Wang, X. Ma, Q. Wang, Y. Cheng, H. Wang, Y. Li, Z. Liu, *Adv. Funct. Mater*. **2013**, *23*, 272.

[87] L. Li, Y. Guan, H. Liu, N. Hao, T. Liu, X. Meng, C. Fu, Y. Li, Q. Qu, Y. Zhang, S. Ji, L. Chen, D. Chen, F. Tang, *ACS Nano* **2011**, *5*, 7462.

[88] Z. Hu, X. Xia, *Adv. Mater.* **2004**, *16*, 305.

[89] X. Z. Zhang, D. Q. Wu, C. C. Chu, *Biomaterials* **2004**, *25*, 3793.

[90] M. Das, S. Mardyani, W. C. W. Chan, E. Kumacheva, *Adv. Mater.* **2006**, *18*, 80.

[91] V. Cauda, C. Argyo, A. Schlossbauer, T. Bein, *J. Mater. Chem.* **2010**, *20*, 4305.

[92] M. R. Abidian, D. H. Kim, D. C. Martin, *Adv. Mater.* **2006**, *18*, 405.

[93] B. G. De Geest, A. G. Skirtach, A. A.Mamedov, A. A. Antipov, N. A. Kotov, S. C. De Smedt, G. B. Sukhorukov**,** *Small* **2007**, *3*, 804.

[94] H. J. Kim, H. Matsuda, H. Zhou, I. Honma**,** *Adv. Mater.* **2006**, *18*, 3083.

[95] Y. Jin, X. Gao, *Nature Nanotechnology* **2009**, *4*, 571.

[96] J. L. V. Escoto, I. I. Slowing, C. W. Wu, V. S. Y. Lin, *J. Am. Chem. Soc.* **2009**, *131*, 3462.

[97] C. Liu, J. Guo, W. Yang, J. Hu, C. Wang, S. Fu, *J. Mater. Chem.* **2009**, *19*, 4764.

[98] S. H. Hu, K. T. Kuo, D. M. Liu, S. Y. Chen, *Adv. Func. Mater.* **2009**, *19*, 3396.

[99] S. H. Hu, S. Y. Chen, C. S. Hsiao, D. M. Liu, *Adv. Mater.* **2008**, *20*, 2690.

[100] W. C. Huang, S. H. Hu, K. H. Liu, S. Y. Chen, D. M. Liu, *J. Control. Release* **2009**, *139*, 221.

[101] S. H. Hu, D. M. Liu, W. L. Tung, C. F. Liao, S. Y. Chen, *Adv. Func. Mater.* **2008**, *18*, 2946.

[102] T. J. Yoon, J. S. Kim, B. G. Kim, K. N. Yu, M. H. Cho, J. K. Lee, *Angew. Chem. Int. Ed.*

2005, *44*, 1068.

[103] R. J. Mannix, S. Kumar, F. Cassiola, M. Montoya-Zavala, E. Feinstein, M. Prentiss, D. E. Ingber, *Nature Nanotechnology* **2008**, *3*, 36.

[104] I. Koh, X. Wang, B. Varughese, L. Isaacs, S. H. Ehrman, D. S. English, *J. Phys. Chem. B* **2006**, *110*, 1553.

[105] Z. Teng, J. Li, F. Yan, R. Zhao, W. Yang, *J. Mater. Chem.* **2009**, *19*, 1811.

[106] G. H. Gao, G. H. Im, M. S. Kim, J. W. Lee, J. Yang, H. Jeon, J. H. Lee, D. S. Lee. *Small.* **2010**, *6*, 1201.

[107] W. S. Seo, J. H. Lee, X. Sun, Y. Suzuki, D. Mann, Z. Liu, M. Terashima, P. C. Yang, M. V. Mcconnell, D. G. Nishimura, H. Dai1, *Nature Materials* **2006**, *5*, 971.

[108] O. Veiseh, C. Sun, J. Gunn, N. Kohler, P. Gabikian, D. Lee, N. Bhattarai, R. Ellenbogen, R. Sze, A. Hallahan, J. Olson, M. Zhang, *Nano Lett.* **2006**, *5*, 1003.

[109] L. Chen, G. Zhu, D. Zhang, H. Zhao, M. Guo, W. Shib, S. Qiu, *J. Mater. Chem.* **2009**, *19*, 2013.

[110] A. K. Gupta, M. Gupta, *Biomaterials* **2005**, *26*, 3995.

[111] L. Li, T. L. M. ten Hagen, D. Schipper, T. M. Wijnberg, G. C. van Rhoon, A. M.M. Eggermont, L. H. Lindner, G. A. Koning, *J. Control. Release* **2010**, *143*, 274.

[112] P. Drake, H. J. Cho, P. S. Shih, C. H. Kao, K. F. Lee, C.H. Kuo, X. Z. Linb, Y. J. Lin, *J. Mater. Chem.* **2007**, *17*, 4914.

[113] N. Nasongkla, E. Bey, J. Ren, H. Ai, C. Khemtong, J. S. Guthi, S. F. Chin, A. D. Sherry, D. A. Boothman, J. Gao, *Nano Lett.* **2006**, *6*, 2427.

[114] J. Kim, Y. Piao, T. Hyeon, *Chem. Soc. Rev.* **2009**, *38*, 372.

[115] J. Kim, J. E. Lee, S. H. Lee, J. H. Yu, J. H. Lee, T. G. Park, T. Hyeon**,** *Adv. Mater.* **2008**, *20*, 478.

[116] J. L. Bridot, A. C. Faure, S. Laurent, C. Riviere, C. Billotey, B. Hiba, M. Janier, V. Josserand, J.-L. Coll, L. V. Elst, R. Muller, S. Roux, P. Perriat, O. Tillement, *J. Am. Chem. Soc.* **2007**, *129*, 5076.

[117] W. C. Law, K. T. Yong, I. Roy, G. Xu, H. Ding, E. J. Bergey, H. Zeng, P. N. Prasad, *J. Phys. Chem. C* **2008**, *112*, 7972.

[118] H. Meng, M. Xue, T. Xia, Y. L. Zhao, F. Tamanoi, J. F. Stoddart, J. I. Zink, A. E. Nel, *J. Am. Chem. Soc.* **2010**, *132*, 12690.

[119] J. E. Lee, N. Lee, H. Kim, J. Kim, S. H. Choi, J. H. Kim, T. Kim, I. C. Song, S. P. Park, W. K. Moon, T. Hyeon, *J. Am. Chem. Soc.* **2010**, *132*, 552.

[120] I. J. Iwuchukwu, M. Vaughn, N. Myers, H. O'Neill, P. Frymier, B. D. Bruce, *Nat. Nanotechnol.* **2010**, *5*, 73.

[121] U. Biermann, U. Bornscheuer, M. A. R. Meier, J. O. Metzger, H. J. Schafer, *Angew. Chem. Int. Ed.* **2011**, *50*, 3854.

[122] S. Febvay, D. M. Marini, A. M. Belcher, D. E. Clapham, *Nano Lett.* **2010**, *10*, 2211.

[123] B. Städler, A. D. Price, A. N. Zelikin, *Adv. Funct. Mater.* **2011**, *21*, 14.
[124] B. M. Venkatesan, R. Bashir, *Nat. Nanotechnol.* **2011**, *6*, 615.
[125] D. Shi, N. M. Bedford, H. S. Cho, *Small* **2011**, *7*, 2549.
[126] G. Maltzahn, J. H. Park, K. Y. Lin, N. Singh, C. Schwöppe, R. Mesters,W. E. Berdel, E. Ruoslahti, M. J. Sailor, S. N. Bhatia, *Nat. Mater.* **2011**, *10*, 545.
[127] K. Li, B. Liu, *J. Mater. Chem.* **2012**, *22*, 1257.
[128] S. Shylesh, V. Schunemann, W. R. Thiel, *Angew. Chem. Int. Ed.* **2010**, *49*, 3428.
[129] X. Gao, Y. Cui, R. M. Levenson, L. W. K. Chung, S. Nie, *Nat. Biotechnol.* **2004**, *22*, 969.
[130] Z. Liu, K. Yang, S. T. Lee, *J. Mater. Chem.* **2011**, *21*, 586.
[131] J. D. Hartgerink, E. Beniash, S. I. Stupp, *Science* **2001**, *294*, 1684.
[132] H. Cui, M. J. Webber, S. I. Stupp, *Biopolymers* **2010**, *94*, 1.
[133] Z. Zhelev, H. Ohba, R. Bakalova, *J. Am. Chem. Soc.* **2006**, *128*, 6324.
[134] C. Wu, Y. Jin, T. Schneider, D. R. Burnham, P. B. Smith, D. T. Chiu, *Angew. Chem. Int. Ed.* **2010**, *49*, 9436.
[135] X. Gao, S. Nie, *Anal. Chem.* **2004**, *76*, 2406.
[136] X. Gao, S. Nie, *J. Phys. Chem. B* **2003**, *107*, 11575.
[137] E. Tasciotti, X. Liu, R. Bhavane, K. Plant, A. D. Leonard, B. K. Price, M. M. C. Cheng, P. Decuzzi, J. M. Tour, F. Robertson, M. Ferrari, *Nat. Nanotechnol.* **2008**, *3*, 151.
[138] J. S. Ananta, B. Godin, R. Sethi, L. Moriggi, X. Liu, R. E. Serda, R. Krishnamurthy, R. Muthupillai, R. D. Bolskar, L. helm, M. Ferrari, L. J. Wilson, P. Decuzzi, *Nat. Nanotechnol.* **2010**, *5*, 815.
[139] Y. Chen, H. Chen, S. Zhang, F. Chen, L. Zhang, J. Zhang, M. Zhu, H. Wu, L. Guo, J. Feng, J. Shi, *Adv. Funct. Mater.* **2011**, *21*, 270.
[140] J. Liu, S. Z. Qiao, Q. H. Hu, G. Q. Lu, *Small* **2011**, *7*, 425.
[141] X. Hu, X. Gao, *ACS Nano* **2010**, *4*, 6080.
[142] S. Y. Emelianov, P. C. Li, M. O'Donnell, *Phys. Today* **2009**, *62*, 34.
[143] X. Wang, Y. Pang, G. Ku, X. Xie, G. Stoica, L. V. Wang, *Nat. Biotechnol.* **2003**, *21*, 803.
[144] H. F. Zhang, K. Maslov, G. Stoica, L. H. V. Wang, *Nat. Biotechnol.* **2006**, *24*, 848.
[145] I. G. Calasso, W. Craig, G. J. Diebold, *Phys. Rev. Lett.* **2001**, *86*, 3550.
[146] B. T. Cox, P. C. Beard, *J. Acoust. Soc. Am.* **2005**, *117*, 3616.
[147] M. H. Xu, L. H. Wang, *Rev. Sci. Instrum.* **2006**, *77*, 22.
[148] A. A. Oraevsky, A. A. Karabutov, E. V. Savateeva, *Proc. SPIE* **2001**, *60*, 4434.
[149] S. Link, C. Burda, B. Nikoobakht, M. A. EI-Sayed, *J. Phys. Chem. B* **2000**, *104*, 6152.
[150] Z. B. Ge, Y. J. Kang, T. A. Taton, P. V. Braun, D. G. Cahill, *Nano Lett.* **2005**, *5*, 531.
[151] Y. S. Chen, W. Frey, S. Kim, K. Homan, P. Kruizinga, K. Sokolov, S. Emelianov, *Optics Express* **2010**, *18*, 8867.

[152] H. Ke, J. Wang, Z. Dai, Y. Jin, E. Qu, Z. Xing, C. Guo, X. Yue, J. Liu, *Angew. Chem. Int. Ed.* **2011**, *50*, 3017.

[153] H. Maeda, *Adv. Enzyme Regul.* **2001**, *41*, 189.

[154] S. D. Perrault, C. Walkey, T. Jennings, H. C. Fischer, W. C. Chan, *Nano Lett.* **2009**, *9*, 1909.

[155] B. Kim, G. Han, B. J. Toley, C. K. Kim, V. M. Rotello, N. S. Forbes, *Nat. Nanotechnol.* **2010**, *5*, 465.

[156] C. Gao, Q. Zhang, Z. Lu, Y. Yin, *J. Am. Chem. Soc.* **2011**, *133*, 19706.

[157] Y. Yin, A. P. Alivisatos, *Nature* **2005**, *437*, 664.

[158] V. F. Segers, R. T. Lee, *Nature* **2008**, *451*, 937.

[159] J. W. M. Bulte, *Am. J. Roentgen.* **2009**, *193*, 314.

[160] H. Wang, F. Cao, A. De, Y. Cao, C. Contag, S. S. Gambhir, J. C. Wu, X. Chen, *Stem Cells* **2009**, *27*, 1548.

[161] I. M. Barbash, P. Chouraqui, J. Baron, M. S. Feinberg, S. Etzion, A. Tessone, L. Miller, E. Guetta, D. Zipori, L. H. Kedes, R. A. Kloner, J. Leor, *Circulation* **2003**, *108*, 863.

[162] B. S. Shah, P. A. Clark, E. K. Moioli, M. A. Stroscio, J. J. Mao, *Nano Lett.* **2007**, *7*, 3071.

[163] S. Lin, X. Xie, M. R. Patel, Y. H. Yang, Z. Li, F. Cao, O. Gheysens, Y. Zhang, S. S. Gambhir, J. H. Rao, J. C. Wu, *BMC Biotechnol.* **2007**, *67*, 1472.

[164] T. H. Chung, J. K. Hsiao, S. C. Hsu, M. Yao, Y. C. Chen, S. W. Wang, M. Y. P. Kuo, C. S. Yang, D. M. Huang, *ACS Nano* **2011**, *12*, 9807.

[165] H. Kim, H. M. Dae, C. Park, E. O. Kim, D. Kim, I. H. Kim, Y. H. Kim, Y. Choi, *J. Mater. Chem.* **2011**, *21*, 7742.

[166] C. Wang, X. Ma, S. Ye, L. Cheng, K. Yang, L. Guo, C. Li, Y. Li, Z. Liu, *Adv. Funct. Mater.* **2012**, *22*, 2363.

[167] C. W. Lu, Y. Hung, J. K. Hsiao, M. Yao, T. H. Chung, Y. S. Lin, S. H. Wu, S. C. Hsu, H. M. Liu, C. Y. Mou, C. S. Yang, D. M. Huang, Y. C. Chen, *Nano Lett.* **2007**, *7*, 149.

[168] H. Yukawa, Y. Kagami, M. Watanabe, K. Oishi, Y. Miyamoto, Y. Okamoto, M. Tokeshi, N. Kaji, H. Noguchi, K. Ono, M. Sawada, Y. Bab, N. Hamajima, S. Hayashi, *Biomaterials* **2010**, *31*, 4094.

[169] A. Aicher, W. Brenner, M. Zuhayra, C. Badorff, S. Massoudi, B. Assmus, T. Eckey, E. Henze, A. M. Zeiher, S. Dimmeler, *Circulation* **2003**, *107*, 2134.

[170] K. S. Aboody, A. Brown, N. G. Rainov, K. A. Bower, S. Liu, W. Yang, J. E. Small, U. Herrlinger, V. Ourednik, P. M. Black, *Proc. Natl. Acad. Sci. U.S.A.* **2000**, *97*, 12846.

Curriculum Vitae

Po-Jung Chen

Advisor: Prof. San-Yuan Chen/Dean-Mo Liu

Department of Materials Science Engineering,

National Chiao Tung University

1001 Ta Hsueh Road, Hsinchu, Taiwan 300, ROC

E-mail: blacklight12345@gmail.com

I. **B.S.:** National Chung Cheng University (2004-2008), Chia-yi, Taiwan ROC

Major: Department of Chemistry and Biochemistry

II. **M. S.:** National Chiao Tung University (2008-2009), Hsinchu, Taiwan ROC

Major: Department of Materials Science and Engineering

III. **Ph. D.:** National Chiao Tung University (2009-2013), Hsinchu, Taiwan ROC

Major: Department of Materials Science and Engineering

Publications

SCI paper:

1. **Po-Jung Chen**, Shang-Hsiu Hu, Chi-Sheng Hsiao, You-Yin Chen, Dean-Mo Liu* and San-Yuan Chen* "Multifunctional magnetically removable nanogated lids of Fe_3O_4–capped mesoporous silica nanoparticles for intracellular controlled release and MR imaging", Journal of Materials Chemistry, 2011, 21, 2535.
2. **Po-Jung Chen**, Shang-Hsiu Hu, Wen-Ting Hung, San-Yuan Chen* and Dean-Mo Liu* "Geometrical confinement of quantum dots in porous nanobeads with ultraefficient fluorescence for cell-specific targeting and bioimaging", Journal of Materials Chemistry, 2012, 22, 9568.
3. Shang-Hsiu Hu, Bang-Jie Liao, Chin-Sheng Chiang, **Po-Jung Chen**, I-Wei Chen and San-Yuan Chen*Core-shell Nanocapsules Stabilized by Single-Component Polymer and Nanoparticles for Magneto-Chemotherapy-Hyperthermia with Multiple Drugs, Advanced Materials, 2012, 24, 3627.
4. **Po-Jung Chen**, Shang-Hsiu Hu, Chih-Tai Fan, Meng-Lin Li, You-Yin Chen San-Yuan Chen* and Dean-Mo Liu* "A novel multifunctional nano-platform with enhanced anti-cancer and photoacoustic imaging modalities using gold-nanorod-filled silica nanobeads", Chemical Communications, 2013, 49, 892.

Conference paper:

1. **Po-Jung Chen**, Shang-Hsiu Hu, Dean-Mo Liu* and San-Yuan Chen* "Fe_3O_4-capped Mesoporous Silica Nanoparticles for Magnetically Remote-controlled Drug Release and MR Imaging" NanoBio-Europe 2011 , Cork, Ireland.
2. **Po-Jung Chen**, Shang-Hsiu Hu, Wen-Ting Hung, You-Yin Chen, Dean-Mo Liu* and San-Yuan Chen* "Incorporation of Quantum-Dots with Mesoporous Silica Nanoparticles

for Intracellular Targeting and *In Vivo* Images" 2011 Materials Research Society (MRS) Fall Meeting, Boston, USA.

3. **Po-Jung Chen**, Shang-Hsiu Hu, Chih-Tai Fan, Meng-Lin Li, Dean-Mo Liu* and San-Yuan Chen* "Mesoporous Silica Nanoparticles Stuffed with Gold Nanorods as a Multifunctional Theranostic Platform for Cancer Treatment and Potoacoustic Imaging" Colloids and nanomedicine 2012, Amsterdam, Holland.